THE LUMINESCENT RESPONSE OF PHOSPHORS AND SCINTILLATORS TO IONS WITH ENERGIES IN THE 0 — 100 KeV RANGE

A Thesis Presented in Partial Fulfillment of the Requirements

for the

Degree of Master of Science

at

Lakehead University

Kim Hwa Tan

Lakehead University

1973

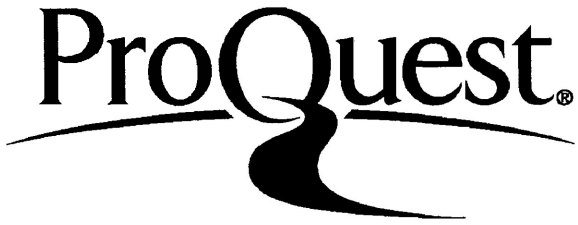

ProQuest LLC.
789 East Eisenhower Parkway
P.O. Box 1346
Ann Arbor, MI 48106 - 1346

ABSTRACT

A survey of the ionoluminescence of a large number of ion-phosphor combinations under uniform conditions has been made. Powdered phosphors and scintillation crystals with different activators, different methods of surface treatment and different particle size were studied in the energy range from 3 — 100 KeV. L, the ratio of integrated photomultiplier output to incident ion current, was found to be a sensitive function of ion energy. It increased with increasing ion energy and decreased with increasing ion mass. A nonlinear relationship between L and E, the ion energy, was observed for heavier ions, the nonlinearity increasing with ion mass. Comparisons of L values obtained in ZnS, YVO_4 and in Zn_2SiO_4:Mn phosphors of different particle size and with different activators were made. The results indicated that the light output may depend on the mechanism of luminescence, the crystal structure and the activators, as well as the surface conditions of the samples. By taking into consideration the non-radiative surface recombination of electron-hole pairs and assuming that the rate of generation of carrier pairs along the path of a particle is proportional to the specific energy loss in electron collision $(dE/dR)_e$, a formula was obtained to predict the nonlinear dependence of L at low energies.

ACKNOWLEDGEMENTS

The author wishes to thank his research supervisor, Dr. L. Hastings, for his guidance and many helpful discussions during the time that this study was in progress, and in the preparation of the manuscript. The author is also indebted to Professor B. J. Spenceley for reading the manuscript.

The financial support from Lakehead University, which made this study possible, is gratefully acknowledged.

LIST OF FIGURES

LIST OF TABLES

TABLE OF CONTENTS

I.

INTRODUCTION

When phosphors are subjected to low energy ion bombardment light is produced. This phenomenon, ionoluminescence, has been studied by many workers in different laboratories concentrating on one or two ion-phosphor combinations and attempting to fit theoretical models to the experimental results. As a rule, the results of one laboratory are not directly comparable with those of another because only a relative measure of the light produced is made and because different detection systems are used. This thesis is a report of work carried out in this laboratory to study as many ion-phosphor combinations as possible under conditions that would reveal the relative efficiences of all of them. During the experiments careful measurements were made and experimental precautions were taken to ensure that all the experimental data obtained were intercomparable. The experiments ranged over many of the commonly reported phosphors and scintillators with different activators, different particle sizes and different surface treatments. Each phosphor type was subjected to bombardment by a variety of heavy and light ions with energies ranging from 3 to 100 KeV.

Additionally it was expected that the data obtained would yield insight into the details of the energy loss and light production mechanisms in the region where nuclear stopping competes with electronic stopping. Particularly it was hoped that a test of the validity of the equation

$$L(E_0) = C \int_0^{E_0} \frac{S_e}{S_e + S_n} dE \qquad (1)$$

could be made. In this equation, $L(E_0)$ is the total amount of light produced along the entire trajectory of an ion that comes to rest inside the stopping medium, S_e and S_n are the electronic and nuclear stopping cross sections, respectively, E_0 is the initial energy of the ion and C is a constant.

II.

REVIEW OF PAST WORK

The luminescent response of powdered inorganic phosphors, such as Zn_2SiO_4, ZnO and ZnS, to ions of different mass has been studied fairly extensively. The luminescent response of such materials is a result of electronic excitation in the host lattice. Many experiments[1-7] have been reported that deal with luminescence processes, energy losses and radiation damage in these phosphors. The luminescence experiments have dealt mainly with the dependence of the intensity of the light output on the incident energy of the fast ions. When a thick layer of powdered phosphor is bombarded with fast ions, light is assumed to be produced along the entire trajectory and the intensity of the light output increases with increasing ion energy and decreases with increasing ion mass. Theoretical interpretations of the luminescent response of these phosphors have been made by considering the energy loss of ions in electronic collision processes.[1-7]

Eve and Duckworth[1] have studied the luminescent response of Zn_2SiO_4:Mn and ZnS:Ag powdered phosphors under low energy ion bombardment. They determined the efficiency of ionoluminescence using the ions $^4He^+$, $^7Li^+$, $^{23}Na^+$, $^{39}K^+$, $^{40}Ar^+$ and $^{85}Rb^+$ in the energy range 5 — 30 KeV. Within this energy range, the luminescence efficiency was found to be a sensitive function of the ion energy, increasing with increasing ion energy and decreasing rapidly as the mass of the incident ions increased. In analysing their results, they have assumed that the luminescence is the result of

electronic excitation in the host lattice and that the intensity is always proportional to the amount of such excitation. According to the theoretical work of Bohr[8] and Nielsen,[9] when the velocity of the incident particles is less than v_0, the velocity of the electron in the first Bohr orbit of the hydrogen atom, the incident particles can be regarded as neutral atoms throughout the penetration of the solid, since the electron capture cross section is so large. The stopping power of the target for a heavy particle is considered to be approximately constant. The probability that an electronic transition will be induced in a stationary atom by the close passage of a slow atomic particle is given by the formula of Seitz and Koshler.[10] With these assumptions, Eve and Duckworth were able to get a good fit for their ZnS:Ag data, but failed with the Zn_2SiO_4:Mn results.

Further theoretical work by Lindhard and Scharff[11] and by Lindhard *et al.*[12] showed that the stopping power of the medium is not a constant for particles in this velocity range, but increases with increasing energy. This was subsequently confirmed by the experiments of van Wijngaarden and Duckworth[2] and by Ormrod and Duckworth.[55] It is well known that heavy ion bombardment of a phosphor causes a considerable degree of damage due to the formation of defects in the crystal structure. The energy loss of heavy ions, the radiation damage and deterioration depth in the phosphors ZnS:Ag and ZnO:Zn have been studied by Hastings, Ryall and van Wijngaarden,[4] and by Hastings and van Wijngaarden.[5] The observed energy losses of ^{4}He, ^{14}N, ^{40}Ar and ^{84}Kr ions in ZnS:Ag and ZnO:Zn when compared to the energy loss for hydrogen were all much smaller than the Lindhard and Scharff theory

predicted.

Ionoluminescence was not critically compared with Lindhard's theory until 1965 when van Wijngaarden, Bradley and Finney[6] studied powdered MgO and Zn_2SiO_4:Mn under bombardment with $^1H^+$, $^4He^+$, $^{14}N^+$, $^{40}Ar^+$ and $^{84}Kr^+$ ions. They assumed that electronic excitation in the stopping medium is a result of the direct interaction between the projectile and the electrons in the target material and that secondary interactions between the electrons and lattice atoms recoiling from nuclear collisions are negligible. As a result, the energy loss to electrons in an element of path length dR is $dE_e = NS_e dR$ where N is the number density of atoms in the stopping medium and S_e is the electronic stopping cross section. The total energy transferred to the electrons could then be written as

$$E_e = \int_0^{E_0} \frac{S_e}{S_e + S_n} dE$$

by making use of the relation $-dE/dR = NS = N(S_e + S_n)$ where S is the total stopping cross section and S_n is the nuclear stopping cross section. The total light output of the incident particle in coming to rest in the stopping medium is represented by Eqn. (1). This integral can be evaluated by numerical methods. For light incident particles such as $^1H^+$ for which $S_e >> S_n$, the light output is simply CE_0. Their experimental results for MgO agree well with the theoretical predictions, but for Zn_2SiO_4:Mn the discrepancy is quite large. The experimental curves for the heavier ions are slightly steeper than the corresponding theoretical curves. In addition, there is a great difference in light output between light and heavy ions. To account for the discrepancies, these workers suggested that C must be a velocity dependent function which should appear under the integral sign.

Careful experiments were also done on the combined effects of ionoluminescence and thermoluminescence of Zn_2SiO_4:Mn in an effort to show that the luminescent response to ion bombardment is independent of the population of the electron traps below the conduction band. The results strongly suggest that ionoluminescence is caused by excitation of the electrons in the host lattice.

The most recent experiments designed to investigate the light output on initial ion energy were done by Lao, Hastings, Finney and van Wijngaarden[7] using ZnO:Zn as the phosphor. They proposed that the energy loss, ΔE_e, of a projectile to electrons in a thin layer is related to the total energy loss, ΔE, in the same layer by $\Delta E_e = [(S_e / (S_e + S_n)]\Delta E$. The element of light output from this layer must therefore be $\Delta L = C[S_e / (S_e + S_n)]\Delta E$. It can be intuitively understood that this formula could take into account the radiation damage along the path of the ions which may be the main reason for the discrepancy between experiment and theory in the case of Zn_2SiO_4:Mn. For a thick layer of phosphor in which the particle comes to rest, the total light output is

$$L(E_0) = \int_0^{E_0} \frac{\Delta L}{\Delta E}\, dE$$

where the quantity, $\Delta L/\Delta E$, is called the luminescence efficiency. Numerical evaluation of this integral gives values which are in close agreement with the experimental results. The experiments also showed that the luminescence efficiency for a constant velocity decreased with increasing ion mass. This casts some light on the energy transfer processes; a light atomic projectile loses its energy mainly to electrons, whereas a heavy ion loses a greater share of its energy in nuclear en-

counters. Finally, the experiments showed that the total light output at constant projectile velocity had an oscillatory behavior with respect to Z_1, the incident ion atomic number, indicating that the mechanism for the luminescent response depends on the detailed behavior of the inelastic projectile-electron collision.

In 1970 Parilis[13] took an approach similar to that of van Wijngaarden *et al.*[6] to calculate the light output but used the calculations of Firsov[60] for the stopping powers. When the predictions of the theory were compared with the experimental results of Doll[14] and van Wijngaarden *et al.*[6] it was found that the theory predicted values 10 per cent lower for Ar^+ incident on MgO and 10 per cent higher for Ne^+ incident on ZnS. He concluded that the dependence of ionoluminescence on the velocity and type of ion is apparently determined by the excitation mechanism and is related to the energy release mechanism to a lesser extent. Thus the crystalline structure of phosphors must have its effect on the yield of luminescence.

The effect of surface recombination on ionoluminescence did not receive much attention until recent studies by Petrov and Makarov[15] and by Petrov.[16] They pointed out that the luminescent response of a given phosphor depends both on radiative recombination through the activator centers in the bulk of a crystal and on the surface recombination which is usually non-radiative. The relative importance of surface recombination should be dependent on the ratio of the depth at which electron-hole pairs are created, R, and the carrier diffusion length, L. They proposed that, under ion or electron bombardment, the intensity of luminescence may be written as

$$I_i = \frac{KE_i}{\varepsilon_i} f(R_i) \quad or \quad I_e = \frac{KE_e}{\varepsilon_e} f(R_e)$$

respectively. Here R_e and R_i are the projectile ranges and ε_e and ε_i are the mean energies spent by primary particles for creating one electron-hole pair, K is a constant and f(R) is a function which takes into account the surface effects. The value of f(R) increases when R increases, and $f(R) \to 1$ when $R/L >> 1$. They assumed that the generation rate was constant along the path of the projectile. Their experimental results showed that the values of I_i and I_e at a given energy of ions and electrons differed very much for samples with different impurity content and depended strongly on the method of surface treatment.

By comparing the values of I_i and I_e at which $f(R_e) = f(R_i)$, they made reasonable estimates of the values ε_i assuming the value ε_e. It was found that the values of ε_i depend on the projectile's initial energy, E_i, increasing with decreasing E_i. The total amount of energy given to electrons by $^7Li^+$ in SiC using the estimated value of $\varepsilon_i(Li)$ was found to be in good agreement with the value of

$$\int_0^{E_0} \frac{S_e}{S_e + S_n} dE$$

calculated according to Lindhard's theory.

Bulk materials which convert the kinetic energy of fast particles into light have been used extensively as nuclear particle detectors. These materials may be broadly divided into three groups: inorganic crystals (NaI(Tl), CsI(Tl), organic crystals (anthracene, stilbene) and plastics. The scintillation response of such materials to projectiles with energies

above 1 Mev has for obvious reasons been studied extensively.[17-28] The response of such materials in the KeV region has not received nearly as much attention since their resolution as particle detectors in this region is relatively poor, especially in comparison to surface barrier detectors. Studies of the response of these crystals to low energy and heavy particles are, however, of interest since they may yield insight into the details of the energy loss and light production mechanisms in the region where nuclear energy loss is significant.

A detailed account of the scintillation response of NaI(Tl) and CsI(Tl) to low energy heavy ions was given by Cano and Lockwood[28] in 1967. In this work, it was found that the light output of CsI(Tl) increased linearly with energy for all ions tested. The response of NaI(Tl) had in general two distinct linear regions for a particular projectile. The point of the inflection and the sense of the inflection depended upon the incident projectile. The behavior of the light output was explained in terms of a model based on the theories of Bohr[8] and Lindhard *et al.*[12] in which the electronic excitation was calculated using Lindhard's theory and the elastic energy loss was calculated along the lines of Bohr. They obtained a fair agreement between theory and experiment. The nonlinear behavior of the NaI(Tl) results was not predicted by this model nor was a plot of the spread in pulse height *versus* electronic energy loss as the incident projectile was changed. The variation of the efficiency might well be understood in terms of the Z_1 dependence of L observed by Lao *et al.*[7] in ZnO:Zn.

The scintillation response of organic scintillators has been described extensively by Birks,[23] in general they differ significantly

from inorganic compounds. The essential features of the scintillation process in an organic scintillator are determined by the molecular structure. Organic materials, unlike the inorganic compounds, form molecular crystals in which the molecules are loosely bound together by van der Waals forces and retain their individual identity, electronic structure and luminescence.

The primary scintillation process is common to all types of organic scintillator and corresponds to the transfer of excitation energy from ionizing particles to the solvent. Subsequent processes depend on the type of scintillator and have been classified by Birks into three systems: (1) Unitary (pure crystals, e.g. anthracene, stilbene). (2) Binary (binary liquid solution, binary plastic solution, binary crystal solution). The excitation energy obtained by the solvent molecules from the incident particle is transferred to the solute molecules prior to emission, the emission spectrum is mainly that characteristic of the solute. (3) Ternary (ternary liquid solution, ternary plastic solution). The emission spectrum is mainly that of the secondary solute, the excitation energy of the solvent being transferred *via* the primary solute to the secondary solute.

The scintillation response, L, of anthracene and stilbene crystals and plastic solutions to different ionizing particles of various energies has been studied at high energies by many workers.[30-35] In general, L varies nonlinearly with E and depends on the nature of the ionizing particles. The form of response curves is similar in all organic materials, though there are slight differences in shape. To describe this nonlinear behavior, which is attributed to quenching of the primary excitation by a high density of ionized and excited molecules, Birks and Black[36] proposed

a semi-empirical relation which gave satisfactory agreement with experiment,[29] except that the response to low energy incident particles was less than expected. The discrepancy between theory and experiment, as described by Birks, is due to the surface quenching effect. To take into account the surface effect, Birks modified his original equation. The validity of the modified equation was confirmed by Fowler and Roos[33] who observed the scintillation response of anthracene and stilbene crystals to 10-40 KeV x-rays and 170-570 KeV protons.

Birks concluded that there are three possible processes that can cause a surface decrease in fluoresence efficiency: (1) escape of excitation energy, which reaches the surface either as excitons or fluorescence photons, (2) back-scattering of incident radiation, (3) quenching by impurity molecules in the surface layer. Results of experiments by Brannen and Olde[38] on the response of the plastic scintillator NE101 to electrons showed that the major cause of the surface effect is the surface escape of excitation energy.

III.

THEORY

Introduction

Luminescence is due to the excitation of electrons into the conduction band from the valence band. A fraction of the excitation energy is transferred to the luminescence centers which subsequently emit.

To understand the response of phosphors to fast ions, the following questions must be asked.

(1) How is energy transmitted to the crystal?

(2) How is energy converted to light in bulk material?

(3) Since the penetration depth of fast ions is not large, what is the effect of the surface?

It is believed that ionoluminescence is due to the electronic excitation mechanism; that is, the energy spent in generating electron-hole pairs is transmitted from the ions to the crystal by inelastic collisions. Elastic collisions will cause atomic displacement and this energy is probably dissipated in the form of heat.

Luminescence resulting from ion bombardment constitutes a very complicated phenomenon which depends on the slightest admixture of impurity atoms, their position in the lattice and the structure of the lattice itself. The most common form of luminescence involving transport of charge is that in which electrons and holes recombine at a crystal imperfection. This imperfection may be a quenching center, in which the energy is quenched without producing any light, or a luminescent center, which subsequently emits a photon. The electron and hole may

recombine and form an exciton, which diffuses through the lattice (non-radiative migration) until it is captured by either a luminescent center or a quenching center or even a low-lying trap. In most inorganic phosphors, the host lattice is transparent to the emission, so that the light produced can be detected.

Since the depth at which electron-hole pairs are created is not large under fast ion bombardment, they may diffuse through the crystal and recombine non-radiatively at the surface. Thus the surface may act as an absorber or a quencher, which reduces the light output considerably, especially for heavier ions.

The luminescence processes and energy transfer mechanisms in inorganic materials are essentially different from those in phosphors. They are determined mainly by the molecular structure, as well as the interaction between molecules. The energy may be transferred from the solvent to the solute or from the solvent *via* the primary solute to the secondary solute depending on the type of scintillator. Due to the complexity of the excitation processes, no model for the ionoluminescence of such substances will be developed here.

Energy Loss Mechanisms

Charged particles lose energy to both the atomic and electronic systems in a target. At high energies where the particle's velocity is greater than the orbital velocity of the lattice electrons, inelastic losses to the electronic system dominate. As the particle slows down, nuclear collisions begin to compete with the electronic collisions and eventually predominate. Let us consider electronic stopping first.

A qualitative classification of slowing down for all kinds of charged particles is reproduced in Fig. 1.[39]

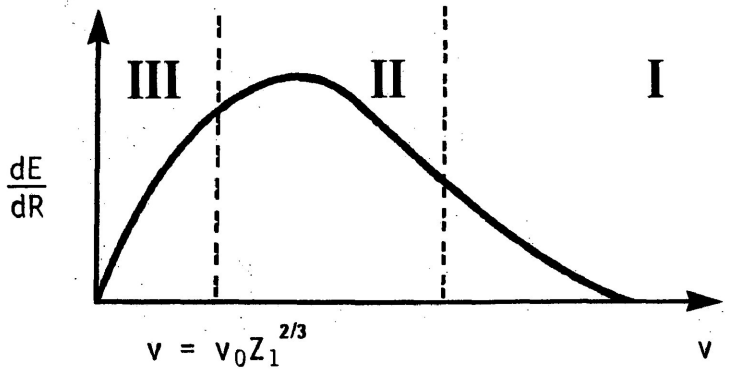

Fig. 1. Classification of stopping for arbitrary ion.

Here the specific energy loss, dE/dR, is shown as a function of particle velocity. The figure is divided into three velocity regions. In region I, where $v >> v_0$ ($v_0 = e^2/\hbar$ is the orbital velocity of the hydrogen electron), dE/dR decreases with increasing particle velocity, the stopping is completely electronic and the well-known Bethe-Bloch formula applies. Lindhard and Winther[40] proposed an equipartition rule, stating that the stopping is contributed to equally by close collision and plasma resonance excitation of the electron gas. They obtained approximate results for stopping at high and low velocities. At high velocities, the stopping is equivalent to the Bethe-Bloch expression, and at low velocities the stopping is closely proportional to the particle velocity.

Region II, which corresponds to intermediate velocities, includes the maximum stopping. For heavy particles, the accuracy of theoretical estimates is poor. For the transition from region I to region II for low Z particles, a shell correction to the Bethe-Bloch treatment has

been introduced by Walske[41] and later by Bonderup.[42]

In region III, the so-called low velocity region where particles have velocities $v < v_0 Z_1^{2/3}$, inner shell electrons have velocities very much greater than the particle velocity and therefore do not contribute to the energy loss. At very low particle energies, the lowest part of region III, nuclear stopping must also be considered and can compete with electronic stopping. For the present work region III, where ions lose energy both to the recoiling atoms and the electrons in the stopping medium, is of the greatest importance. The total energy loss is the sum of the electronic and nuclear components, $dE = dE_e + dE_n$. The specific energy loss, the so-called stopping power of a medium, is given by

$$-\frac{dE}{dR} = -\left[\left(\frac{dE}{dR}\right)_n + \left(\frac{dE}{dR}\right)_e\right]$$

where the subscripts, n and e, refer to the nuclear and electronic components, respectively.

S_e, S_n are given by the equations

$$\left(-\frac{dE}{dR}\right)_n = NS_n$$

$$\left(-\frac{dE}{dR}\right)_e = NS_e$$

$$\text{and } \left(-\frac{dE}{dR}\right) = NS = N(S_e + S_n) \; . \qquad (2)$$

Here N is the number of stopping atoms per unit volume. The three stopping cross sections are related by

$$S = S_e + S_n \; .$$

S_e and S_n are of the same order of magnitude when $v = 0.1\ v_0 Z_1^{2/3}$.[12]

Lindhard and Scharff[11] introduced a model based on a particle moving through an electron gas and suggested that the electronic stopping power is proportional to the particle velocity, v, when $v < v_0 Z_1^{2/3}$ which corresponds to the velocity of a proton with an energy less than 25 KeV. To a first approximation, they obtained

$$S_e = \xi_e \, .0793 \, 4\pi e \left(\frac{.8853\ a_0}{Z_1^{2/3} + Z_2^{2/3}} \right)^{3/2} \frac{Z_1 Z_2}{A_1^{1/2}} E^{1/2}$$

$$= KE^{1/2}$$

where ξ_e is a constant of the order of 1 or 2 and is approximately equal to $Z_1^{1/6}$.

By introducing the dimensionless energy ε and length ρ they obtained

$$S_e(\varepsilon) = \left(\frac{d\varepsilon}{d\rho} \right)_e = k\varepsilon^{1/2}$$

where the constant, k, is given by

$$k = \xi_e \frac{0.0793 Z_1^{1/2} Z_2^{1/2} (A_1 + A_2)^{3/2}}{(Z_1^{2/3} + Z_2^{2/3})^{3/4} A_1^{3/2} A_2^{1/2}}$$

ρ is given by

$$\rho = RNM_2 \frac{4\pi a^2 M_1}{(M_1+M_2)^2}$$

and ε is given by

$$\varepsilon = \frac{EaM_2}{Z_1 Z_2 e^2 (M_1+M_2)} .$$

The last two are dimensionless measures of range and energy, respectively. R is the path length travelled by the ion, N is the number of atoms per unit volume and E is the ion energy in the laboratory system, M_1 and Z_1

represent the mass and atomic number of the projectile, and M_2 and Z_2 represent the corresponding quantities for the target atom. A_1 and A_2 similarly represent their mass numbers. The quantity a has the value $0.8853\ a_0$.

The equation for S_e no longer holds when $v \geq v_0 Z_1^{2/3}$ and gradually assumes an $E^{-1}\ln E$ dependence. Recent work has shown S_e to have an oscillatory dependence on Z_1,[43-47] which is not predicted by Lindhard's theory.

Bohr[8] laid the foundation for a theoretical investigation of the stopping process in terms of elastic nuclear collisions and this later was extended by Nielsen[9] and by Lindhard and Scharff.[11] The reduced nuclear stopping cross section $(d\varepsilon/d\rho)$ can be computed using a Thomas-Fermi estimate of the interaction potential (Appendix I). The result of Lindhard's calculation is reproduced in Fig. 2, together with the constant nuclear stopping cross section derived from the power law potential. The full curve is $(d\varepsilon/d\rho)_n$ computed from the Thomas-Fermi model, the dashed curve is from the power law potential.

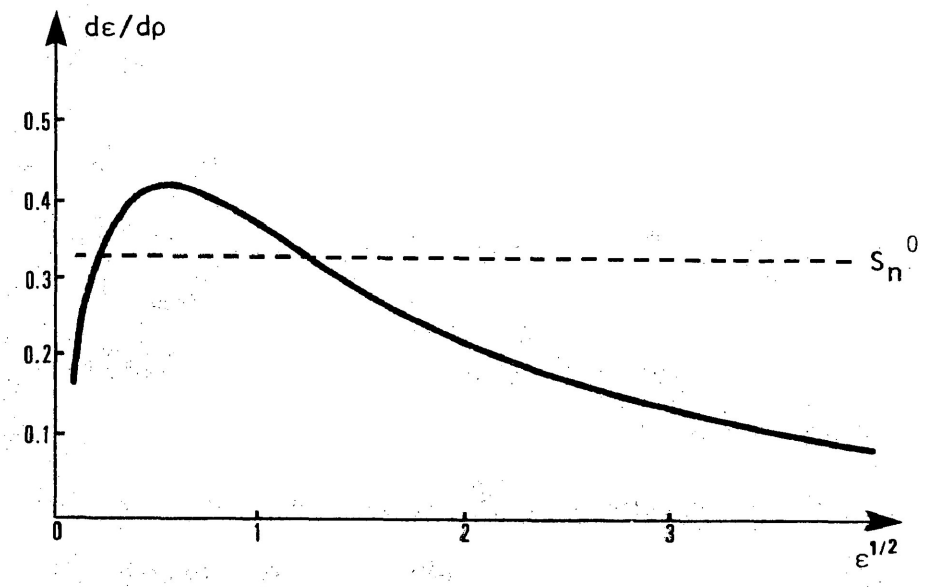

Fig. 2. Theoretical nuclear stopping cross section.

It has been shown that ionoluminescence is caused by the excitation of the electrons in the host lattice.[6] Ionoluminescence, like other forms of luminescence, occurs in two stages: the excitation of the electrons and the release of the stored energy, that is, an electron is excited from the valence band to the conduction band, a hole is left behind in the valence band, a photon is emitted when the electron-hole pair recombine *via* the luminescence centers. The mechanism for the release of the stored energy is roughly identical for various types of crystal luminescence centers.

The nuclear collisions between the projectile and the target atoms cause the target atoms to recoil. However, since the majority of such collisions involve only small angular deflection of the projectile (see Appendix I), the electronic excitation produced by the secondaries will be ignored. The energy loss in nuclear collisions is probably dissipated in the form of heat, whereas the direct interaction between the projectile and the electrons in electronic collisions will cause the electrons to make transitions which result in the production of light. Since inelastic collisions are responsible for electronic excitation, the integrated light output (L) in ionoluminescence should be proportional to the energy transferred to the electrons. For an atomic projectile, travelling along an element dR of its trajectory, the energy loss to electrons is given by $dE_e = NS_e dR$. By making use of Eqn. (2), van Wijngaarden[6] obtained

$$dE_e = [S_e / (S_e + S_n)]dE \ .$$

Thus the total energy lost to electrons by a projectile which comes to rest inside the stopping medium is

$$E_e = \int_0^{E_0} \frac{S_e}{S_e + S_n} dE \qquad (3)$$

where E_0 is the initial energy of the projectile.

The curves of E_e *versus* E_0 for ZnO shown in Fig. 3 were obtained by numerical integration of Eqn. (3). Fig. 3 also shows the calculated points for the phosphors ZnS, Zn_2SiO_4 and CsI, but for clarity no curves have been drawn through them.

Since we have assumed that the total light intensity, L, produced along the entire trajectory of a projectile that comes to rest inside the stopping medium, is proportional to the energy lost to electrons, E_e, we write $L = CE_e$ or

$$L(E_0) = C \int_0^{E_0} \frac{S_e}{S_n + S_e} dE$$

where C is a constant.

Using the two dimensionless variables, ε and ρ, L can be written in the following terms

$$L(E_0) = C \frac{Z_1 Z_2 e^2 (M_1 + M_2)}{aM_2} \int_0^{\varepsilon_0} \frac{(d\varepsilon/d\rho)_e}{(d\varepsilon/d\rho)_e + (d\varepsilon/d\rho)_n} d\varepsilon$$

where $\varepsilon_0 = [aM_2 / Z_1 Z_2 e^2 (M_1 + M_2)] E_0$. Numerical integration of this equation was performed by evaluating $(d\varepsilon/d\rho)_e$ by means of the equation $(d\varepsilon/d\rho)_e = k\varepsilon^{1/2}$ and using Lindhard's curve for $(d\varepsilon/d\rho)_n$ shown in Fig. 2.

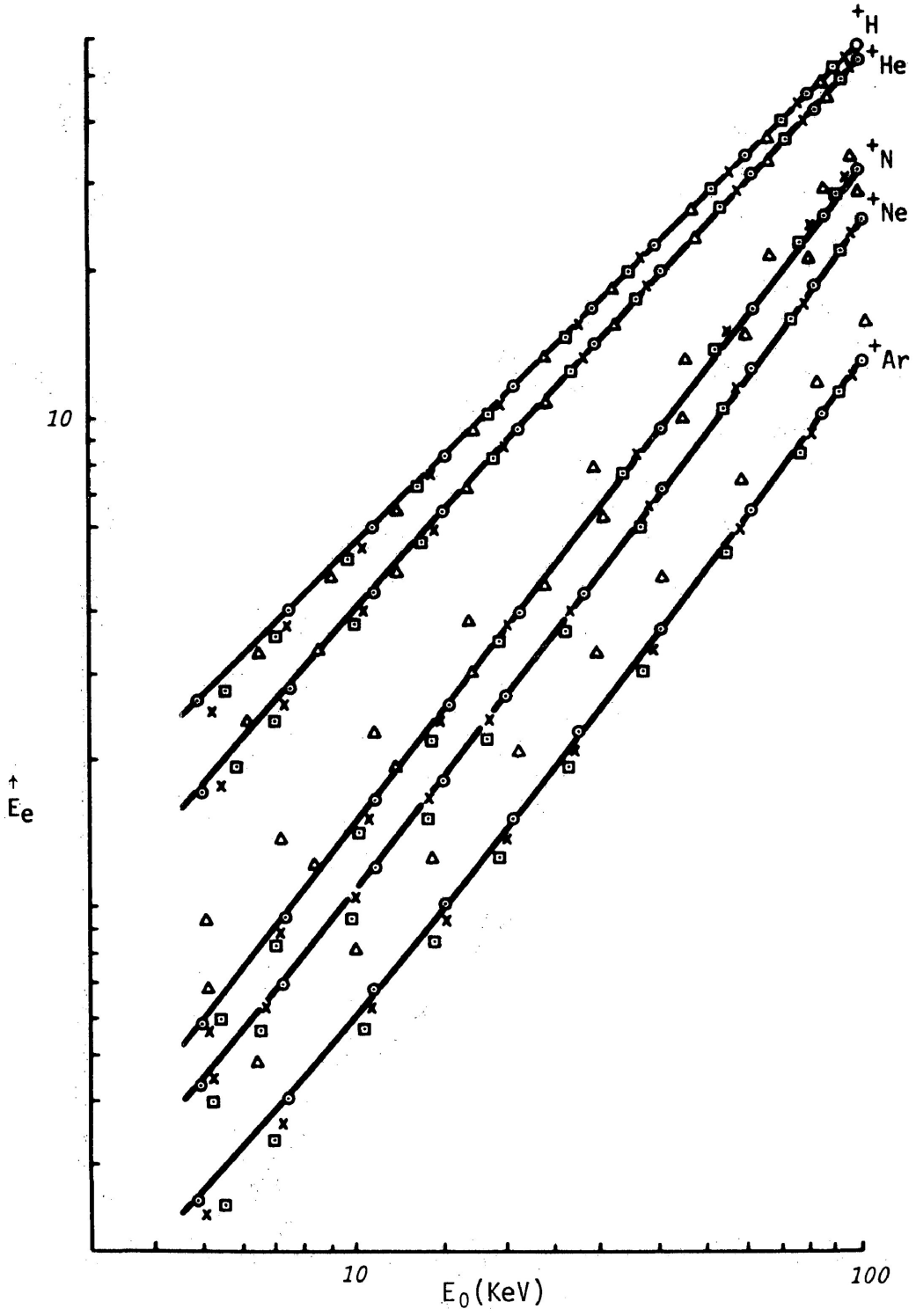

Fig. 3. Plot of the total energy lost to the electrons, E_e *versus* E_0 for ZnO(o), ZnS(×), Zn SiO (□) and CsI(Δ) samples.

Recombination Processes

Generally speaking when a photoconductive material is stimulated by energetic particles or by other means, if the excitation energy is sufficient to break the covalent electron pair lattice bonds, electrons will be liberated and leave holes behind at the excitation sites. In the presence of a source of excitation, electron-hole pairs are being continually generated and are continually recombining. The generation rate, g, is the number of electron-hole pairs generated per unit volume per unit time and the recombination rate, r, is related to the carrier lifetime, τ (or recombination lifetime) and the carrier concentration, n, by the relation $r = n/\tau$. The carrier generation rate, g, at any point in the volume of the material is proportional to the particle beam intensity. Obviously, g is not equal to n/τ except in the state of thermal equilibrium or without the presence of any excitation source. The thermal generation rate which is denoted g_0 is the number of electron-hole pairs generated per unit time per unit volume from thermal breakage of covalent bonds and is equal to the thermal recombination rate, n_0/τ_0; i.e., $g_0 = n_0/\tau_0$. Since the generation (or recombination) of an electron is inevitably accompanied by hole generation (or recombination), we may write $g_n = g_p$ and $n/\tau_n = p/\tau_p$, the subscripts n and p refer to electrons and holes, respectively, and in the thermal equilibrium state, $g_{0n} = n_0/\tau_{n0} = n_p/\tau_{p0} = g_{0p}$, the rate of carrier generation is equal to the rate of carrier recombination.

The motion of carriers in the solid may be determined by means of the continuity equation

$$d(\Delta n)/dt = D^*\nabla^2(\Delta n) + \mu^* E\cdot\nabla(\Delta n) + g - r \qquad (4)$$

which is developed by considering the flux of holes, J_p, and flux of electrons, J_n, through a volume element of material (see Appendix II). In this equation, D^* and μ^* are the ambipolar diffusion and mobility, respectively, and are given by

$$D^* = \frac{n + p}{n/D_p + p/D_n} ,$$

$$\mu^* = \frac{p - n}{n/\mu_p + p/\mu_n} .$$

For n type materials, when $n >> p$, $D^* = D_p$, and $\mu^* = -\mu_p$. The equation then has the form

$$d(\Delta p)/dt = D_p\nabla^2(\Delta p) - \mu_p \underset{\sim}{E}\cdot\nabla(\Delta p) + g - r .$$

In strong p type materials, where $p >> n$, $D^* = D_n$, $\mu^* = \mu_n$ and the equation has the form

$$d(\Delta n)/dt = D_n\nabla^2(\Delta n) + \mu_n \underset{\sim}{E}\cdot\nabla(\Delta n) + g - r .$$

And, for intrinsic materials, where $n = p$, $D^* = 2D_pD_n/D_p+D_n$, $\mu^* = 0$, and the equation has the form

$$d(\Delta n)/dt = D^*\nabla^2(\Delta n) + g - r .$$

Finally, it should be admitted that we have no intention of applying Eqn. (4) to any but one-dimensional problems and without the presence of an electric field, so that the continuity equation reduces to

$$d(\Delta n)/dt = d(\Delta p)/dt = D^*d^2(\Delta n)/dX^2 + g - r .$$

More simply, it can be written

$$dn/dt = D(d^2n/dX^2) + g - r \qquad (5)$$

where the asterisk has been dropped and n has replaced Δn since n_0 is negligible for large band-gap intrinsic materials.

The various processes for recombination of electrons and holes fall into two classes, depending on whether the electrons and holes recombine directly by band-to-band transitions, or indirectly *via* intermediate localized energy levels in the forbidden gap, such as shown in Fig. 4.

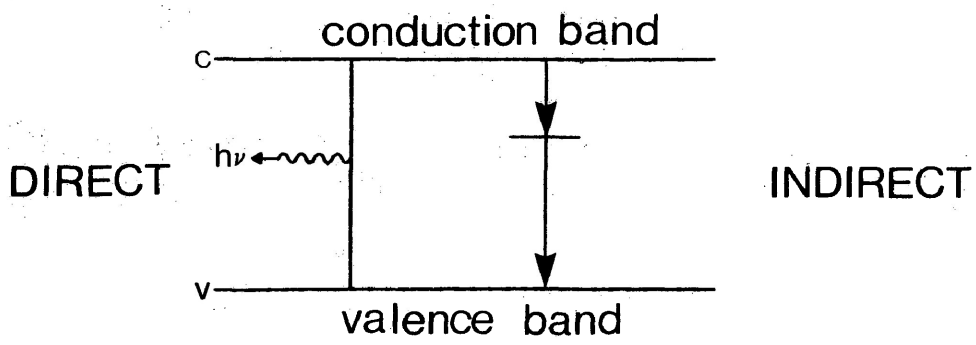

Fig. 4. Competing recombination processes.

In direct recombination, the electrons must release an amount of energy approximately equal to the full gap energy, this energy is carried away by the photon of frequency, ν, given by $h\nu = E_V - E_C$. In indirect recombination, some energy which would have been carried away by the photon in a direct transition is now carried away by phonons, the frequency of the radiation associated with such transitions is given by $h\nu = E_V - E_C + E_p$ where E_p is the energy of the phonon involved.

These two recombination processes are always competing. For direct recombination, light emission is generally the important mechanism,

while for indirect transitions, phonon emission predominates. Whether an indirect recombination process will or will not produce light depends on the nature of the recombination center.

The statistical treatment of trapping of electrons and holes by a localized energy level lying deep within the energy gap was first investigated by Shockley and Read.[51] There are four basic processes involved in an electron-hole recombination through trapping centers, as illustrated in Fig. 5.

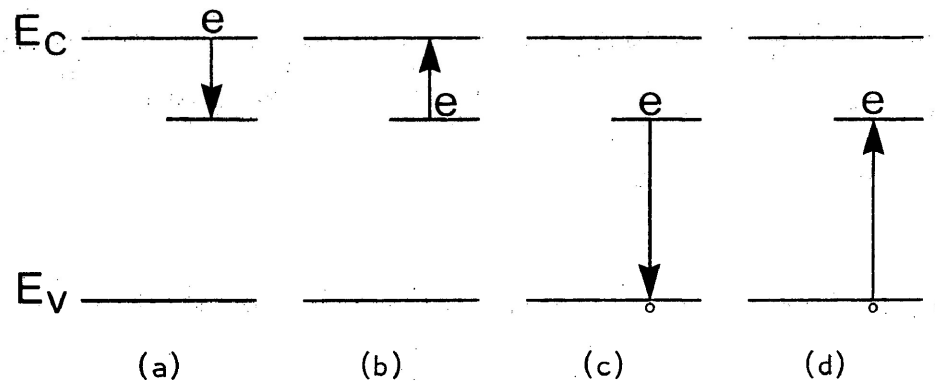

Fig. 5. Four fundamental processes involved in recombination through traps.

(a) The capture of an electron from the conduction band by an initially neutral empty trap.
The energy loss of the electron is then converted into heat or light or both depending upon the nature of the trapping process.

(b) The emission of an electron from the trap to the conduction band.

(c) The capture of a hole from the valence band by a trap containing an electron or the emission of a trapped electron to the valence band.

(d) The capture of an electron from the valence band or the emission of a hole from the trap to the valence band.

These trapping processes are characterized by an average capture cross section for recombination. The probability that a free carrier will make a transition to a localized level or across the gap depends on the number of electrons in the conduction band and the capture cross section of the traps.

Comparatively, a more practical model of electron hole recombination and trapping processes was studied by Birks.[29] A schematic diagram of the energy level system for an impurity activated crystal phosphor is shown in Fig. 6.

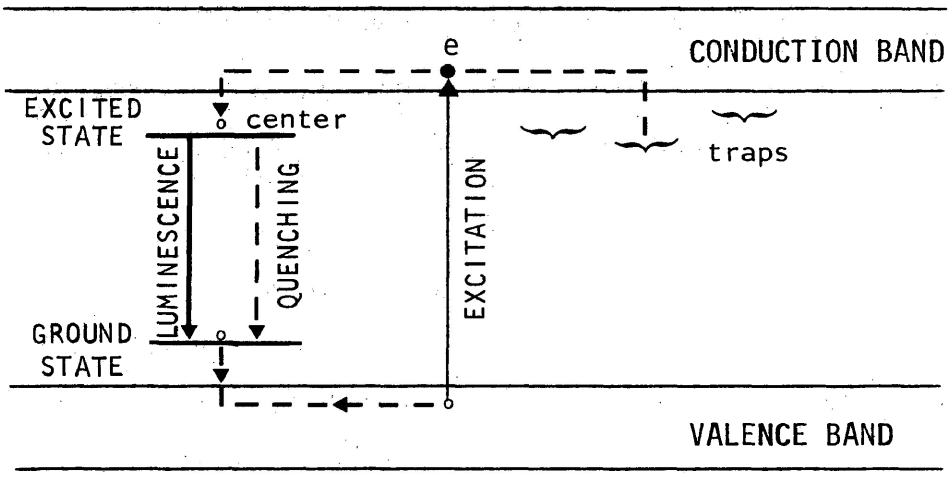

Fig. 6. Energy bands in an impurity crystal phosphor showing excitation, luminescence, quenching and trapping centers.

The luminescence centers and traps arise from crystal imperfection. Electrons excited from the valence band to the conduction band, moving in the vicinity of luminescence centers or traps, may enter these centers or traps if they are unoccupied. The electron captured by the trap may return to the conduction band by acquiring sufficient thermal energy or fall to the valence band by a radiationless transition. When an electron-hole

pair recombines at the luminescence center, a photon is emitted subsequently. If the recombination occurs at a quenching center, the excitation energy will dissipate in the form of heat. Luminescence requires the recombination of an electron and a hole at the activator center.

The indirect recombination of electrons and holes, accompanied by the phonon-emission process, can well be explained by the concept of the configuration diagram. The configuration diagram, as shown in Fig. 7, presents the energy, E, of the ground state and of the first excited state of an atom as a function of its configuration coordinate, X, this atom being either an impurity atom or a host lattice atom.

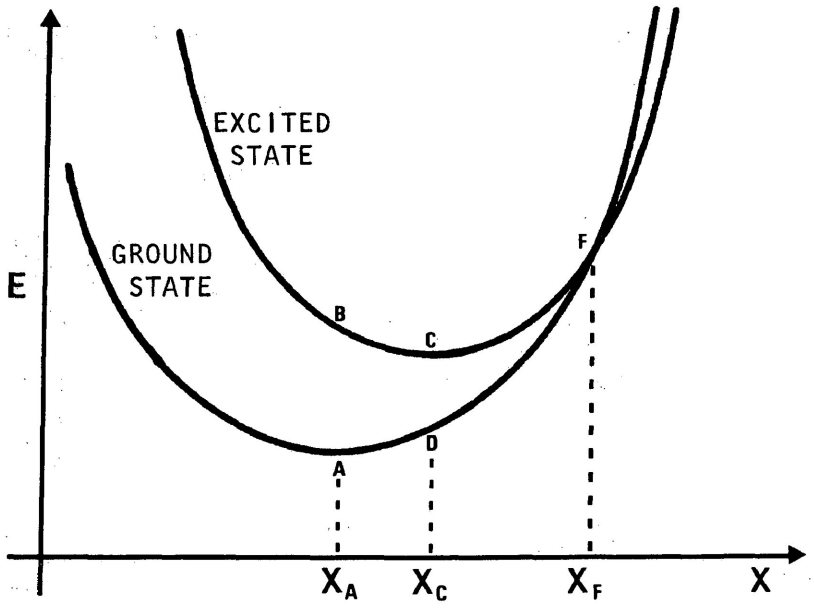

Fig. 7. Configuration diagram.

A and C are the equilibrium potentials of an electron in the ground state and the first excited state, respectively, and correspond to slightly different positions of the atom. Hence, when the electron

is excited from the ground state at A to the excited state at B, the whole system partly relaxes to C. The atom is displaced a distance dX. The excited electron loses some energy in this process and the energy lost is dissipated in the form of an atomic displacement, i.e. as a phonon. When the electron returns to the ground state at D, a new atomic displacement is necessary for the system to relax to its lower energy at A, and takes the form of a phonon emission.

The energy curves of the ground and excited states usually intersect or approach each other closely at some point F. If it has sufficient thermal energy, the atom can move to a configurational position X_F. At F the electron will make a transition to the ground state. In such a process, the photon would not be emitted since when the system relaxes to position X_A, the electron is at the lowest energy state.

We have learned that charge carriers generated in the volume of the material will undergo recombination at a rate corresponding to a volume lifetime τ. They will also diffuse toward the surface due to the gradient in number density and may recombine at the surface at a rate which may be represented by a surface recombination velocity, s. Under these circumstances, the surface acts as a partial absorber for electrons and holes. The charge carriers, which are generated close to the surface of the sample, will recombine more rapidly at the sample surface than the charge carriers generated deep in the volume of the sample. If the sample is sufficiently thin, electrons and holes may recombine on both sample surfaces. The main difference between surface recombination and volume recombination is that the former is non-radiative, while the latter may be significantly radiative, and they are

independent of one another.

The effect of surface recombination has been studied extensively by McKelvey.[50] Consider a diagram of the particle flux interchange between the surface and interior region of the sample, as illustrated by Fig. 8.

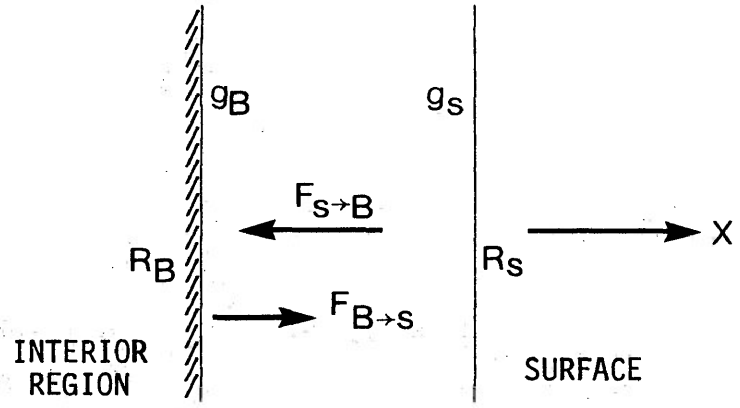

Fig. 8. Flux interchange.

R_B is defined as the probability that a carrier upon entering the crystal will be sent back by the bulk, and R_S the probability that a carrier in a single collision with the surface will be sent back by the surface.

g_B is the flux originating from the interior and g_S is the surface generated flux. $F_{B\to S}$, the particle flux flowing from the bulk to the surface, is made up of g_B plus that part of the flux flowing from the surface to the bulk being reflected by the bulk. $F_{S\to B}$ is the flux flowing from the surface to the interior of the crystal. Therefore

$$F_{B\to S} = g_B + R_B F_{S\to B}$$

$$F_{S\to B} = g_S + R_S F_{B\to S} .$$

The difference between $F_{B\to s}$ and $F_{s\to B}$ is the net flux of carriers, which is equal to the net diffusion current, $-D\, d(\Delta n)/dX$, evaluated at the surface in the absence of an electric field

$$F_{B\to s} - F_{s\to B} = - D \left(\frac{d(\Delta n)}{dX}\right)_{surface} .$$

$F_{B\to s}$ and $F_{s\to B}$ may be obtained on the grounds of general statistics. In the thermal equilibrium condition, the particle concentration, n_0, is the same everywhere, the number of particles per unit time crossing a plane surface of unit area in either direction is just

$$F_{B\to s} = F_{s\to B} = n_0\bar{c}/4 \qquad (\bar{c} \text{ - average thermal velocity}).$$

The surface thermal generation rate, g_s, is clearly equal to the surface recombination rate

$$g_s = (1-R_s)\, n_0\bar{c}/4 ,$$

$(1-R_s)$ being the probability that a particle will be absorbed by the surface.

When a diffusion flow of particles is set up by a concentration gradient

$$F_{B\to s} \neq F_{s\to B} \neq n_0 c/4 .$$

The sum of $F_{B\to s}$ and $F_{s\to B}$ in the surface region can be obtained if the Boltzman distribution is still correct

$$F_{B\to s} + F_{s\to B} = n_s\bar{c}/2$$

where n_s represents the concentration in the neighbourhood of the surface. By solving these equations, one obtains

$$-D\left(\frac{d(\Delta n)}{dX}\right)_{surface} = (n_s-n_0)\,(\bar{c}/2)(1-R_s/1+R_s)$$

$$-D\left[\frac{d(\Delta n)}{dX}\right]_{surface} = s \cdot (\Delta n)_{surface}$$

where $s = (\bar{c}/2)(1-R_s / 1+R_s)$ is the surface recombination velocity. This surface boundary condition is generally written as

$$-D\,[\underset{\sim}{n}\cdot\nabla(\Delta n)]_{surface} = s \cdot (\Delta n)_{surface}$$

where $\underset{\sim}{n}$ is a unit outward vector normal to the surface.

Carrier diffusion processes and carrier recombination at the surface of the photoconductors were studied by DeVore[52] in analyzing the shape of photoconductivity spectral distribution curves. Gergely[53] applied DeVore's diffusion equation in analyzing the shape of cathodoluminescence curves for various types of phosphors. Taking into account the surface recombination and diffusion processes, the nonlinear dependence of cathodoluminescence intensity on the energy of incident electrons could well be explained. For several phosphors, the diffusion length, L, was found to lie in the range $0.05 - 0.15\mu$ and the surface recombination velocity, s, was found to lie in the range $5 \times 10^3 - 5 \times 10^5$ cm/sec.

Recently the Russian workers, Makarov and Petrov,[15] in studying the ionoluminescence and cathodoluminescence of SiC single crystals, claimed that the dependence of the intensity of cathodoluminescence and ionoluminescence on the incident particle energy was governed by the state of the surface of the sample, as well as its impurity content.

The theoretical function, f(R), which allows for the influence of the energy losses in an inactive surface layer and for the non-radiative surface recombination was given by them as

$$f(R) = 1 - Q\frac{L}{R}(1-e^{-R/L})$$

where

$$Q = s / |(D/L) + s|$$

provided that the generation of non-equilibrium carrier pairs along the path of an exciting particle is uniform.

Ionoluminescence

A development of a theoretical treatment of the ionoluminescent processes which contains the mechanisms discussed in the previous sections and which is intended to describe the particular ion-phosphor combinations used in the present work is the topic of this section. The starting points for this development are a continuity equation (5) similar to DeVore's and Lindhard's energy loss theory.

It is assumed that the dimensions of the crystal are much larger than the range R of the incident particle and the diffusion length L_D of the released carriers, the volume lifetime, t, is a constant then for a particular sample.

In consequence of the above assumptions, the problem can be treated as a one-dimensional one. Consider now a thick sample, the particle is incident perpendicular to the surface of the sample in the x-direction. The following notation is used:

$n(x)$ = concentration of charge carriers at a point x in the sample;

L_D = diffusion length of charge carriers;

D = diffusion coefficient of charge carriers;

s = the surface recombination velocity;

$g(x)$ = rate of generation of carrier pairs within the substance.

We consider that $g(x) \propto (-dE/dx)_e$ where $(-dE/dx)_e$ is the energy loss per

unit thickness by the incident particle to the electronic system of the crystal. We assume that the energy loss per unit thickness is a constant

$$-\frac{dE}{dx} = \frac{E_0}{R_p}$$

where E_0 is the projectile initial energy and R_p is the depth of penetration.

Lindhard's theory predicted that the specific energy loss is

$$-\frac{dE}{dR} = N(S_e + S_n).$$

For the case of $^1H^+$, since $S_e >> S_n$, we may write

$$\frac{dE}{dR} = \left(\frac{dE}{dR}\right)_e .$$

Since S_e varies as $E^{\frac{1}{2}}$, the range along the path R also varies as $E^{\frac{1}{2}}$. The projected range, however, varies nearly in direct proportion to E. If the projected range R_p is considered, the rate of generation g(x) will be

$$g(x) \propto E_0/R_p$$

or

$$g(x) = CE_0/R_p$$

where C is a proportionality constant. g(x) is a constant proportional to the energy loss per unit thickness of the stopping medium.

$$g(x) = C\frac{E_0}{R_p} \qquad 0 < x < R_p$$

$$= 0 \qquad x > R_p .$$

Under steady state conditions, dn/dt = 0 and the continuity equation, Eqn. (5), reduces to

$$D(d^2n/dx^2) = n/\tau - g(x). \qquad (6)$$

Substituting $g(x) = CE_0/R_p$ into Eqn. (6) yields

$$D(d^2n/dx^2) = n/\tau - CE_0/R_p$$

or

$$d^2n/dx^2 = n/D\tau - CE_0/DR_p. \qquad (7)$$

For convenience, let $\beta^2 = 1/D\tau$ and $\gamma = CE_0/DR_p$ for $0 < x < R_p$ and $\gamma = 0$ for $x > R_p$. With this notation, Eqn. (7) becomes

$$d^2n/dx^2 = \beta^2 n - \gamma. \qquad (8)$$

The general solutions for Eqn. (8) are

$$n_1(x) = C_1 \exp(\beta x) + C_2 \exp(-\beta x) + \gamma/\beta^2 \qquad 0 < x < R_p$$

$$n_2(x) = C_3 \exp(\beta x) + C_4 \exp(-\beta x) \qquad x > R_p \quad .$$

The constants, C_1, C_2, C_3 and C_4, may be determined from the boundary conditions:

(1) $Dn_1'(0) = sn_1(0)$

(2) $n_1(R_p) = n_2(R_p)$

(3) $n_1'(R_p) = n_2'(R_p)$

(4) $n_2(x) = 0$ if $x \to \infty$

where the prime indicates a derivative. The values of the constants thus obtained are

$$C_1 = -\gamma \exp(-\beta R_p)/2\beta^2$$

$$C_2 = [\gamma \exp(-\beta R_p)/2\beta^2)(s/D\beta+s)(1-D\beta/s-2\exp(\beta R_p)]$$

$$C_3 = 0$$

$$C_4 = C_2 - C_1 \exp(2\beta R_p).$$

The total number of carrier pairs generated is

$$N_0 = \int_0^{R_p} n_1(x)\,dx + \int_{R_p}^{\infty} n_2(x)\,dx.$$

We assume that the intensity of the light produced is proportional to the total number of carrier pairs generated

$$L(E) \propto N_0/\tau$$

where τ is the lifetime of the carriers.

$$L(E) \propto 1/\tau \left\{ \int_0^{R_p} n_1(x)\,dx + \int_{R_p}^{\infty} n_2(x)\,dx \right\}$$

$$L(E) = C'/\tau \left\{ \int_0^{R_p} n_1(x)\,dx + \int_{R_p}^{\infty} n_2(dx)\,dx \right\} .$$

After integrating and rearranging, we obtained

$$L(E) = k'E_0 \left\{ 1 - QL_D/R_p \; (1-\exp(-R_p / L_D)) \right\} \quad , \qquad (9)$$

where $k' = C'C$, $L_D = 1/\beta$, the diffusion length of the carriers, and $Q = s/|s+(D/L_D)|$ is a surface recombination loss parameter. For hydrogen ions at high energy where $R_p >> L_D$, Eqn. (9) reduces to

$$L_H \simeq k'E_0.$$

For the case of heavy ions where nuclear collisions compete with electronic collisions, a projectile energy distribution function within the sample is approximated as follows. It is assumed that the energy

loss per unit thickness is a constant

$$-\frac{dE}{dx} = \frac{E_0}{R_p}$$

where R_p is the depth of penetration. Integrating from the surface (x=0) where the particle's incident energy is E_0 to a point x from the surface where the particle's energy has been reduced to E gives

$$-\int_{E_0}^{E} dE = \frac{E}{R_p}\int_{0}^{x} dx$$

$$-E + E_0 = E_0 x / R_p$$

$$E = E_0 \ (1 - x / R_p)$$

Since the stopping power is expressed in terms of the range along the path a range correction factor must be introduced to estimate the energy loss per unit distance from the surface:

$$(-dE/dx)_e = \alpha_R \ (-dE/dR)_e.$$

The rate of generation g(x) is then

$$g(x) \propto (-dE/dx)_e = \alpha_R(-dE/dR)_e = \alpha_R NKE^{\frac{1}{2}}$$

or

$$g(x) = C\alpha_R NKE^{\frac{1}{2}}.$$

For the case of $^{40}Ar^{+}$ ions falling on ZnS, α_R takes the form[12]

$$\alpha_R = 1 + \mu/3 \simeq 4/3$$

where

$$\mu = M_2 / M_1 \simeq 1.$$

$g(x)$ for $^{40}Ar^{+}$ ions on ZnS will then be

$$g(x) = \frac{4}{3} CNKE_0^{\frac{1}{2}} (1 - x/R_p) \qquad \text{for} \quad 0 < x < R_p$$
$$g(x) = 0 \qquad \text{for} \quad x > R_p \ . \tag{10}$$

Applying the steady state continuity equation (6) and substituting Eqn. (10)

$$d^2n(x)/dx^2 = \beta^2 n(x) - \gamma'(1 - x/R_p) \tag{11}$$

results, where $\gamma' = \frac{4CNKE^{\frac{1}{2}}}{3D}$.

Introducing the new variable, $y = \beta(R_p - x)$, Eqn. (11) becomes

$$\frac{d^2n(y)}{dy^2} - n(y) = - \frac{\gamma y^{\frac{1}{2}}}{\beta^{\frac{5}{2}} R_p^{\frac{1}{2}}} \ .$$

The general solutions to this equation are

$$n_1(y) = C_1 \exp(y) + C_2 \exp(-y) - \frac{\gamma}{\beta^{\frac{5}{2}} R_p^{\frac{1}{2}}} \sum_{j=1}^{\infty} \frac{y^{2j + \frac{1}{2}}}{\prod_{k=1}^{2j} (k - \frac{1}{2})} \qquad 0 < x < R_p$$

and

$$n_2(y) = C_3 \exp(y) + C_4 \exp(-y) \qquad x > R_p \ . \tag{12}$$

In terms of the new variable, the boundary conditions become

$$(1) \quad -Dn_1'(\beta R_p) = S_n(\beta R_p)$$
$$(2) \quad n_1(0) = n_2(0)$$
$$(3) \quad n_1'(0) = n_2'(0)$$
$$(4) \quad n_2(y) = 0 \quad \text{if} \quad y \to \infty \ . \tag{13}$$

The values of the constants in Eqns. (12) that satisfy Eqns. (13) are

$$C_1 = C_3 = \frac{s\gamma R_p{}^2 \exp(-\beta R_p)}{(s+D\beta)} \sum_{j=0}^{\infty} \frac{(\beta R_p)^{2j}}{\prod_{k=1}^{2j+2} (k+\frac{1}{2})} + \frac{\gamma R_p \exp(-\beta R_p)}{(s+D\beta)} \sum_{j=0}^{\infty} \frac{(\beta R_p)^{2j}}{\prod_{k=1}^{2j+1} (k+\frac{1}{2})}$$

and $$C_2 = C_4 = 0.$$

The total number of carrier pairs generated is therefore

$$N_0 = \beta^{-1} \int_0^{\beta R_p} n_1(y)\,dy + \beta^{-1} \int_{-\infty}^{0} n_2(y)\,dy$$

and the light produced is

$$L(E) = \frac{N_0}{\tau} = 1/\tau \left\{ \beta^{-1} \int_0^{\beta R_p} n_1(y)\,dy + \beta^{-1} \int_{-\infty}^{0} n_2(y)\,dy \right\}$$

or

$$L(E) = \frac{C'}{\tau} \left\{ \beta^{-1} \int_0^{\beta R_p} n_1(y)\,dy + \beta^{-1} \int_{-\infty}^{0} n_2(y)\,dy \right\}.$$

After integration and rearranging, there results for argon

$$L_A = C'C \frac{4}{3} N K E_0{}^{\frac{1}{2}} R_p{}^{\frac{2}{3}} \left\{ 1 - \frac{3}{2} Q \sum_{j=0}^{\infty} \frac{(-R_p/L_D)^j}{\prod_{k=1}^{j+1} (k+\frac{1}{2})} \right\}$$

$$\simeq k' E_e{}^0 \left\{ 1 - \frac{3}{2} Q \sum_{j=0}^{\infty} \frac{(-R_p/L_D)^j}{\prod_{k=1}^{j+1} (k+\frac{1}{2})} \right\} \qquad (14)$$

where $E_e{}^0 = N S_e(E_0) R_p$ and k', Q and L_D have the same meaning as before.

In general, we may write Eqns. (9) and (14) in the following form for hydrogen

$$L_H(E) = k' E_0 f_H(R_p / L_D)$$

where

$$f_H = 1 - Q \frac{L_D}{R_p} (1 - \exp(-R_p / L_D)) \qquad (15)$$

and for argon in the form

$$L_A = k' E_e{}^0 f_A(R_p / L_D)$$

where

$$f_A = 1 - \frac{3}{2} Q \sum_{j=0}^{\infty} \frac{(-R_p/L_D)^j}{\prod_{k=1}^{j+1} (k+\ )} .$$

A comparison plot of f_H and f_A *versus* R_p/L_D is shown in Fig. 9 for Q=1, Q=0.5 and Q=0. If we put Q=0, we may expect that Eqns. (9) and (14) should reduce to Eqn. (1). The result of such a comparison is displayed in Fig. 10.

For the case of $^{40}Ar^+$ ions penetrating NaI(Tl), to the first approximation, and over-estimating the nuclear stopping, we may write the range correction factor, $\alpha_R(E)$, as

$$\alpha_R(E) \simeq \mu S_n/S_e .$$

Here S_n is considered a constant, corresponding to the r^{-2} potential between atoms. Thus we may write the generation rate, g(x), as

$$g(x) \propto dE_e/dx = \alpha_R(E)\, dE/dr$$

$$\propto \mu S_n N$$

or

$$g(x) = C \mu S_n N$$

which is a constant.

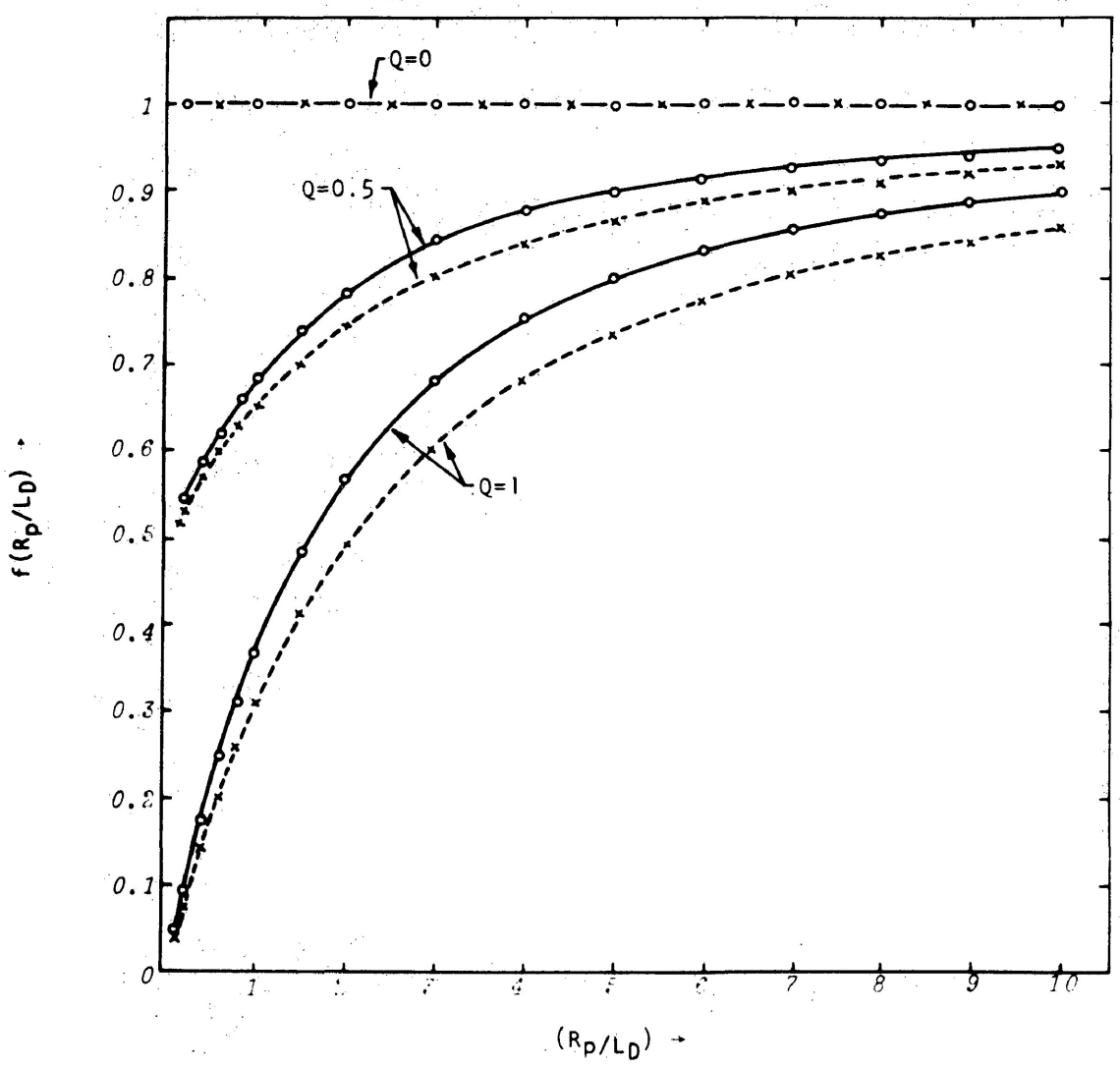

Fig. 9. A composite plot of f_H (o—o) and f_A (×---×) *versus* (R_p/L_D) for Q = 0, 0.5 and 1.

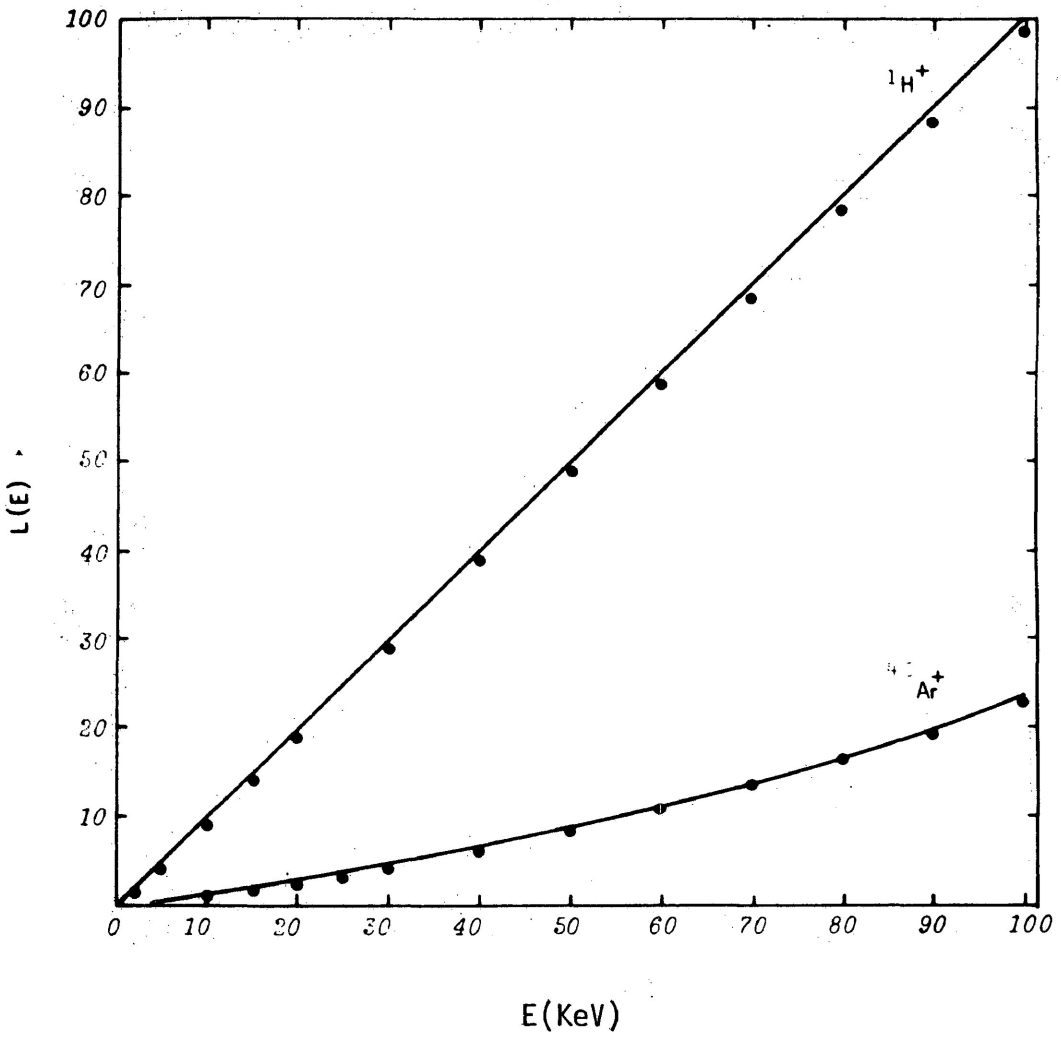

Fig. 10. The solid curves are calculated from Eqns. (9) and (14) with Q = 0 and k' = 1. The points (·) are obtained from Eqn. (1) with C = 1 for both $^1H^+$ and $^{40}Ar^+$ in ZnS.

Using the same approach as above for $^{40}Ar^{+}$ ions on a NaI(Tℓ) target, L(E) takes the form

$$L(E) = k'\mu N S_n R_p \left\{1 - Q \frac{L_D}{R_p} (1 - \exp(R_p / L_D))\right\} \qquad (16)$$

$$L(E) = k'\mu N S_n R_p f(R_p / L_D)$$

where

$$f(R_p / L_D) = 1 - Q \frac{L_D}{R_p} (1 - \exp(-R_p / L_D))$$

which is identical to Eqn. (15).

IV.

APPARATUS AND TECHNIQUE

The general principle of operation of the apparatus is illustrated

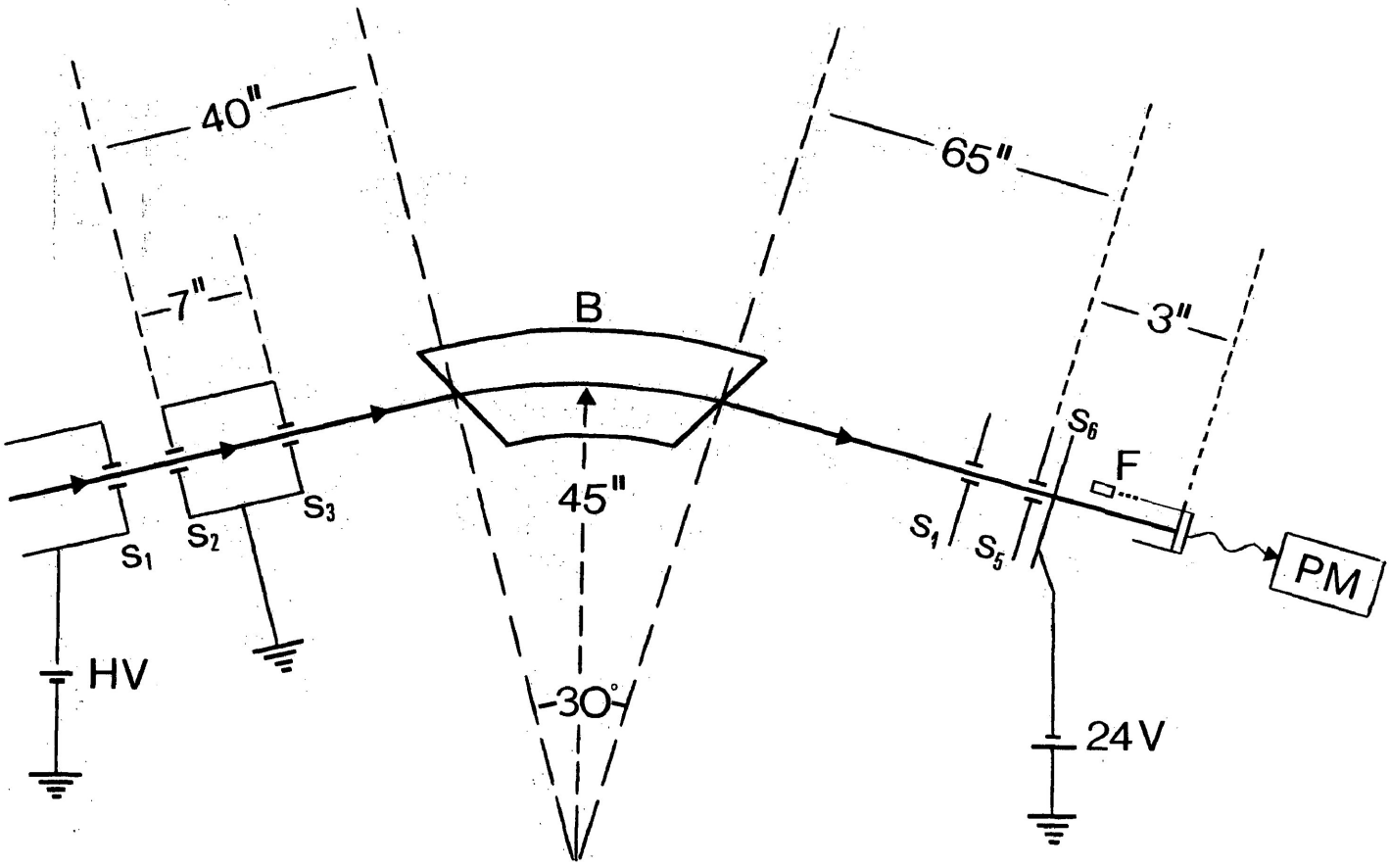

Fig. 11. Schematic diagram of the apparatus.

in Fig. 11. Positive ions produced in a gas—electron bombardment source are accelerated between slits S_1 and S_2 by a high voltage power supply, HV (UVC Model BAL-130-1.5-LU), whose output potential could be varied from 0 to 130 KV and which was calibrated to an accuracy of ±1.5 percent.

After acceleration, the ion beam passed through a collimating stage

consisting of slit S_3 and was directed into a magnetic field B, produced by an electromagnet, which separated the various types of ions present in the beam. The desired ion beam, in travelling a circular path of radius 45", was bent through an angle of 30°. The ion beam was then further collimated by the second collimating stage consisting of the slit system, S_4 and S_5. The ion beam is collected in a small Faraday cup, F, and the beam current is measured by means of a high speed electrometer (Keithley Model 416). In order to prevent secondary electrons from entering or leaving the Faraday cup, slit S_6 is kept at a negative potential of 24 volts. The dimensions of the slits, S_1, S_2 and S_3, are approximately 0.01" by 0.50". The divergence of the ion beam is sufficiently large to produce an approximately uniform ion distribution over the area of S_5 so that the irradiation was effectively distributed over a corresponding area of the sample.

The Faraday cup and the cylindrical sample holder were connected together and could be moved in an arc perpendicular to the ion beam by means of a bellows system. When the cup moved out of the ion beam, the ion beam impinged upon the sample.

The sample consisted of a thin layer of tiny phosphor crystals deposited to a depth of a few tenths of a millimeter on a 1.5" diameter quartz disk held by a metal ring. In order to minimize the deterioration of the phosphor samples under prolonged ion bombardment during the course of the experiments, they were scanned rapidly across the beam.

The sample disk was first moved so that the sample was not in the path of the ion beam, the ion beam was collected in the Faraday cup as shown in Fig. 12. After the ion current was determined, the Faraday cup was retracted and the phosphor sample then scanned perpendicularly across

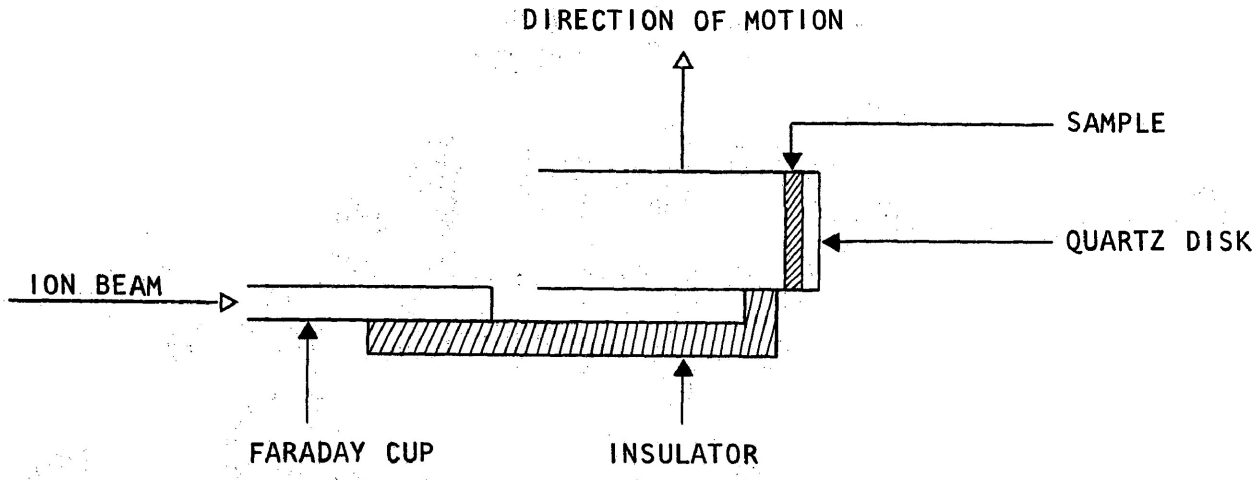

Fig. 12. The arrangement of the Faraday cup and the sample holder.

the path of the ion beam. The Faraday cup was then reinserted into the beam and a second determination of the ion current was made. The mean time taken to scan a sample across the ion beam was less than 5 seconds. As the sample passed across the ion beam, light emitted from the bombarded sample was detected by means of a photomultiplier tube PM (EMI Type 9653Qb) whose output was registered on a Keithley electrometer (Keithley Model 410A). The d-c output of the electrometer was retained on the same recorder used for the ion current, which indicated the luminescence response of the sample to the ion bombardment. The purpose of the second collimating stage is to ensure that the ion beam impinges upon the sample in a fixed position relative to the photomultiplier tube, so that the geometrical distribution of the illumination on the photosensitive surface of the photomultiplier tube was constant. The target chamber was made of brass and was maintained at a pressure of about 1×10^{-7} torr. The pressure in the first collimating stage was maintained at about 5×10^{-6} torr.

The photomultiplier tube is provided with a Spectrosil (fused silica) window, giving a useful spectral range from 6500 Å down to 1650 Å. The major portions of the luminescent spectra of all the samples studied fell

within the range of sensitivity of the photomultiplier.[61] The tube was mounted in a mu-metal shield (EMI Type ps 6B) to reduce the variation in the photomultiplier output current due to stray magnetic fields from the magnetic analyzer.

Fig. 13 which is made with a two-pen recorder illustrates the type of recorder tracing observed in the experiments. I_i is the ion

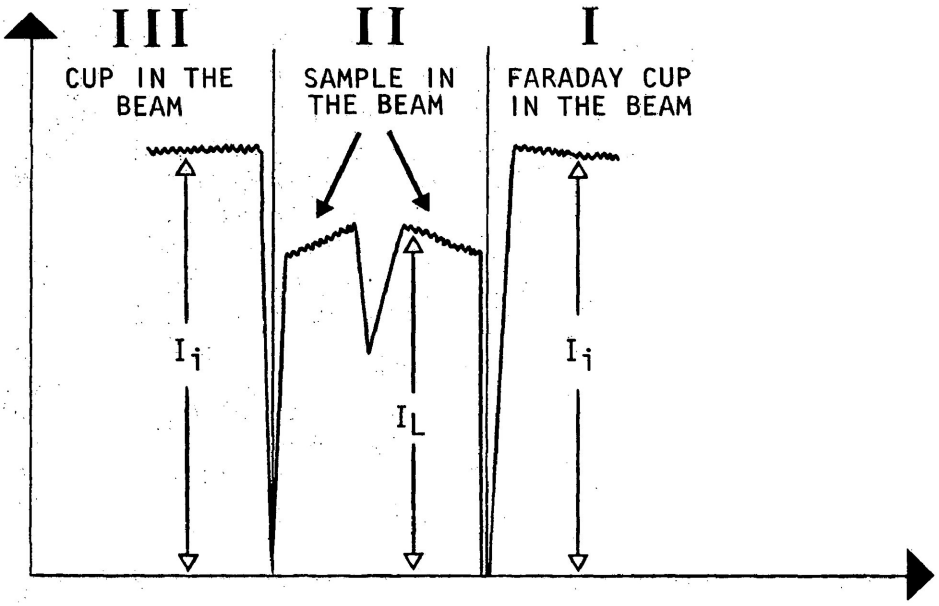

Fig. 13. A reproduction of a two-pen recorder tracing showing the ion beam current, I_i, and the photomultiplier current, I_L, as the sample is scanned across the ion beam.

beam current and I_L is the photomultiplier output current. The ion beam current (I_i) is measured by means of a Keithley electrometer (Keithley Model 416) which has an accuracy of ± 3 percent of full scale on the 3×10^{-9} to 10^{-13} ampere ranges. The reading accuracy of the meter is about 0.5 percent. In the present experiments, the ion beam current readings were obtained with the electrometer on the 10^{-12} and 3×10^{-12} ampere scale. In these ranges, the linearity of the meter was about

0.5 percent. All of the photomultiplier output currents (I_L) were measured with a Keithley electrometer (Model 410A) on the 10^{-8} to 10^{-4} ampere scale, accurate to about 0.5 percent. Therefore L, which is I_L/I_i, has a random error of about 1-2 percent and possibly a systematic error of about 6 percent. The larger systematic error is of little consequence since it does not affect the *relative* values of L.

The phosphor samples were prepared by first suspending the tiny phosphor crystals in methanol. This suspension was then poured into a container with the quartz disk supported near the bottom. The phosphor particles settled from the mixture and formed an even coating on the surface of the slide. The alcohol was then drained away and the sample allowed to dry. The uniformity of the surface layer of the sample depended on the speed of draining. The rate of deposition of the phosphor from the suspension varies with the particle size, being slower for the smaller particles.

In order to ensure that the values $L = I_L/I_i$ were representative of the undamaged sample during the course of the experiments, the sample was first bombarded with the lightest ion, $^1H^+$, and then with $^4H^+$, $^{14}N^+$, $^{20}Ne^+$ and $^{40}Ar^+$ in that order. The value of L under $^1H^+$ bombardment was then rechecked after each run. No significant changes were observed.

V.

RESULTS

The light output as a function of energy was determined at room temperature for the luminescent materials listed in Table I. The integrated light output from the samples was found to be directly proportional to the ion current in the range 10^{-13} to 10^{-12} ampere. In such an ion current range, the irradiation dose per scan is roughly $3 \times 10^{7} - 3 \times 10^{8}$ ions/cm^2, since the area of the slit is 0.1 cm^2 and the scanning time is 5 sec. According to the results of earlier workers[15,57] such a dose is negligible and will not induce any appreciable damage. Thus the light output per unit ion current, L, is a measure of the light output per impinging ion.

A composite plot of the relative luminescence efficiency of the phosphors and scintillation crystals under bombardment with $^{1}H^{+}$ ions, as a function of energy, is shown in Fig. 14 on a double logarthmic scale. It was found that ZnS:Ag (P-22 G.E.) has the highest ionoluminescent response and the scintillator Plastifluor has the lowest ionoluminescent response. We have given the L values of ZnS:Ag (P-22 G.E.) for a 100 KeV $^{1}H^{+}$ ion a value of 100. The light output for the other samples was then normalized so that Fig. 14 indicates the relative efficiency. The results showed that the ionoluminescent response is a sensitive function of ion energy. In the energy range studied, the experimental points lie approximately on straight lines for ion energies below 100 KeV, with different shapes for different samples. It is seen that of the powdered phosphors the ZnS samples (curves 1,

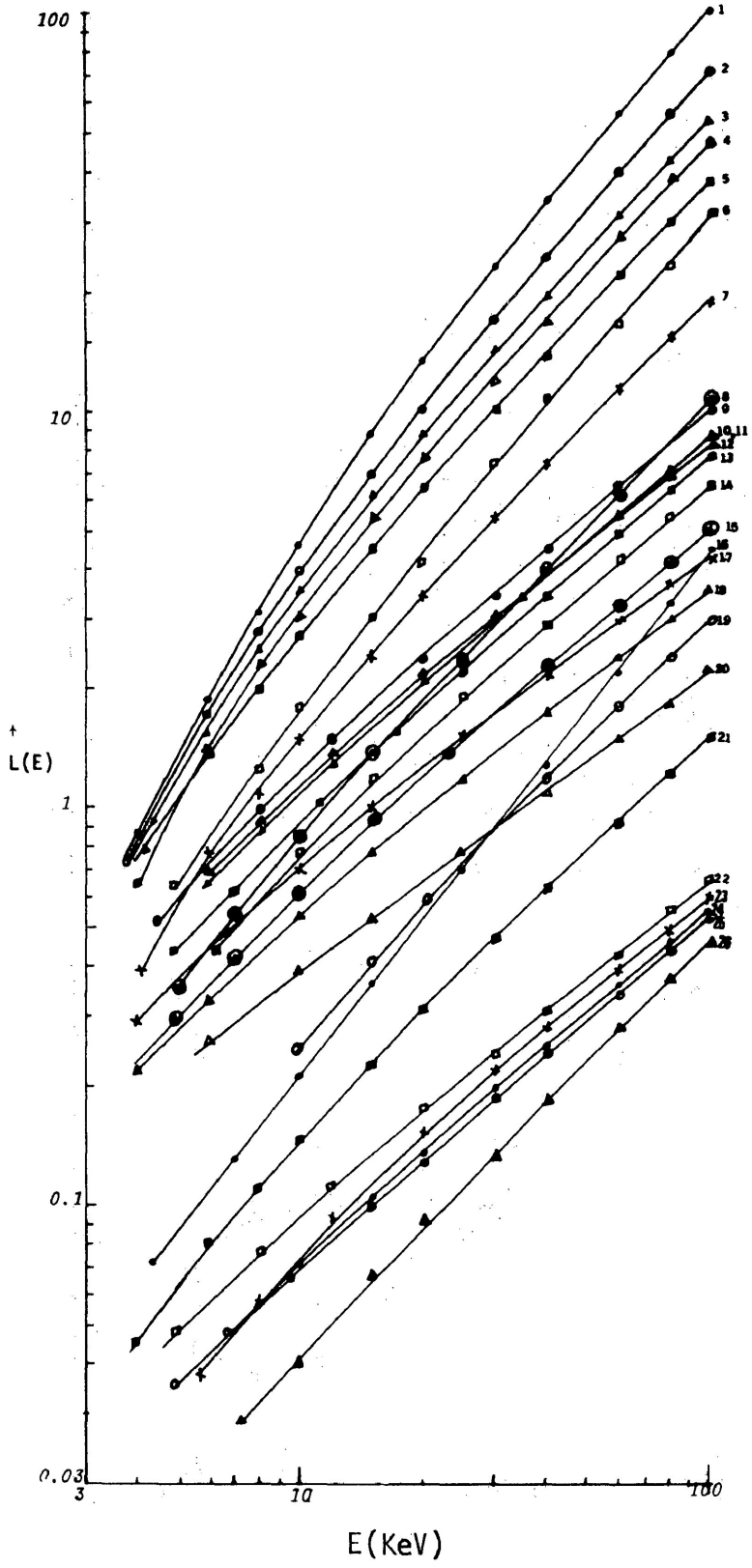

Fig. 14. Relative luminescence efficiency of the phosphors and scintillation crystals under $^{1}H^{+}$ bombardment.

2, 3, 4 and 6) and the ZnCdS samples (curves 5 and 7) have the higher luminescence efficiencies and of the scintillators NaI(Tℓ) (curve 17), CsI(Tℓ) (curve 8) and CsI(Na) (curve 19) are the best. In general, the light output L varies approximately with the incident ion energy E according to the relation $L \propto E^{w}$, and it may be classified into three groups in which $w \approx 1$, $w < 1$ and $w > 1$ as follows:

$w \approx 1$		$w < 1$		$w < 1$	
Zn_2SiO_4:Mn	(9-14)	$CaWO_4$	(16,18)	ZnS	(1,2,3,4,6)
ZnO:Zn	(15)	Stilbene	(20)	ZnCdS	(5,7)
CsI(Na)	(19)	YVO_4:Eu	(24)	CsI(Tℓ)	(8)
Y_2O_2S:Eu	(21)	YVO_4:Eu,Bi	(22)	NaI(Tℓ)	(7)
Plastifluor	(26)	$KMgF_3$:Mn	(23)		
		Plastifluor (polished)	(25)		

The numbers in parentheses refer to the samples in Table I and Appendix III.

The values of the relative luminescent response of all the samples studied at 10 KeV, 50 KeV and 100 KeV energy under $^{1}H^{+}$ bombardment are given in Table I.

The optical and physical properties of the samples are given in Table II (Appendix III). The scintillators NaI(Tℓ), CsI(Tℓ), CsI(Na), Plastifluor and stilbene were purchased from Isomet Corporation and the powdered phosphors were purchased from the General Electric Company and the Sylvania Company.

In these experiments, the scintillation crystals have been subjected to various surface treatments. Curve 26 in Fig. 14 represents the luminescent response of Plastifluor without any surface treatment and curve 25 is the luminescent response curve of the same Plastifluor which

TABLE I

NO.	SAMPLE			10 KeV	50 KeV	100 KeV
1	ZnS:Ag	(P-22)	GE	4.57	41.6	100
2	ZnS:Ag	(P-11)	GE	3.97	31	69
3	ZnS:Ag	(P-11)	GE ultra fine**	3.54	25	53
4	ZnS:Ag:Cu	(P-2)	GE	3.00	22	46.5
5	ZnCdS:Ag	(P-22)	GE	2.72	17.5	37
6	ZnS:Cu	(P-31)	GE	2.47	12.5	31
7	ZnCdS:Ag	(P-20)	GE	1.51	9.3	18.6
8	CsI(Tℓ)			0.92	4.9	10.8
9	Zn_2SiO_4:Mn	(P-1)	GE	1.25	5.4	9.9
10	Zn_2SiO_4:Mn	(P-1)	Sylvania #161	1.09	4.7	8.6
11	Zn_2SiO_4:Mn	(P-1)	Sylvania #221	1.16	4.6	8.5
12	Zn_2SiO_4:Mn	(P-1)	GE	0.92	4.2	7.8
13	Zn_2SiO_4:Mn	(P-1)	Sylvania #160	0.85	4.1	7.6
14	Zn_2SiO_4:Mn	(P-1)	GE	0.77	3.5	6.4
15	ZnO:Zn	(P-15)	Sylvania #137	0.61	2.7	5
16	$CaWO_4$		GE regular	0.70	3.60	4.4
17	*NaI(Tℓ)			0.20	1.70	4.4
18	CaWO		GE fine	0.53	2.10	3.5
19	*CsI(Na)			0.25	1.50	3
20	*Stilbene			0.4	1.30	2.2
21	Y_2O_2S:Eu	(P-22)	GE	0.14	0.76	1.47
22	YVO_4:Eu,Bi	(P-22)	GE	0.11	0.37	0.65
23	$KMgF_3$:Mn	(P-19)	GE	0.075	0.33	0.60
24	YVO_4:Eu	(P-22)	GE	0.068	0.32	0.55
25	*Plastifluor		(Polished)	0.07	0.30	0.43
26	*Plastifluor			0.04	0.21	0.43

*1 in. diameter, ¼ in. thick blanks.

**Details of particle sizes are given in Table II, Appendix III.

has been polished with 5 micron alumina; the two curves are non-parallel and show rather different behavior at low energies. Curve 17 represents the results for NaI(Tℓ) dry polished with extra fine emery polishing paper. Curves 8 and 19 represent the results for CsI(Tℓ) and CsI(Na), respectively, both polished with paper and lens tissue. The ZnS response curves with different activators and different particle size are non-parallel and cross each other at very low energy. Moreover, the Zn_2SiO_4:Mn curves corresponding to different particle sizes show slightly different luminescent responses. It is evident that surface treatment affected considerably the luminescence yield and the shape of the curves. This strongly suggests that ionoluminescence is affected both by the method of the surface treatment and by the type and amount of impurity present in the crystal.

The low light output of organic scintillators, such as stilbene and Plastifluor, may be due to two causes:

1. The scintillators are of low density materials and contain only elements of low atomic number (H = 1, C = 6), and
2. High self-absorption in contrast to NaI(Tℓ) and CsI(Tℓ) which are of small self-absorption.[29]

The rare-earth-activated red emission phosphors, such as europium-activated yttrium vanadate and yttrium oxysulfide, and europium-bismuth-activated yttrium vanadate, in general, have much lower light output than the other phosphors. This may be due to the different transition mechanism associated with the rare-earth center, in which the electronic transitions occur in inner shells, producing an emission spectrum which consists of narrow lines.

Scintillation Crystals

Figs. 15 to 21 show the observed relative light output per impinging ion L as a function of ion energy E on a linear scale for various ions bombarding samples of Plastifluor, stilbene, NaI(Tℓ), CsI(Tℓ) and CsI(Na). The experimental values were all obtained at room temperature. The observed value of the light produced by $^{1}H^{+}$ at 100 KeV was normalized to a value of 100. All other values for a particular scintillator were normalized using the same constant. Results of the measurements performed using the organic solid solution scintillator, Plastifluor, are shown in Fig. 15 and Fig. 16. In Fig. 15 the relative light output L under $^{1}H^{+}$ ion bombardment has a linear relationship with the ion energy E within the experimental uncertainty over the entire energy region investigated. The L *versus* E relation for $^{4}He^{+}$ and $^{14}N^{+}$ is not linear, with curvatures concave and convex toward the energy axis. Fig. 16 shows the results for Plastifluor polished with 5 micron alumina. The slope of the curve decreased with increasing ion energy for $^{1}H^{+}$ and became nearly constant above 20 KeV. A comparison plot of L *versus* E curves for two types of Plastifluor scintillator, as displayed in Fig. 17, illustrates clearly the difference in luminescent response from unpolished Plastifluor to that from polished Plastifluor when bombarded by ions. The ratio of light output from polished Plastifluor to that from unpolished Plastifluor is roughly (1.4-2):1 for $^{1}H^{+}$ and $^{4}He^{+}$ and (2-3):1 for $^{14}N^{+}$. Results of observation showed that surface polishing greatly improved the luminescent response of the crystals, especially for heavy ions. This indicated that an energy degrading surface existed on the unpolished Plastifluor which reduced the light output.

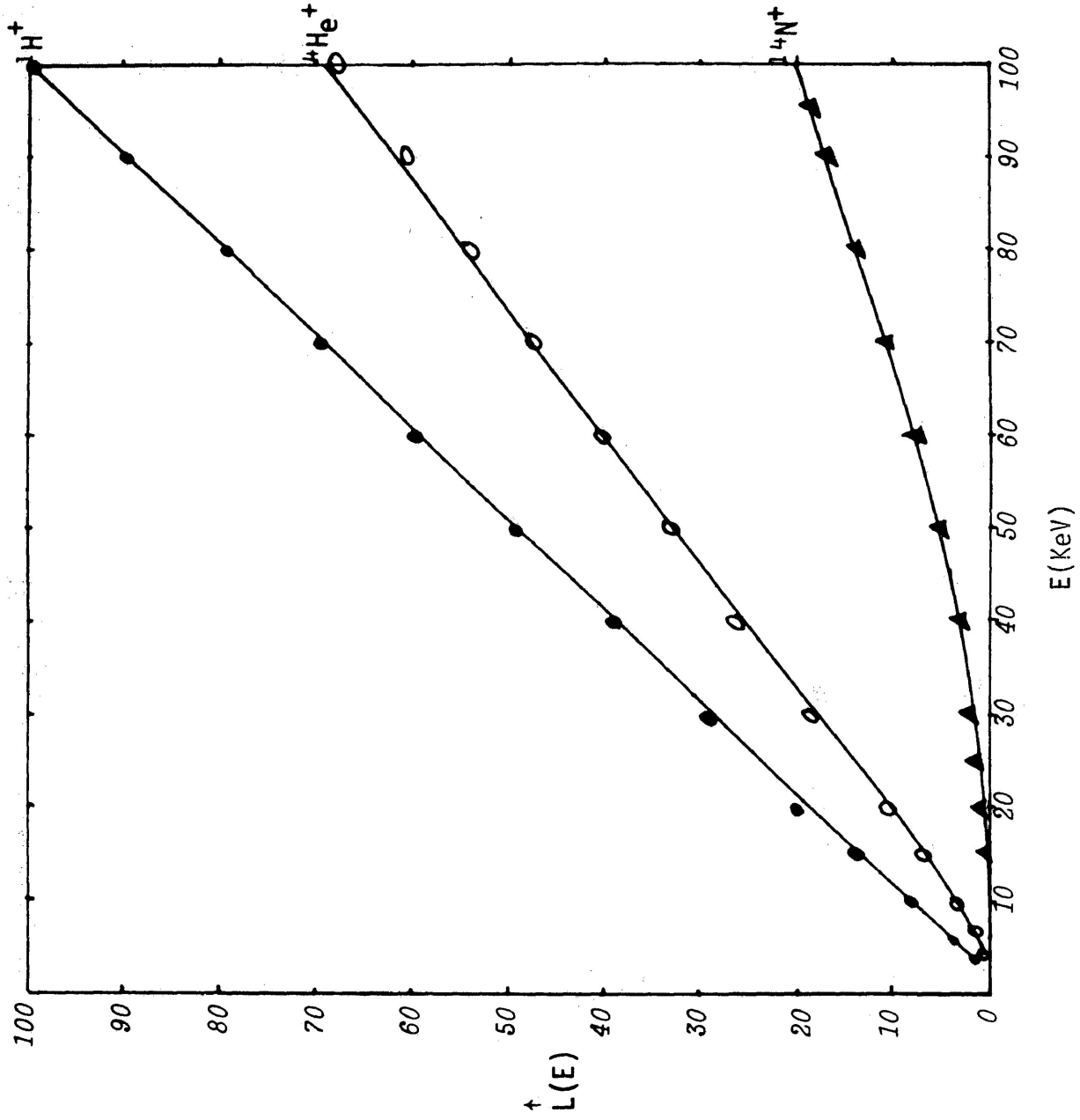

Fig. 15. A linear plot of L *versus* E for $^1H^+$, $^4He^+$ and $^{14}N^+$ ions impinging on Plastifluor.

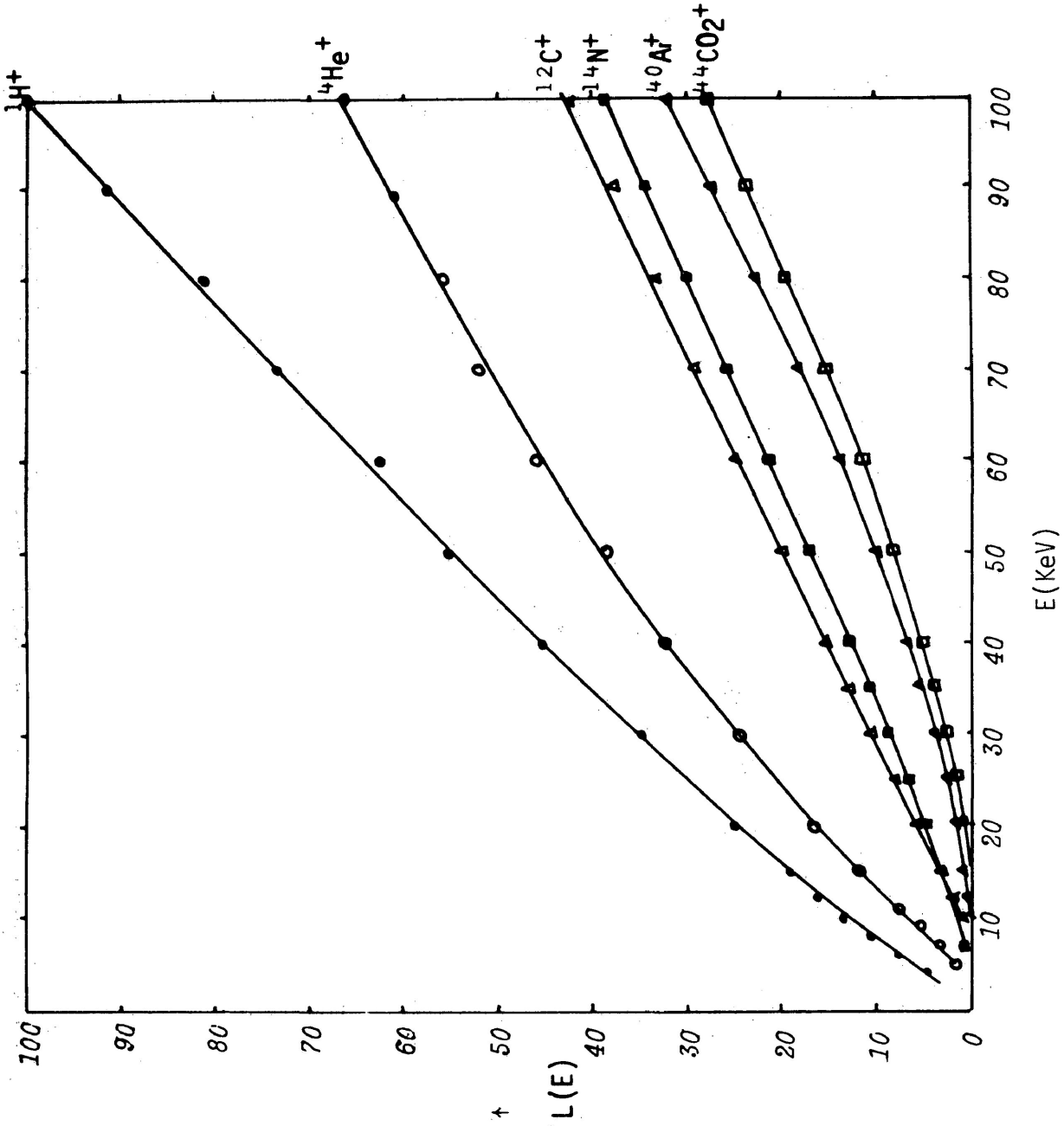

Fig. 16. A linear plot of L *versus* E for $^{1}H^{+}$, $^{4}He^{+}$, $^{12}C^{+}$, $^{14}N^{+}$, $^{40}Ar^{+}$ and $^{44}CO_2^{+}$ ions impinging on Plastifluor polished with 5 micron alumina.

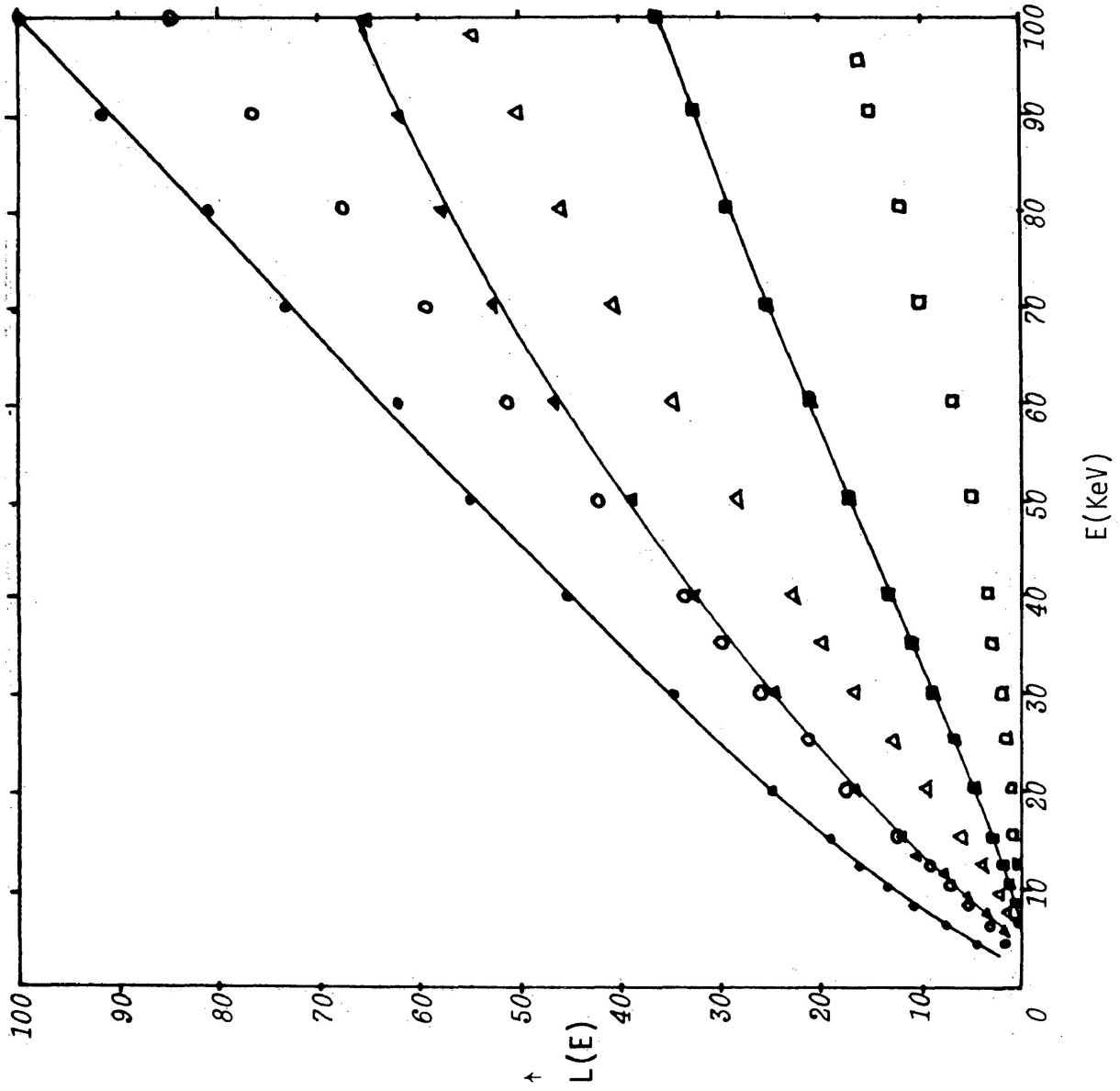

Fig. 17. Composite plot of L *versus* E for $^{1}H^{+}$, $^{4}He^{+}$ and $^{14}N^{+}$ ions impinging on polished Plastifluor ($^{1}H^{+}$(●); $^{4}He^{+}$(▲); $^{14}N^{+}$(■)) and unpolished Plastifluor ($^{1}H^{+}$(o); $^{4}He^{+}$(Δ); $^{14}N^{+}$(□)). The solid curves are drawn through the points of polished Plastifluor.

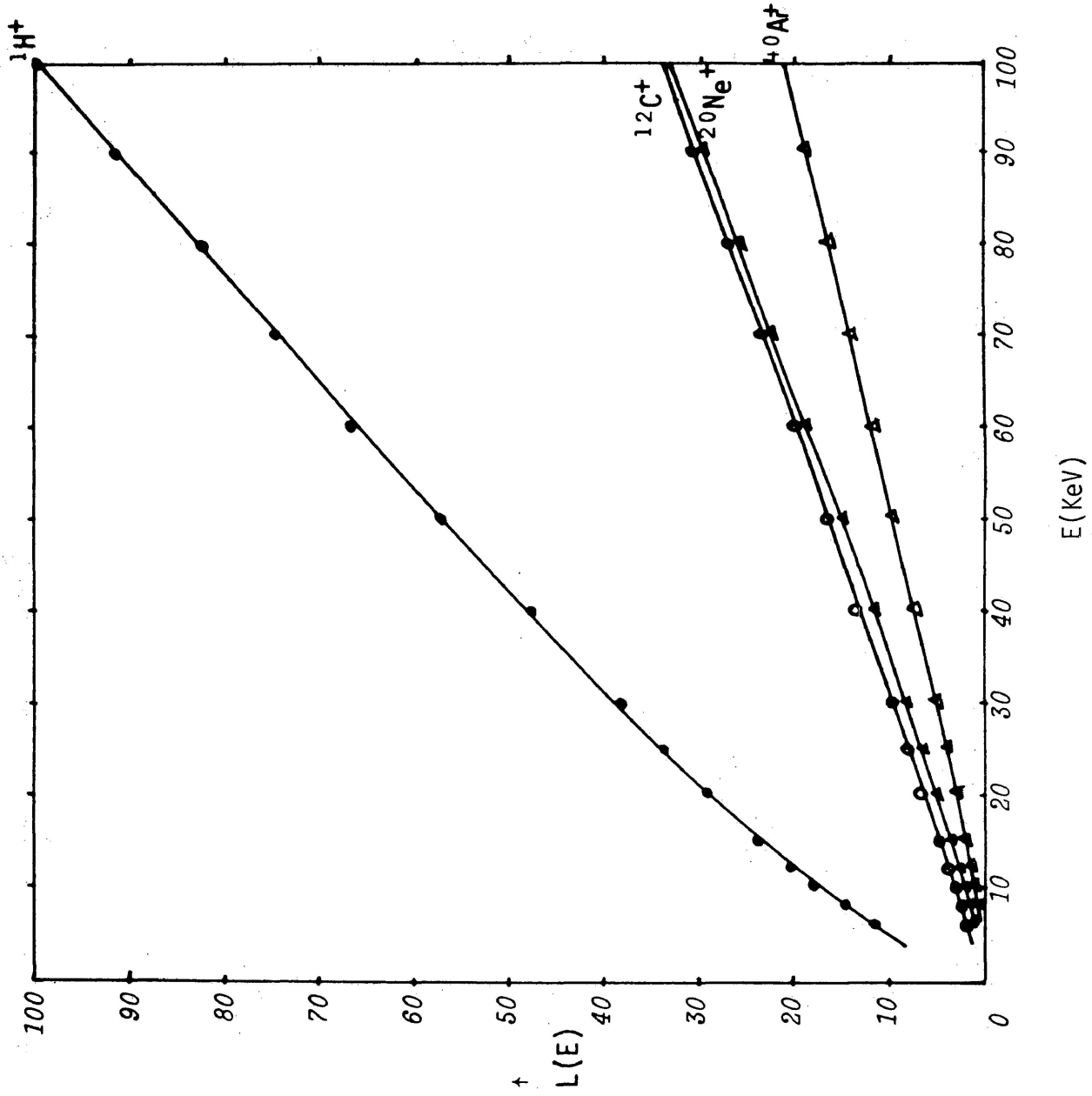

Fig. 18. A linear plot of L *versus* E for $^{1}H^{+}$, $^{12}C^{+}$, $^{20}Ne^{+}$ and $^{40}Ar^{+}$ ions impinging on stilbene.

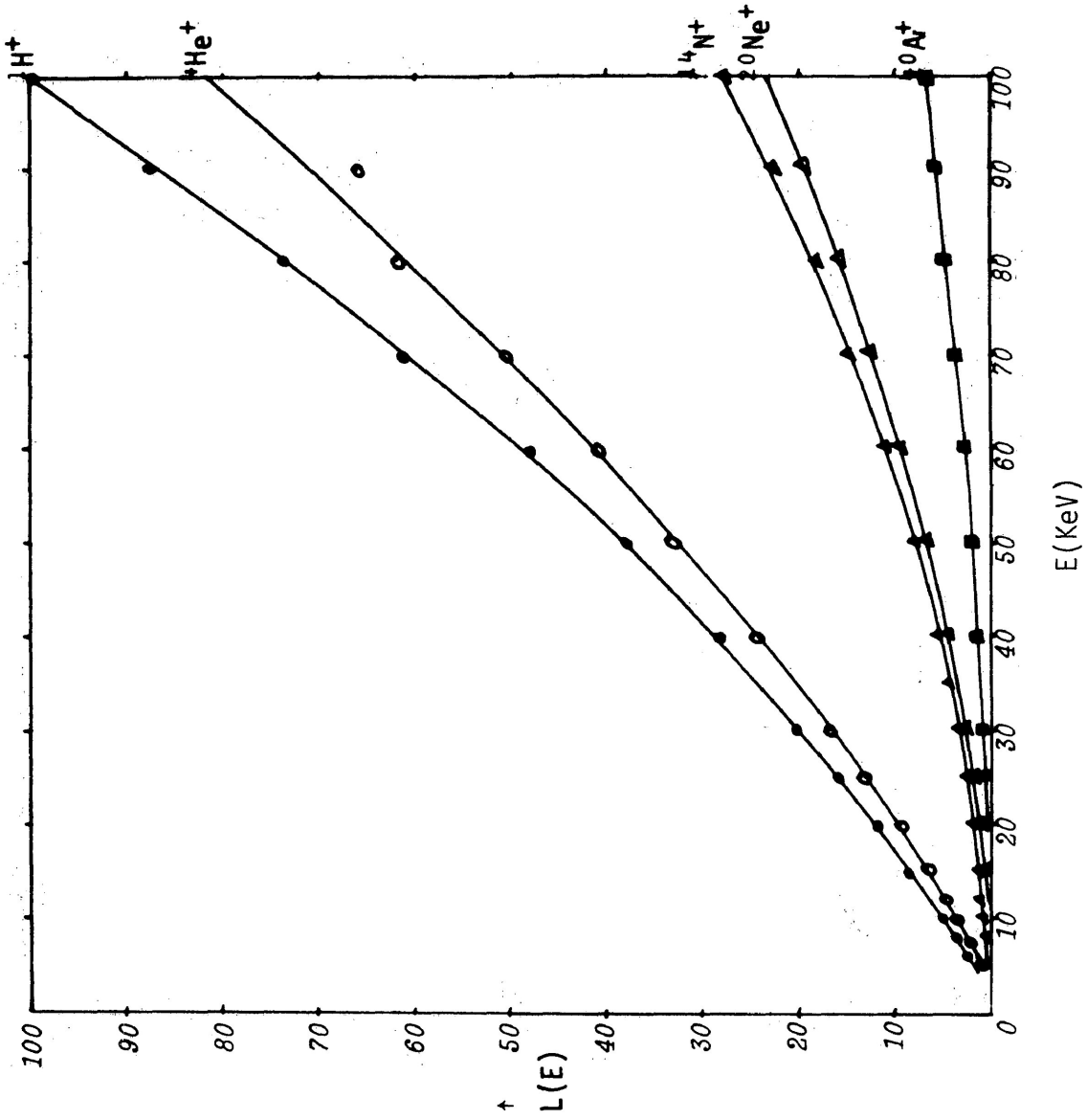

Fig. 19. A linear plot of L *versus* E for $^{1}H^{+}$, $^{4}He^{+}$, $^{14}N^{+}$, $^{20}Ne^{+}$ and $^{40}Ar^{+}$ ions impinging on NaI(Tl).

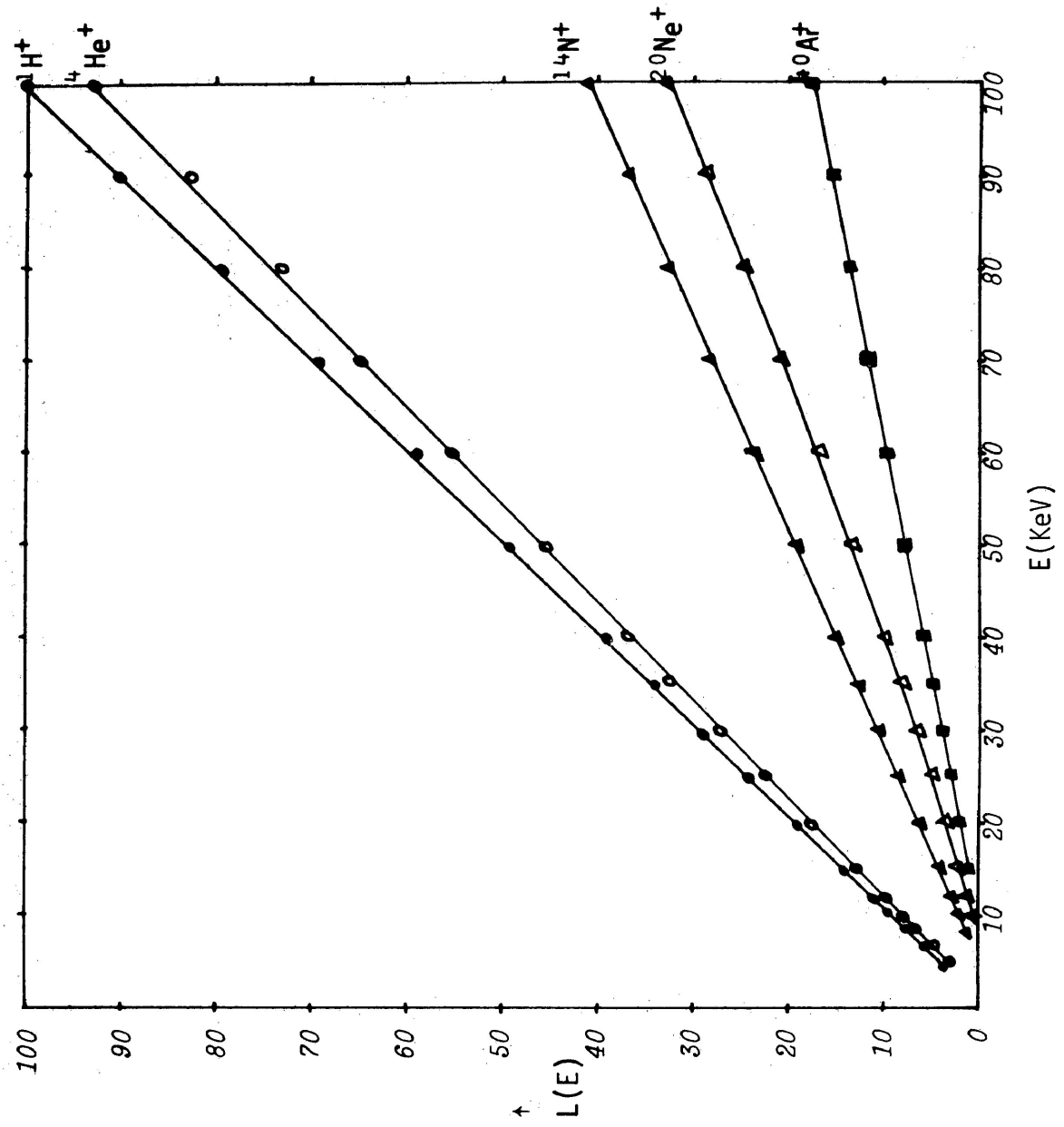

Fig. 20. A linear plot of L *versus* E for $^{1}H^{+}$, $^{4}He^{+}$, $^{14}N^{+}$, $^{20}Ne^{+}$ and $^{40}Ar^{+}$ ions impinging on CsI(Tl).

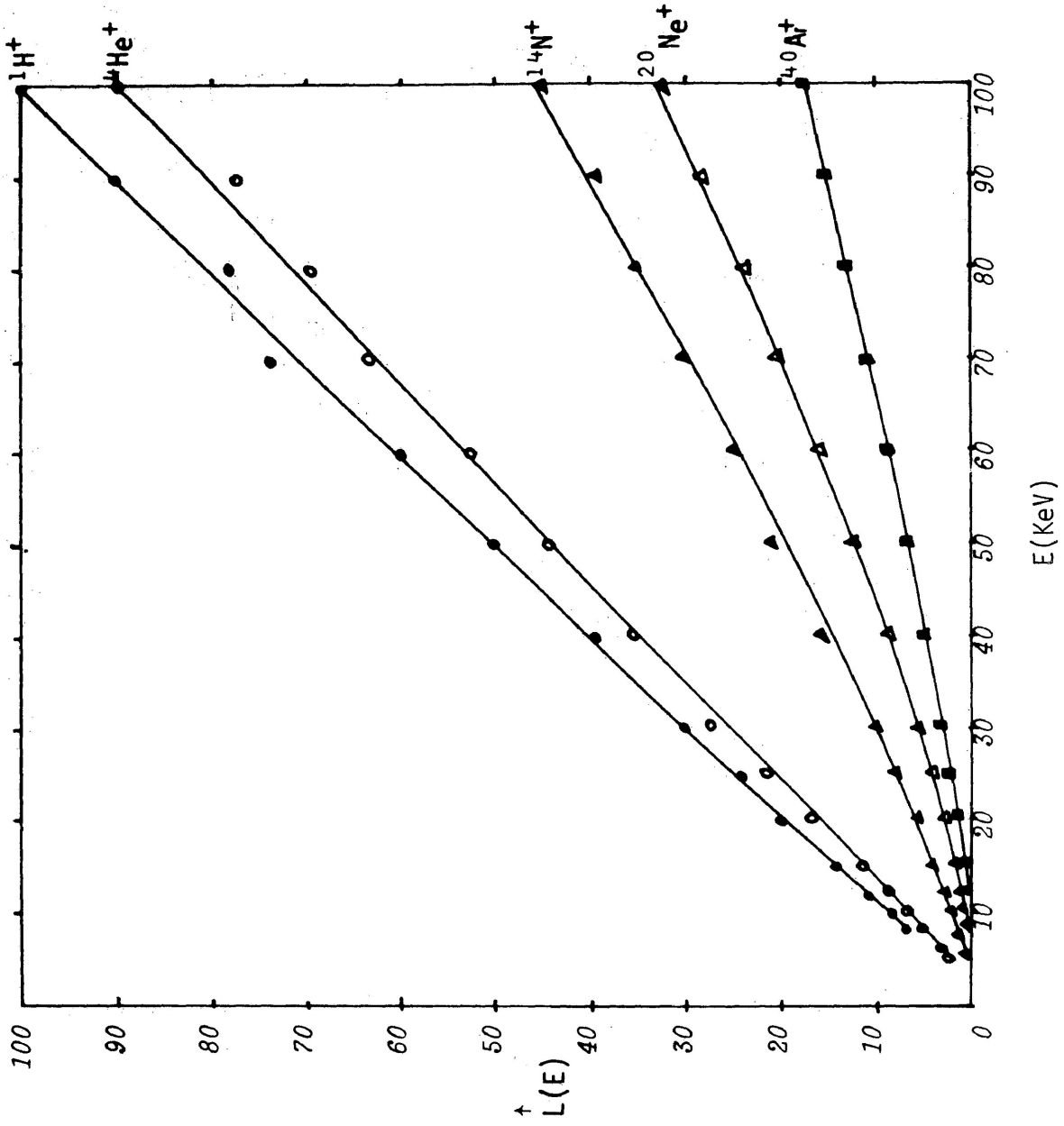

Fig. 21. A linear plot of L *versus* E for $^{1}H^{+}$, $^{4}He^{+}$, $^{14}N^{+}$, $^{20}Ne^{+}$ and $^{40}Ar^{+}$ ions impinging on CsI(Na).

The light output from the organic scintillator stilbene was found to be approximately five times larger than the light output from Plastifluor. The L *versus* E plot of stilbene shown in Fig. 18 is similar to the plot for Plastifluor shown in Fig. 15. For $^{12}C^{+}$ ions, a linear relation between light output and energy was again obtained. For $^{1}H^{+}$, L is a linear function of E for $E > 25$ KeV, but for $E < 20$ it is nonlinear with a curvature corresponding to a higher value of dL/dE at low E. Although Plastifluor and stilbene are of somewhat similar atomic constitution, stilbene is a crystal whereas Plastifluor is a solution. This fact may cause the greater relative separation between the light output of the light and heavy ions in stilbene as compared to Plastifluor.

Fig. 19 shows the results of measurements of a NaI(Tℓ) scintillator where the surface has been polished with extra fine emery paper. The L *versus* E relationship for each of the ions investigated is nonlinear, all have curvatures concave toward the energy axis. The difference in light output between light and heavy ions is considerably larger than in the other types of scintillation crystal. The large deviation from linearity of the L *versus* E plot for $^{1}H^{+}$ and the low luminescent response for heavy ions may be due to the fact that NaI is very hygroscopic, a large amount of excitation energy has been lost due to processes occurring at the surface. This will be interpreted by considering surface recombination.

Results of measurements performed using CsI(Tℓ) and CsI(Na) are shown in Fig. 20 and Fig. 21; both crystals have been polished with paper and lens tissue to eliminate any contamination which might be present after removal from the shipping container. It was observed in both CsI(Tℓ) and CsI(Na) crystals that the relative light output L has a linear relation

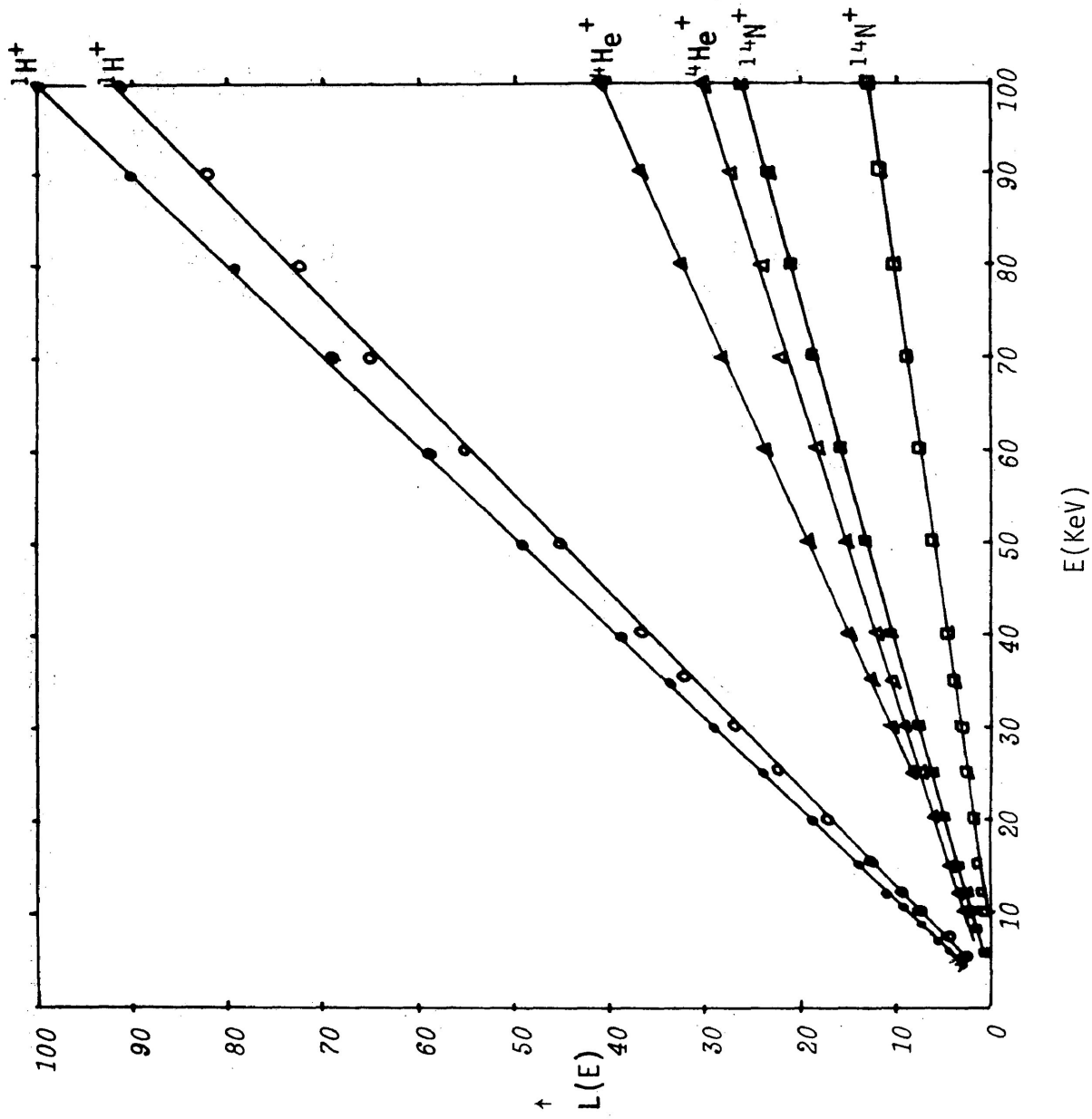

Fig. 22. A composite plot of L *versus* E for $^1H^+$, $^4He^+$ and $^{14}N^+$ ions impinging on CsI(Tℓ) [$^1H^+$(●); $^4He^+$(▲); $^{14}N^+$(■)] and CsI(Na) [$^1H^+$(o); $^4He^+$(Δ); $^{14}N^+$(□)].

with ion energy E for $^{1}H^{+}$ and $^{4}He^{+}$ ions over the entire energy range studied within experimental error. For $^{14}N^{+}$, $^{20}Ne^{+}$ and $^{40}Ar^{+}$, L *versus* E is linear in the energy range 20 — 100 KeV for CsI(Tℓ); for CsI(Na), the linear relation was found in the energy range 30 — 100 KeV. A comparison for the luminescent response from CsI(Tℓ) and CsI(Na), as displayed in Fig. 22, shows a number of differences. (In order to avoid confusion, the $^{20}Ne^{+}$ and $^{40}Ar^{+}$ curves are not shown in Fig. 22.) It was found that the light output of CsI(Tℓ) is approximately 3.3 times higher than that of CsI(Na) for a given mass and ion energy. That is, the ratio of luminescent efficiency from CsI(Tℓ) to that from CsI(Na) is approximately 1:0.3. The difference in luminescent efficiency between CsI(Tℓ) and CsI(Na) may be due to the presence of different impurities (Tℓ, Na) in the crystal, but is more likely due to different impurity concentrations. That this is true is strongly indicated by the close agreement of the normalized curves for the two samples (Figs. 20 and 21). This observation is an indication that the L *versus* E relation is governed by the ion-lattice energy transfer processes. That is, the transfer of ion energy to the lattice is more important than the transfer to the impurities themselves and the luminescent efficiency is determined by the impurity characteristics or concentrations.

The solid curves in Figs. 23 to 26 represent theoretically predicted values of L as a function of energy, calculated from Eqn. (1). The constant C in the equation was adjusted so as to normalize the curve to one experimental point of one chosen impinging ion; the remaining points then followed. The normalized value of C was then used in calculating the theoretical L values as a function of ion energy for the rest of the impinging ions. The broken lines were drawn through the experimental points.

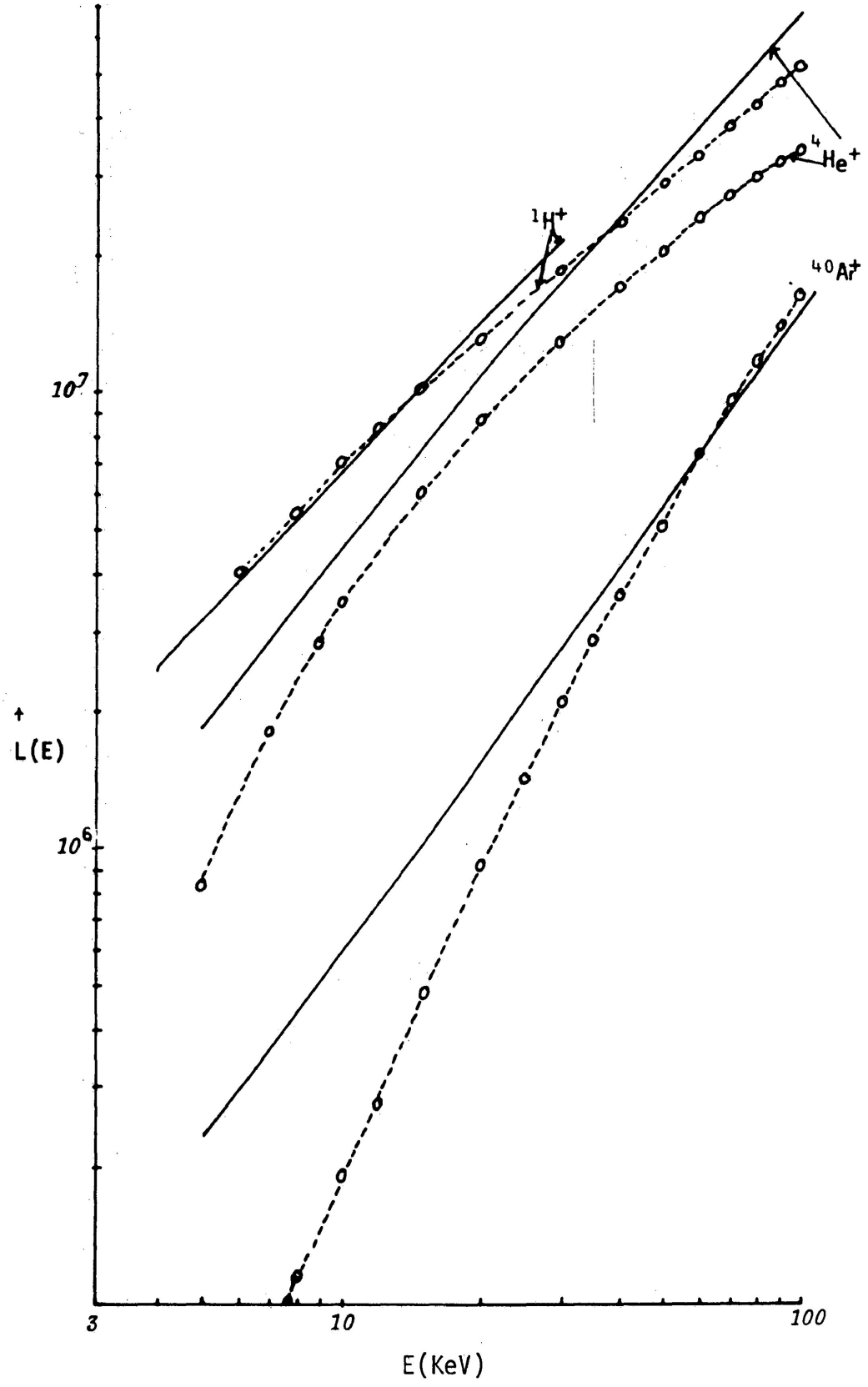

Fig. 23. A logarithmic plot of L *versus* E for $^1H^+$, $^4He^+$ and $^{40}Ar^+$ ions impinging on Plastifluor. The solid curves represent the appropriate theoretical function [Eqn. (1)] and the broken lines are drawn through the experimental points.

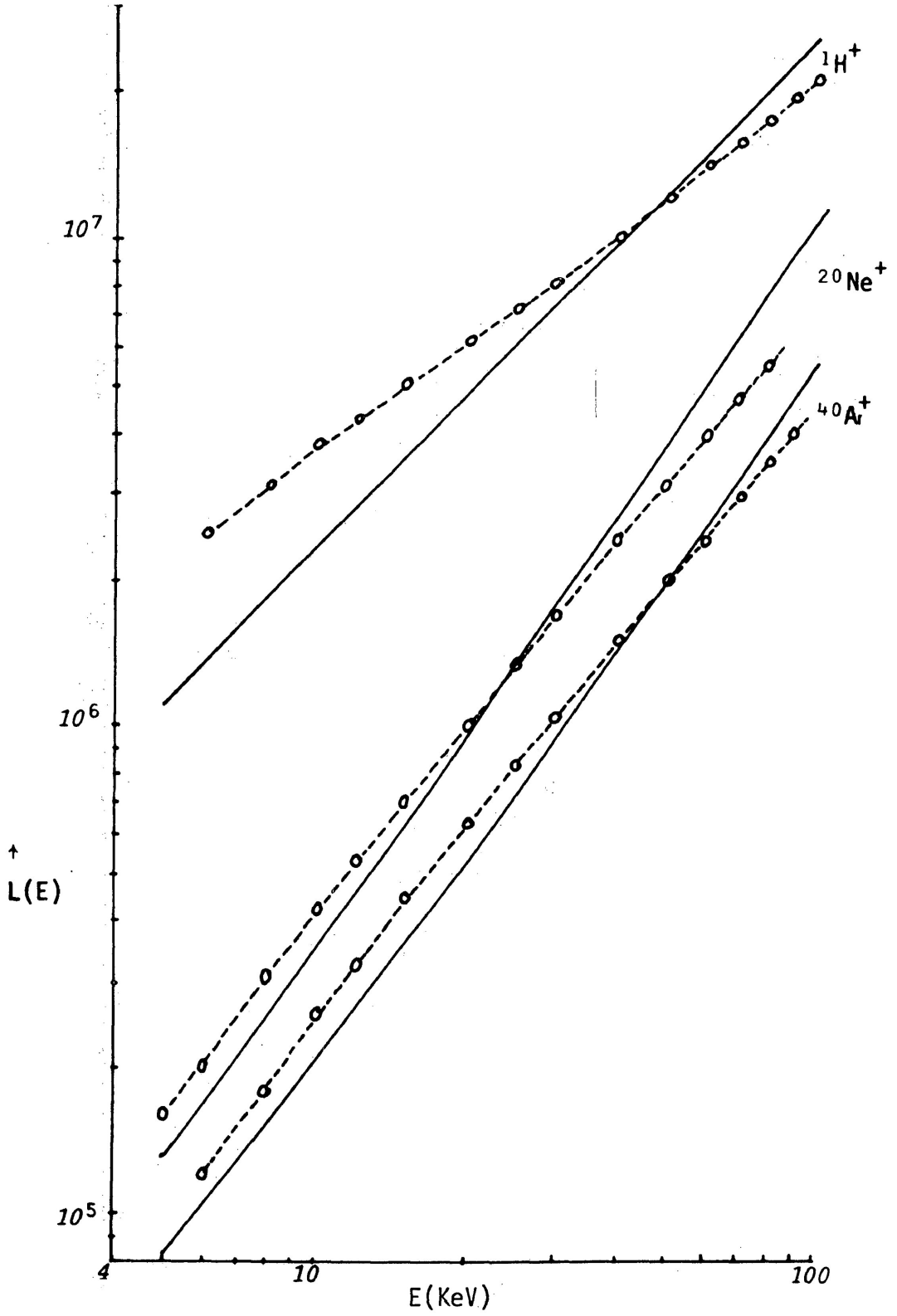

Fig. 24. A logarithmic plot of L *versus* E for $^1H^+$, $^{20}Ne^+$ and $^{40}Ar^+$ ions impinging on stilbene. The solid curves represent the appropriate theoretical function [Eqn. (1)] and the broken lines are drawn through the experimental points.

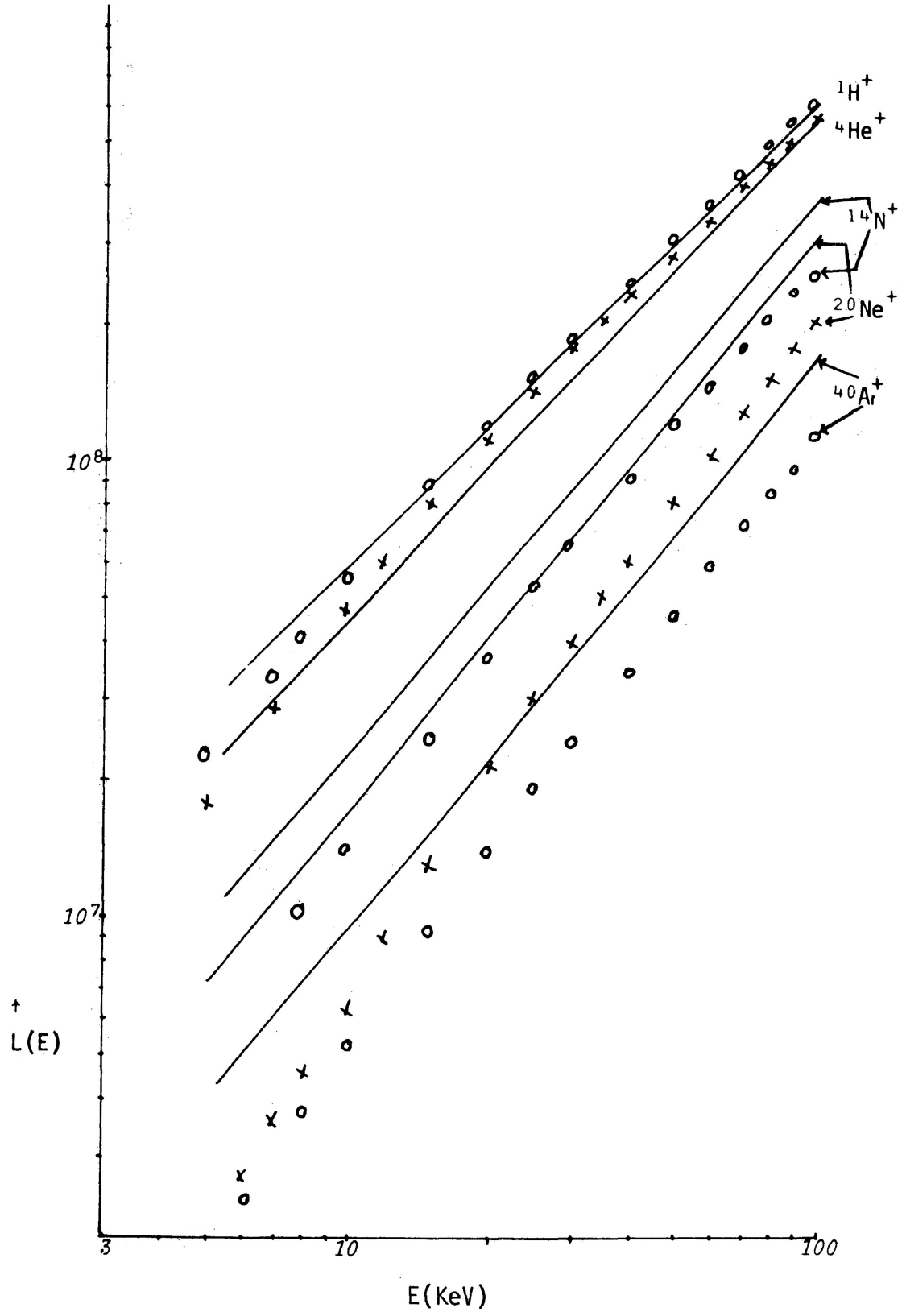

Fig. 25. A logarithmic plot of L *versus* E for $^{1}H^{+}$, $^{4}He^{+}$, $^{14}N^{+}$, $^{20}Ne^{+}$ and $^{40}Ar^{+}$ ions impinging on CsI(Tℓ). The solid curves represent the appropriate theoretical function [Eqn. (1)].

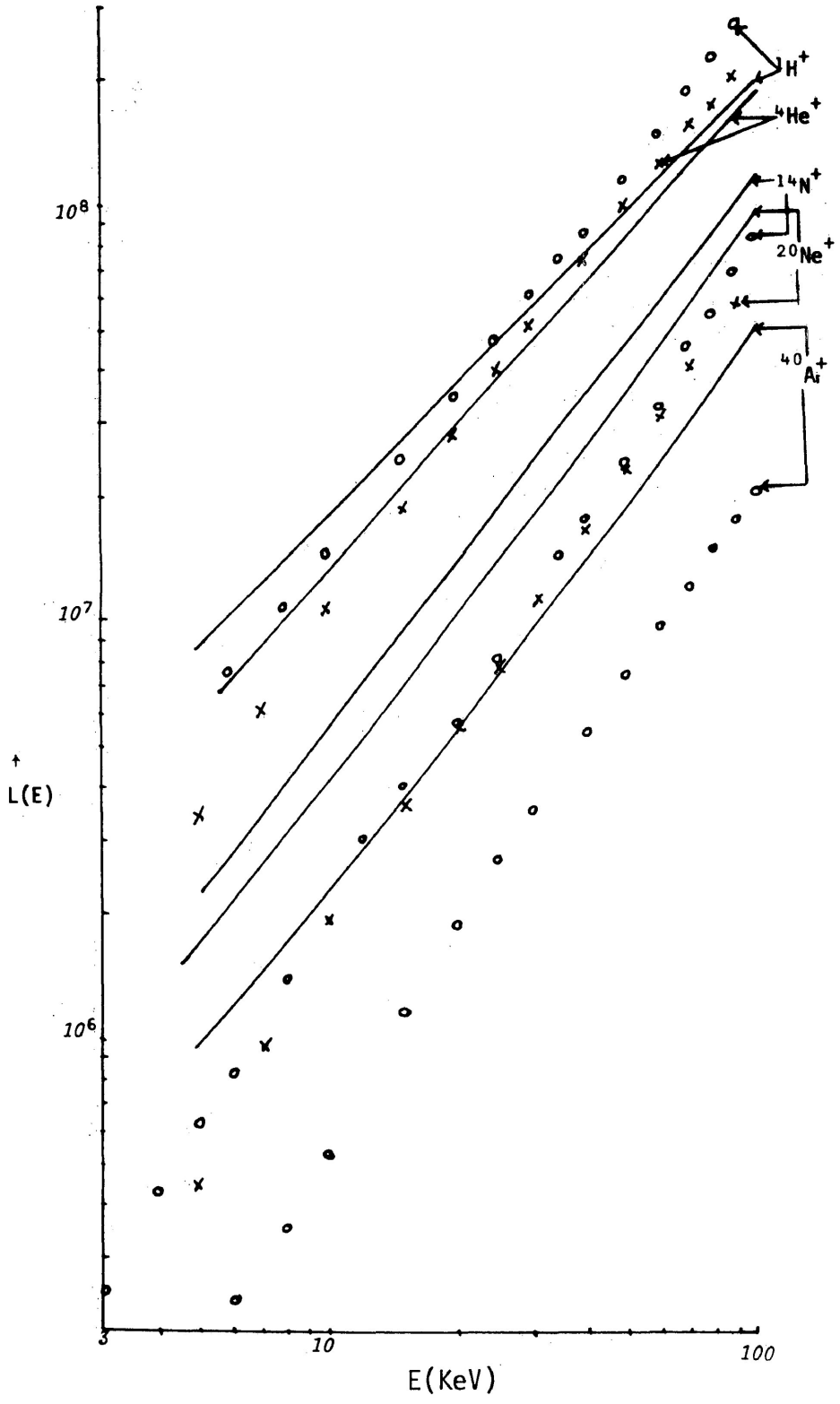

Fig. 26. A logarithmic plot of L *versus* E for $^1H^+$, $^4He^+$, $^{14}N^+$, $^{20}Ne^+$ and $^{40}Ar^+$ ions impinging on NaI(Tl). The solid curves represent the appropriate theoretical function [Eqn. (1)].

Fig. 23 shows the results obtained from a Plastifluor sample with three singly charged positive ions $^{1}H^{+}$, $^{4}He^{+}$ and $^{40}Ar^{+}$ as impinging particles. It is not surprising that the theory does not predict the functional relationship of L and E, as well as the relative magnitude of light output and the spacing of ions of different masses, since the energy transfer mechanism of the Plastifluor solid solution is known to be different from the mechanism found in crystals.

The results of the stilbene scintillator are shown in Fig. 24. For heavier ions, the predicted L *versus* E curves have a slope about 15 percent steeper than the experimental ones. Moreover, the difference between observation and theory is larger for $^{1}H^{+}$ than for the other ions.

The experimental points in Fig. 25 show the observed light output as a function of energy for $^{1}H^{+}$, $^{14}N^{+}$, $^{40}Ar^{+}$, $^{4}He^{+}$ and $^{20}Ne^{+}$ incident upon CsI(Tℓ). The value of C was adjusted so that the theoretical and experimental curves have approximately the correct slope, but do not predict the correct relative magnitudes for the light produced by the heavier ions.

Fig. 26 is a similar plot for NaI(Tℓ). It will be noted that the theoretical curves do not agree with the experimental ones as well as they did for CsI(Tℓ). The experimental curves have a higher slope and seem to diverge more and more from the theoretical ones as the ion mass is increased and the energy reduced. This effect is thought to be due to surface recombination whose role is most important for heavy, short-ranged ions and ions of low energy which do not penetrate the sample to depths far from the surface.

Since NaI is hygroscopic, the surface is readily contaminated by moisture in the air during sample handling. It is thus reasonable to

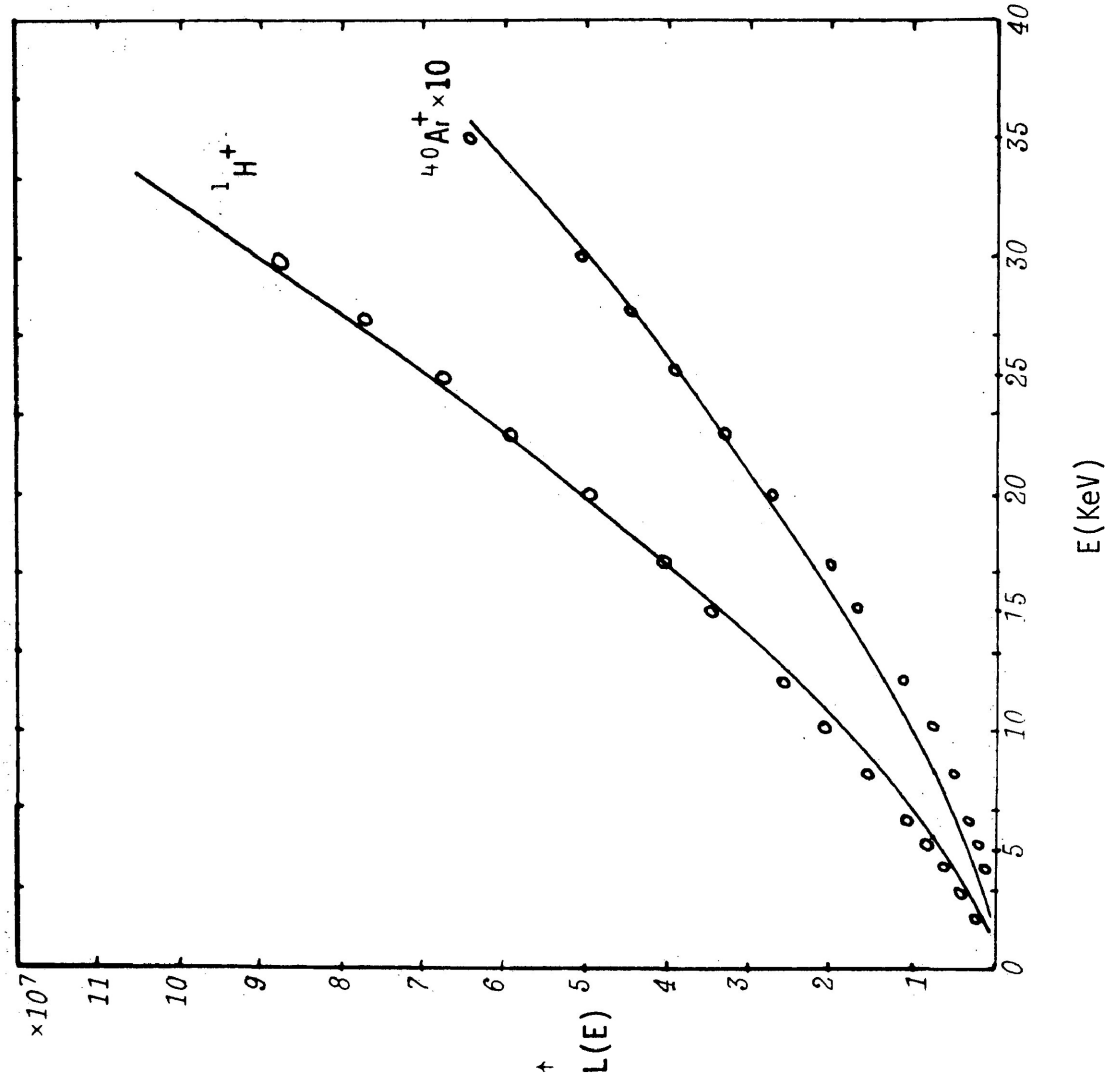

Fig. 27. A linear plot of L *versus* E for $^{1}H^{+}$ and $^{40}Ar^{+}$ ions impinging on NaI(Tl) at lower energies. The solid curves represent the appropriate theoretical functions [Eqn. (9) and Eqn. (14)].

expect surface recombination effects to be present in this substance. CsI, however, is much better in this regard and serious surface damage during preparation is not expected. Since the experimental curves for CsI (see Fig. 25) do not show a strong low-energy divergence from the theoretical ones, it is assumed that no serious surface effects are present.

Theoretical curves for NaI(Tℓ) with the surface recombination effect are shown in Fig. 27. The points are experimental, the curve for $^{1}H^{+}$ was computed using Eqn. (9) and for $^{40}Ar^{+}$ was computed using Eqn. (16) with a surface loss parameter Q = 0.9 and diffusion length of 3000 Å. The proportionality constant k' was obtained by normalizing the theoretical L values of $^{1}H^{+}$ to the corresponding experimental value at 20 KeV. The general agreement between theory and experiments seems fairly good.

The depth of penetration (projected range) R_p for both $^{1}H^{+}$ and $^{40}Ar^{+}$ in NaI were obtained using the ratio R_p / R predicted by Lindhard *et al.*[12] and by Schiott[56] where R, the total path length, is calculated according to

$$R = \int_0^{E_0} \frac{1}{NS}\, dE$$

where

$$S = S_e + S_n.$$

Fig. 28 is a composite plot of the theoretical curves for CsI and NaI *versus* energy computed from Eqn. (1) and normalized so that the $^{1}H^{+}$ curves were coincident. It will be noted that on the basis of this theoretical model, little difference is expected between the light outputs for these substances, although as was pointed out, the theory does not agree particularly well with experiment for either substance. The

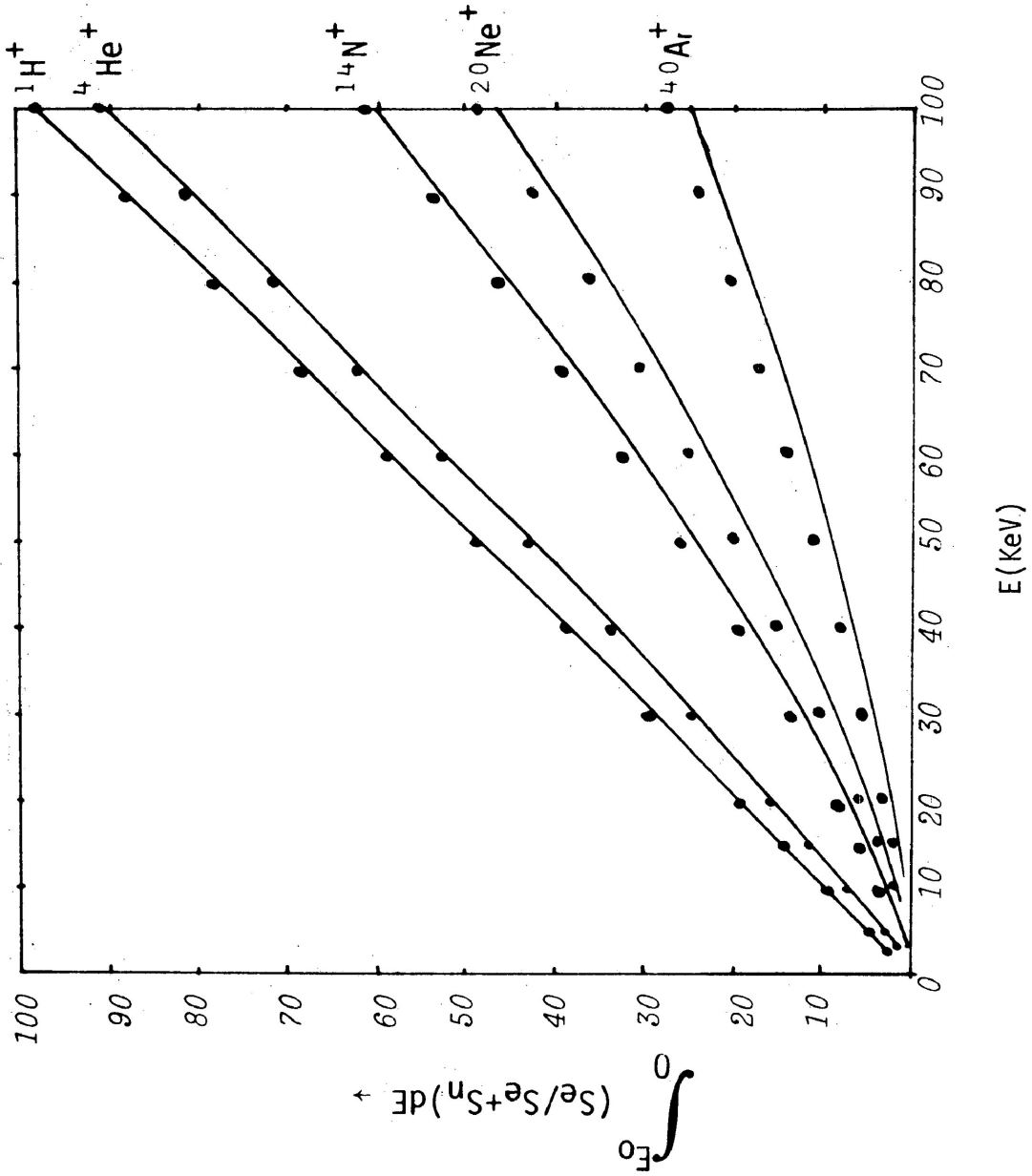

Fig. 28. A composite plot of theoretical $\int_0^{E_0} \frac{S_e}{S_e + S_n} dE$ values *versus* E for $^{1}H^{+}$, $^{4}He^{+}$, $^{14}N^{+}$, $^{20}Ne^{+}$ and $^{40}Ar^{+}$ ions in CsI(Tℓ) [·] and NaI(Tℓ) [solid curve].

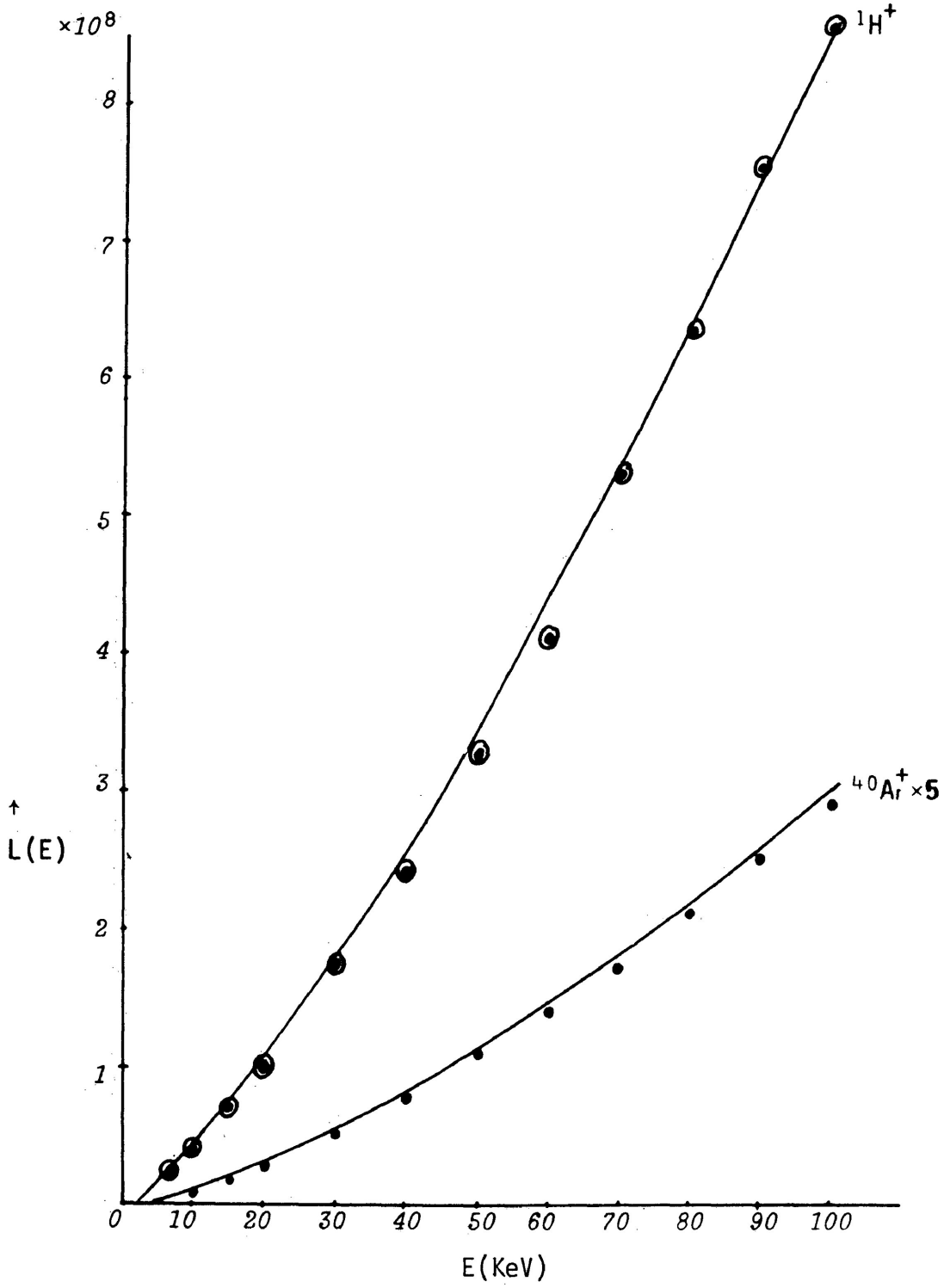

Fig. 29. The dotted circles ⊙ and dots · are experimental L values of NaI(Tℓ) for $^{1}H^{+}$ and $^{40}Ar^{+}$, respectively. The solid curves were obtained by using the experimental L values of CsI(Tℓ) multiplied by Eqn. (15) and a constant.

divergence of the theoretical CsI curves from experiment may well be due to the fact that S_e is incorrectly estimated and that observed Z_1 oscillations must be taken into account for a better fit. In order to compute the effect of surface recombination, the following assumptions were made:

(1) The bulk luminescent response of CsI and NaI has the same relative dependence on ion mass and energy. This is consistent with the initial theory.

(2) In NaI, surface recombination plays a strong role; in CsI, it does not.

Thus one may consider that the L values of NaI may be obtained from the corresponding L values of CsI by

$$L_{exp}(NaI) = C \times f(R_p / L_D) \times L_{exp}(CsI).$$

The results of such an estimation are shown in Fig. 29 with $f(R_p/L_D)$ given in Eqn. (15). The dotted circles and dots are experimental L values for $^1H^+$ and $^{40}Ar^+$ in NaI(Tl), respectively, and the solid curves were obtained according to the above relation. It will be noted that this treatment also yields an excellent overall fit.

Powdered Phosphors

The luminescent responses of powdered phosphors under $^1H^+$, $^4He^+$, $^{14}N^+$, $^{20}Ne^+$ and $^{40}Ar^+$ bombardment are shown in Figs. 30 to 54. In reviewing the experimental results describing the luminescent response, several general features are observed in the various phosphors:

(1) The relative light output L increased with increasing ion energy and decreased rapidly with increasing ion mass.

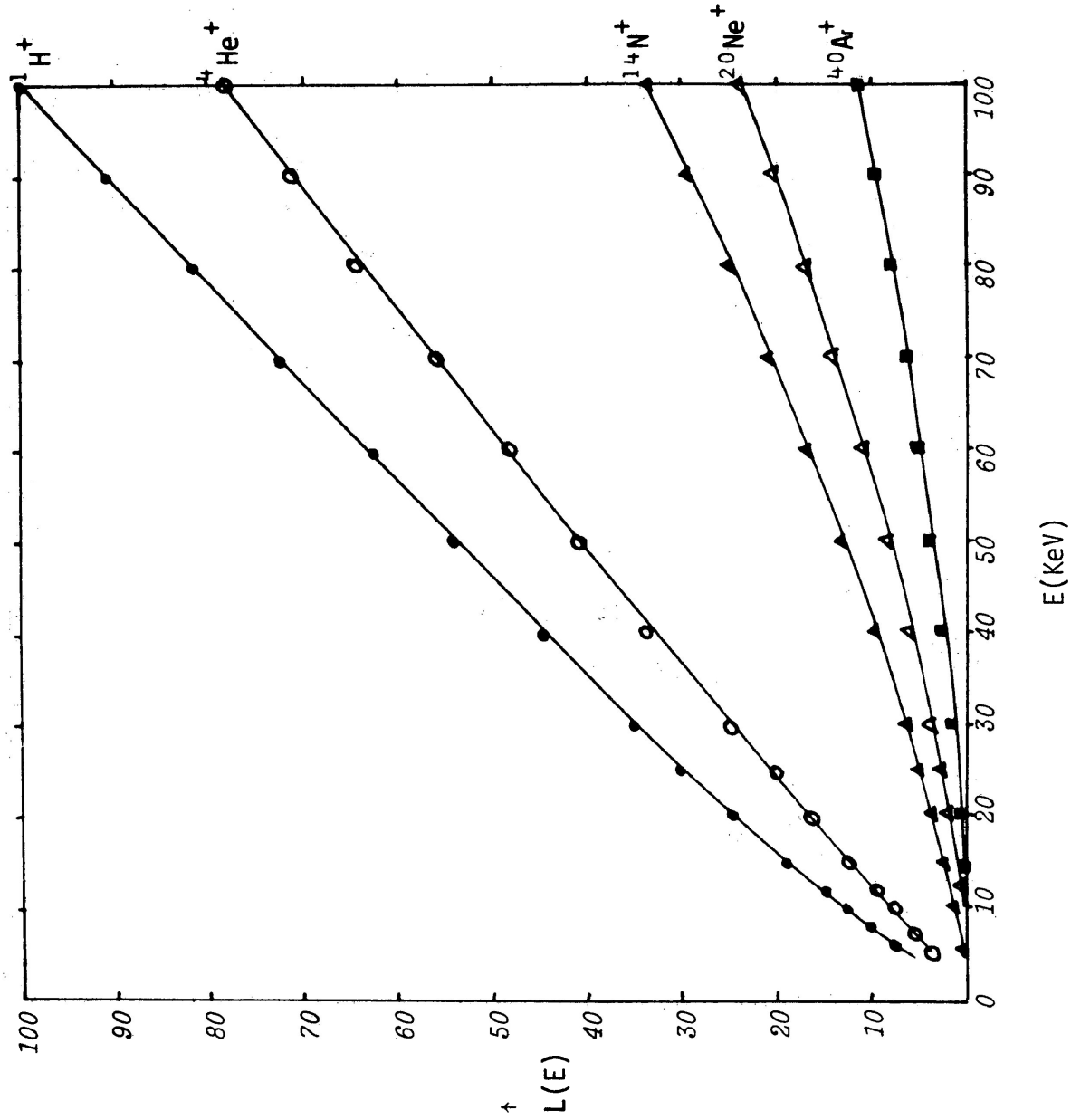

Fig. 30. A linear plot of L *versus* E for $^{1}H^{+}$, $^{4}He^{+}$, $^{14}N^{+}$, $^{20}Ne^{+}$ and $^{40}Ar^{+}$ ions impinging on Zn_2SiO_4:Mn (P-1, 2μ size).

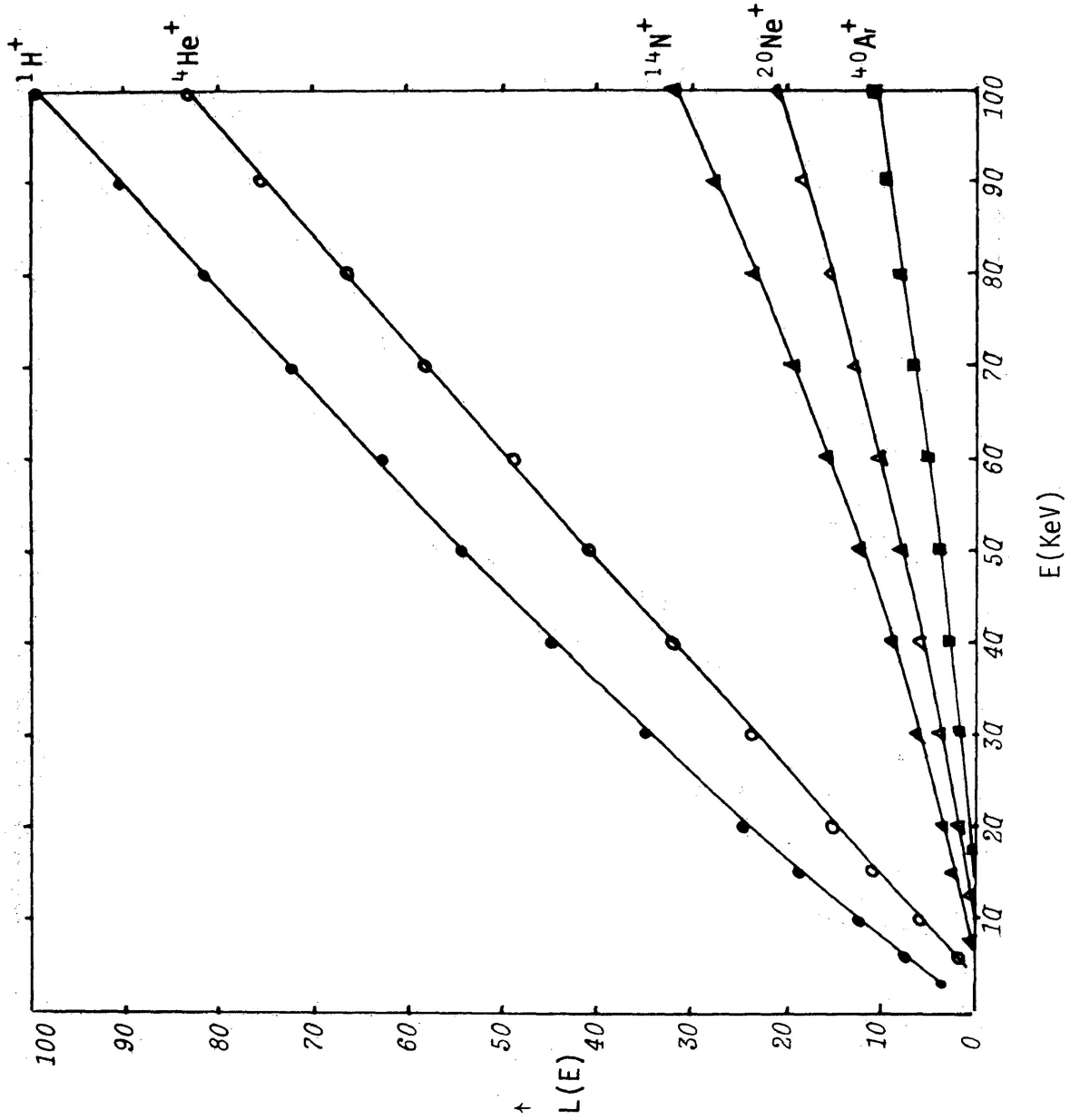

Fig. 31. A linear plot of L *versus* E for $^{1}H^{+}$, $^{4}He^{+}$, $^{14}N^{+}$, $^{20}Ne^{+}$ and $^{40}Ar^{+}$ ions impinging on Zn_2SiO_4:Mn (P-1, 5μ size).

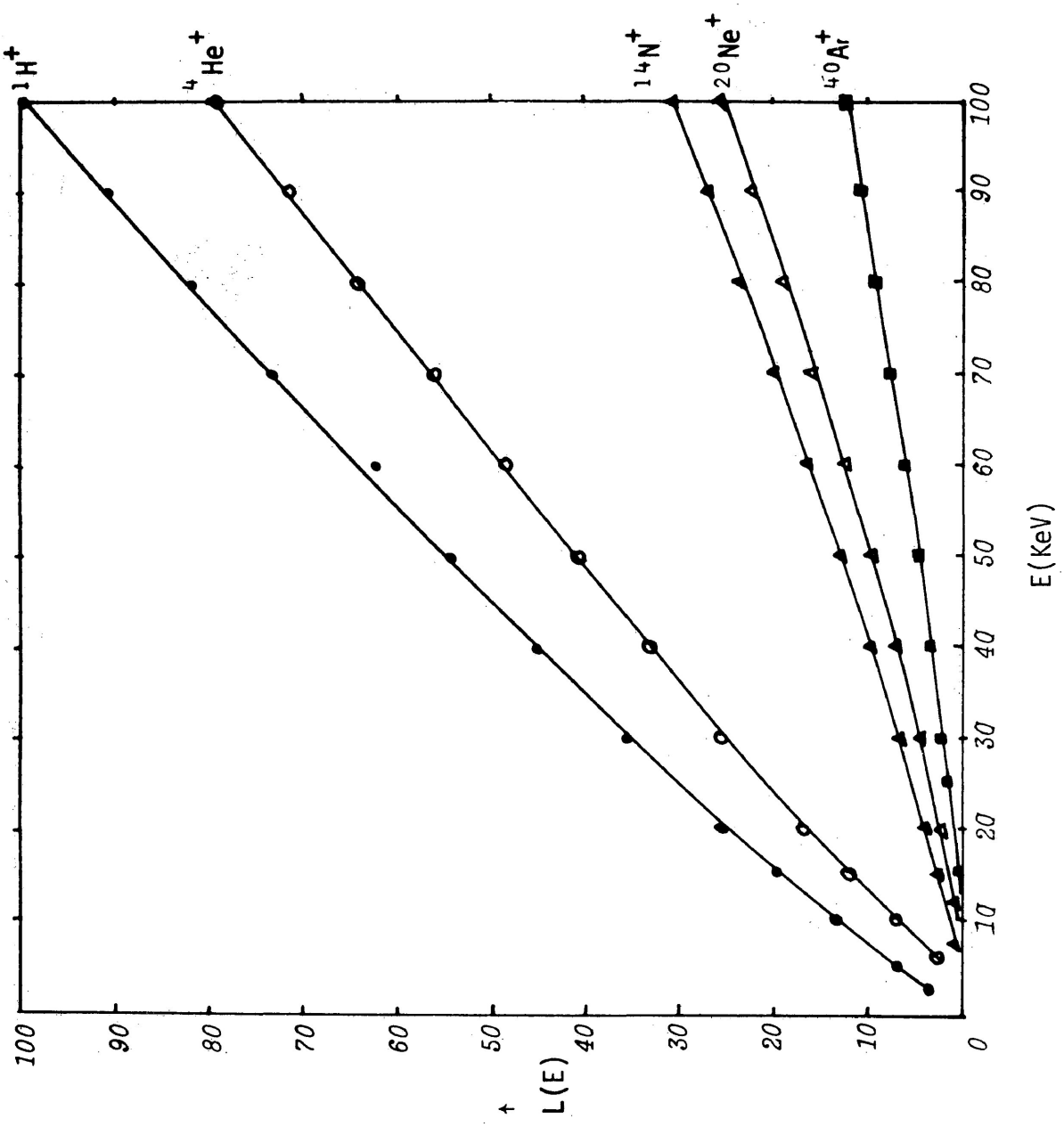

Fig. 32. A linear plot of L *versus* E for $^{1}H^{+}$, $^{4}He^{+}$, $^{14}N^{+}$, $^{20}Ne^{+}$ and $^{40}Ar^{+}$ ions impinging on Zn_2SiO_4:Mn (P-1, 10μ size).

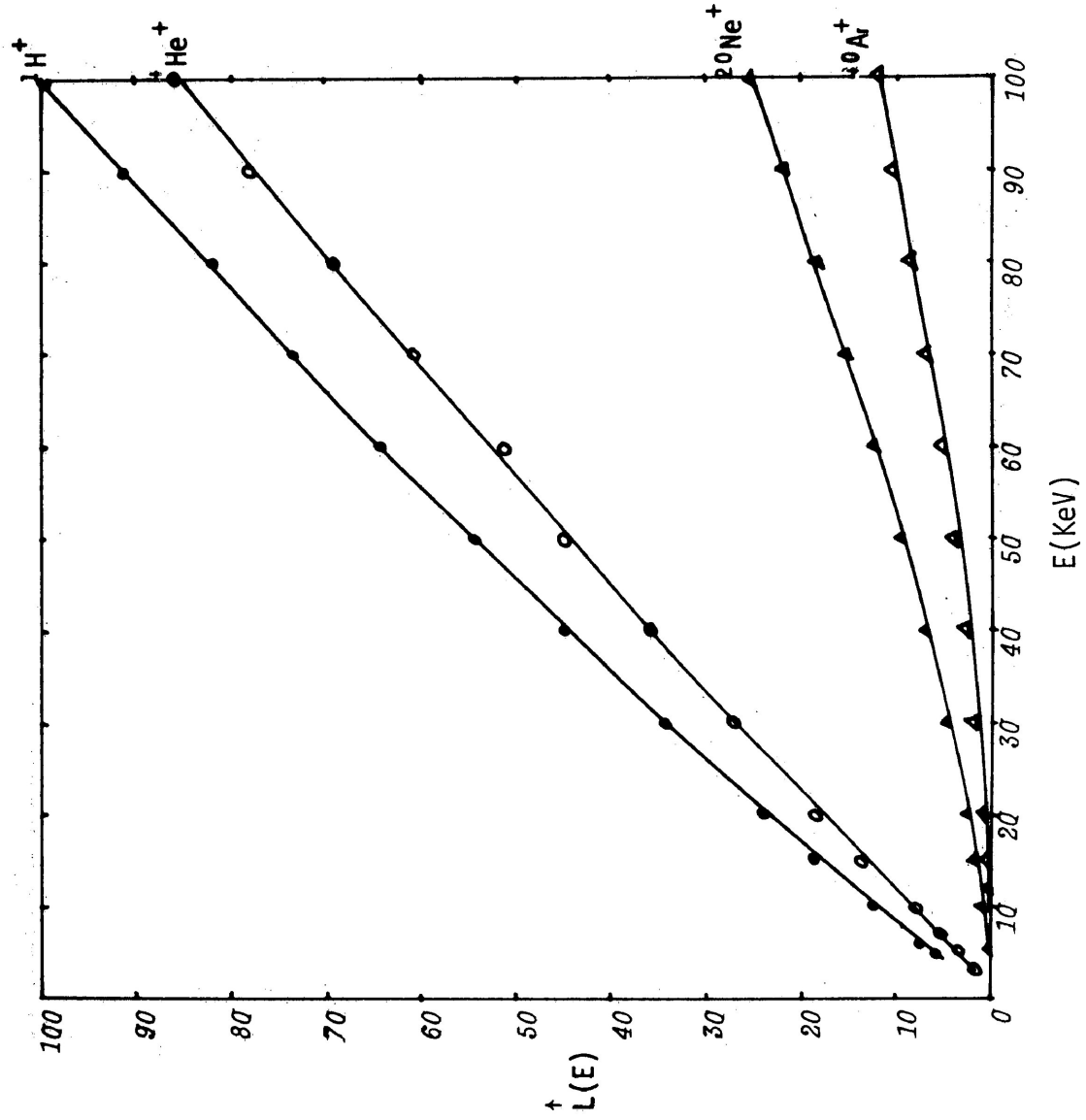

Fig. 33. A linear plot of L *versus* E for $^{1}H^{+}$, $^{4}He^{+}$, $^{20}Ne^{+}$ and $^{40}Ar^{+}$ ions impinging on Zn_2SiO_4:Mn (P-1 regular).

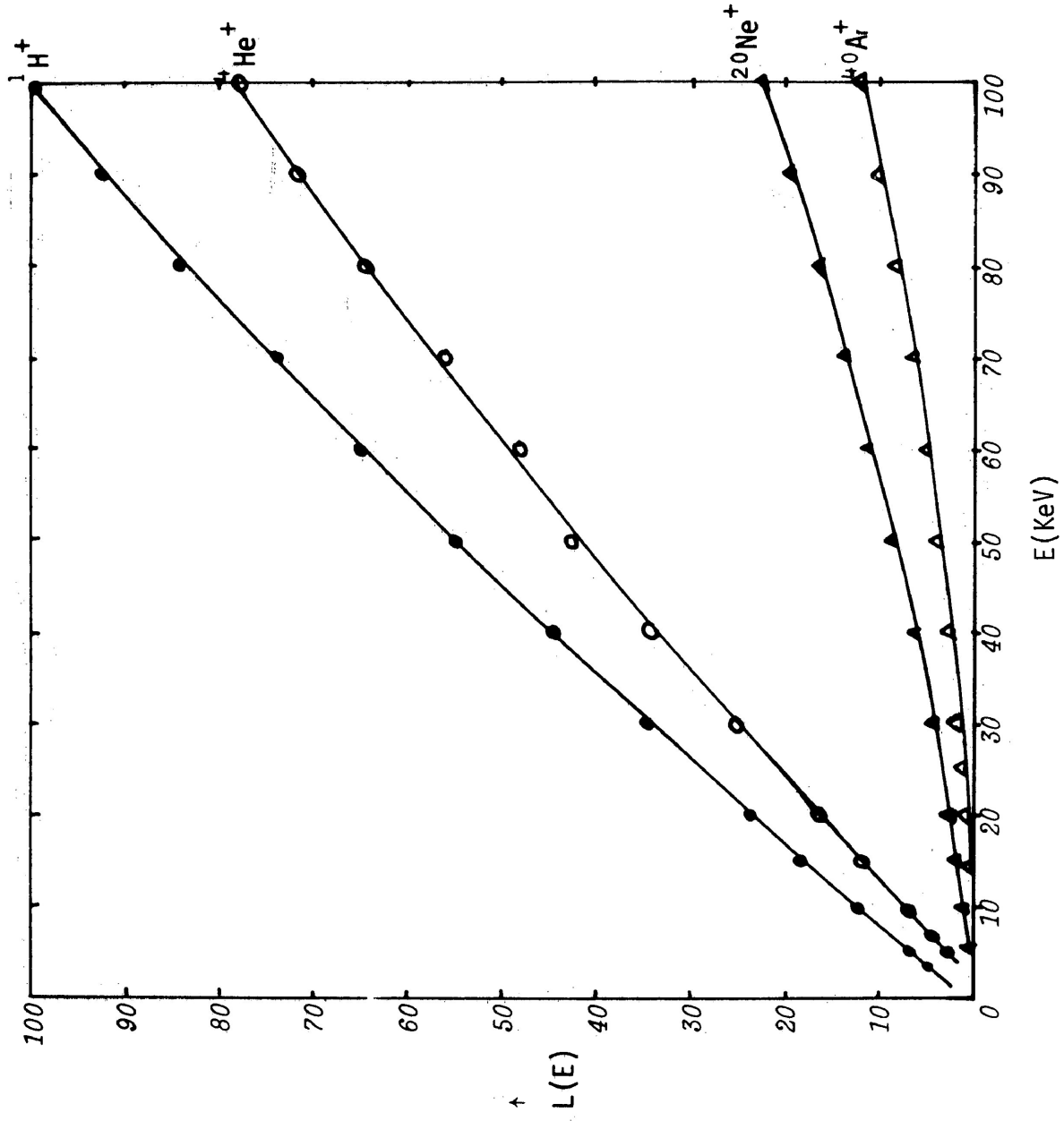

Fig. 34. A linear plot of L *versus* E for $^{1}H^{+}$, $^{4}He^{+}$, $^{20}Ne^{+}$ and $^{40}Ar^{+}$ ions impinging on Zn_2SiO_4:Mn (P-1 fine).

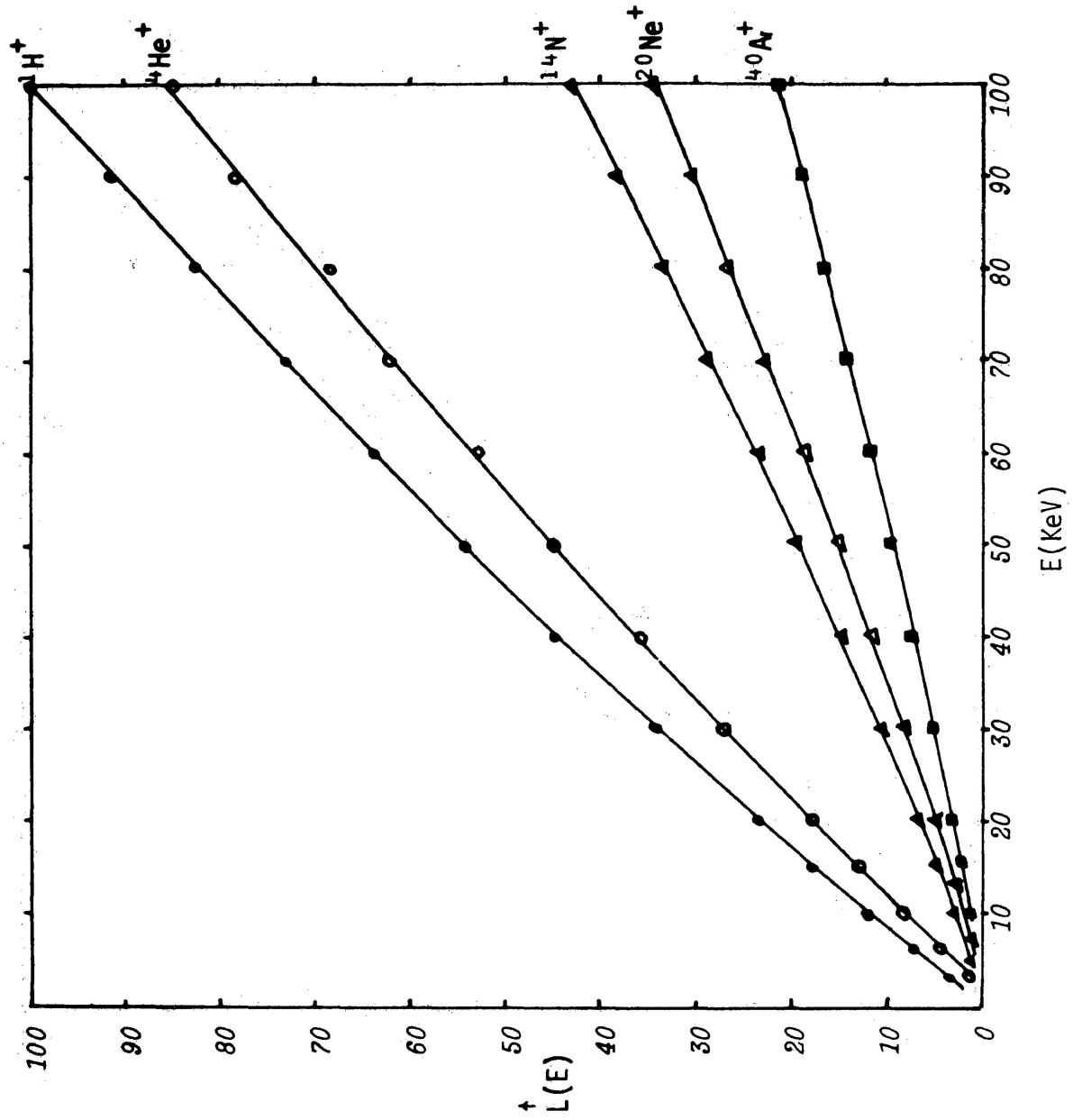

Fig. 35. A linear plot of L *versus* E for $^{1}H^{+}$, $^{4}He^{+}$, $^{14}N^{+}$, $^{20}Ne^{+}$ and $^{40}Ar^{+}$ ions impinging on ZnO:Zn.

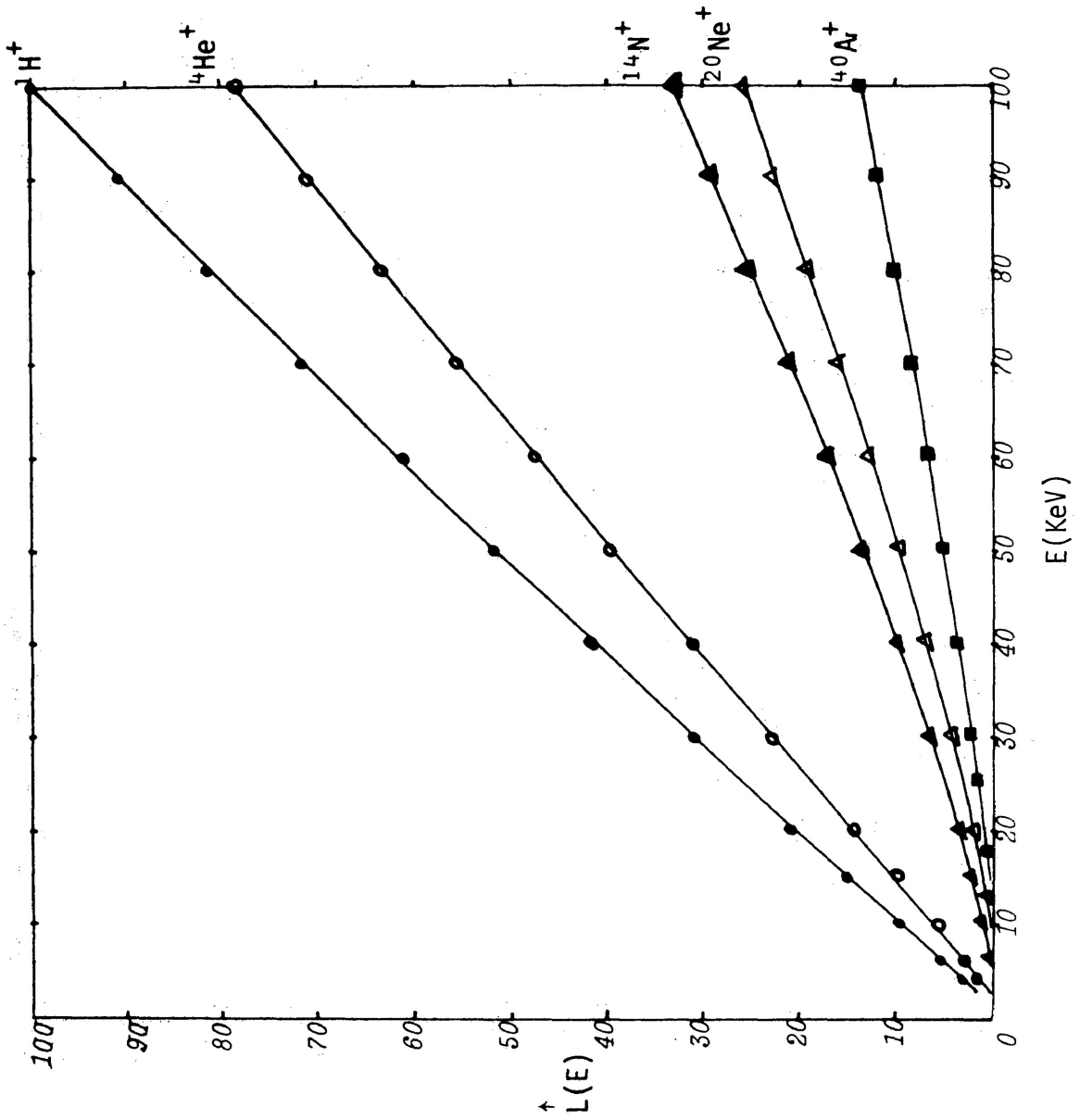

Fig. 36. A linear plot of L *versus* E for $^{1}H^{+}$, $^{4}He^{+}$, $^{14}N^{+}$, $^{20}Ne^{+}$ and $^{40}Ar^{+}$ ions impinging on Y_2O_2S:Eu.

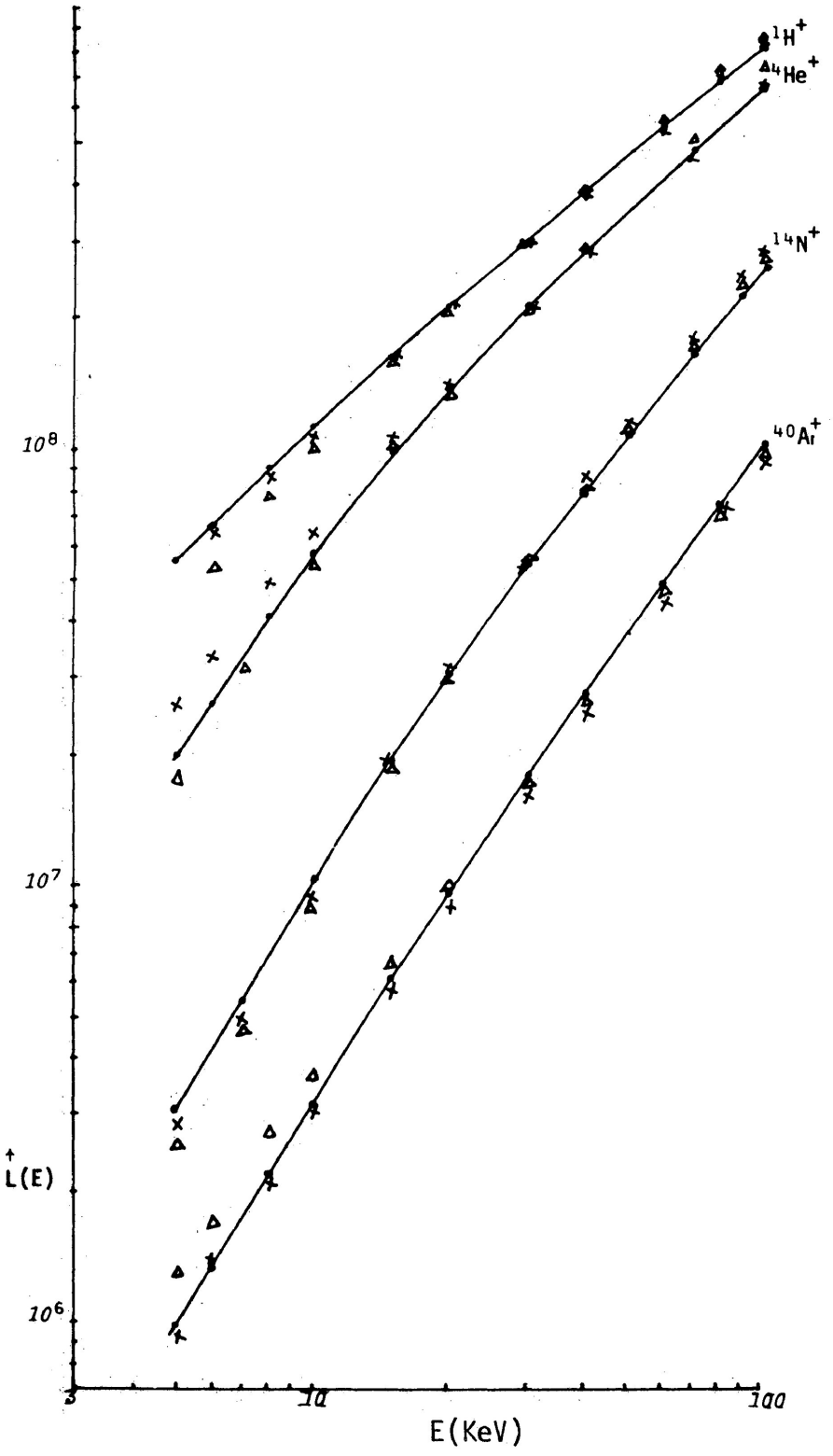

Fig. 37. A composite plot of L *versus* E for $^1H^+$, $^4He^+$, $^{14}N^+$ and $^{40}Ar^+$ ions impinging on Zn_2SiO_4:Mn of different particle size: 10μ (·); 5μ(x); and 2μ(Δ). Solid curves are drawn through the points of 10μ size sample.

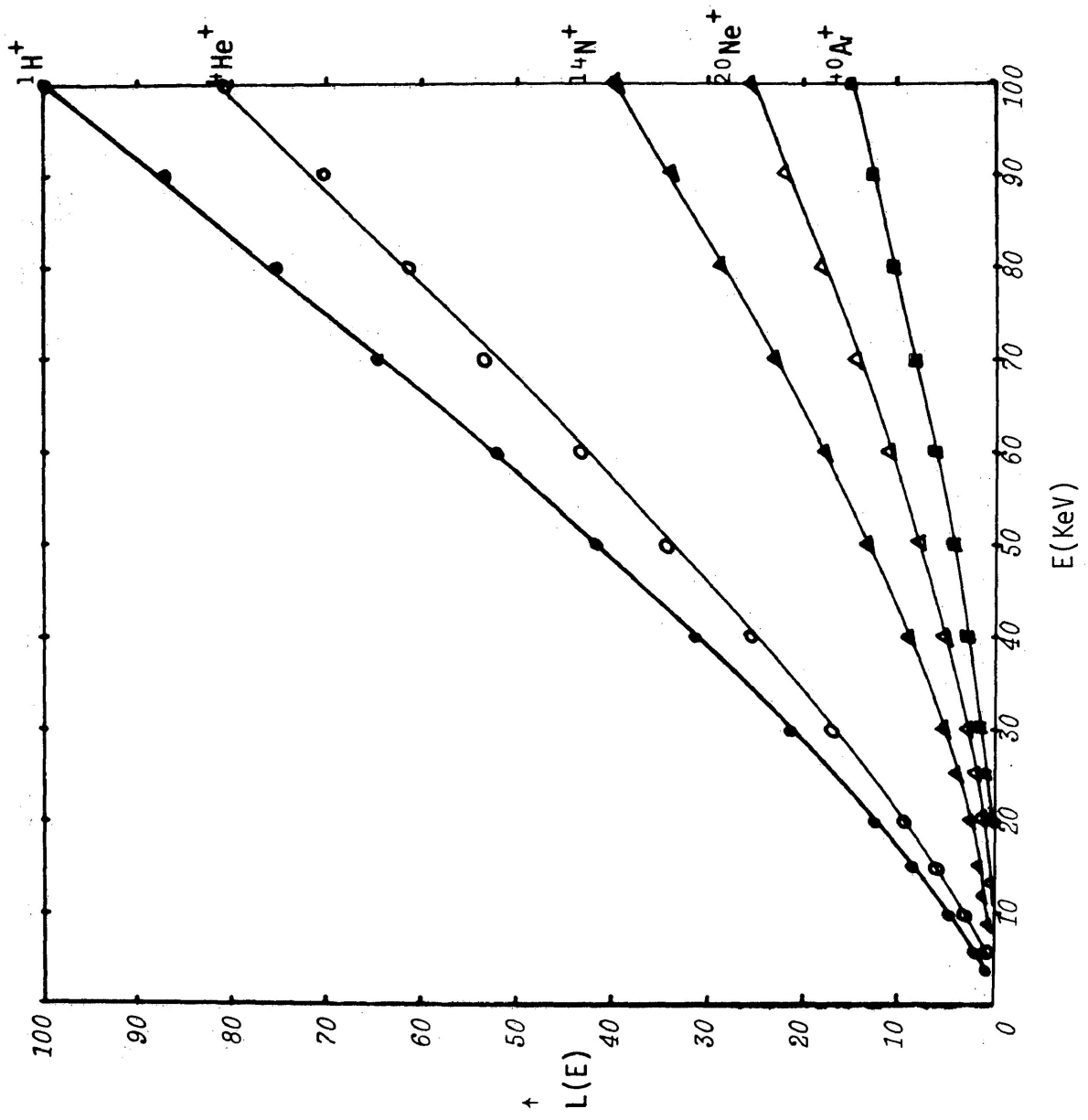

Fig. 38. A linear plot of L *versus* E for $^{1}H^{+}$, $^{4}He^{+}$, $^{14}N^{+}$, $^{20}Ne^{+}$ and $^{40}Ar^{+}$ ions impinging on ZnS:Ag (P-22, 7μ size).

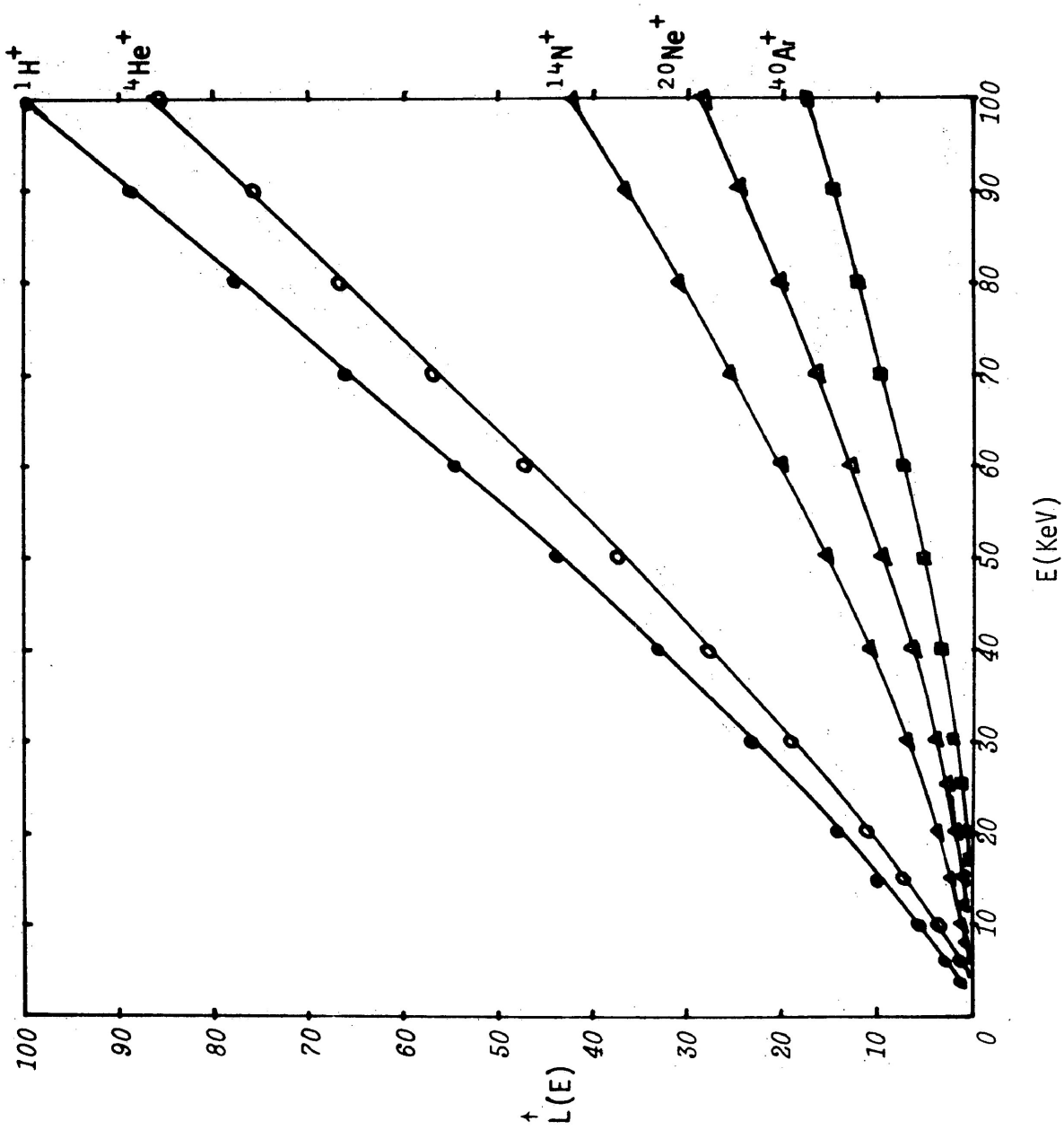

Fig. 39. A linear plot of L *versus* E for $^{1}H^{+}$, $^{4}He^{+}$, $^{14}N^{+}$, $^{20}Ne^{+}$ and $^{40}Ar^{+}$ ions impinging on ZnS:Ag (P-11, 10.5μ size).

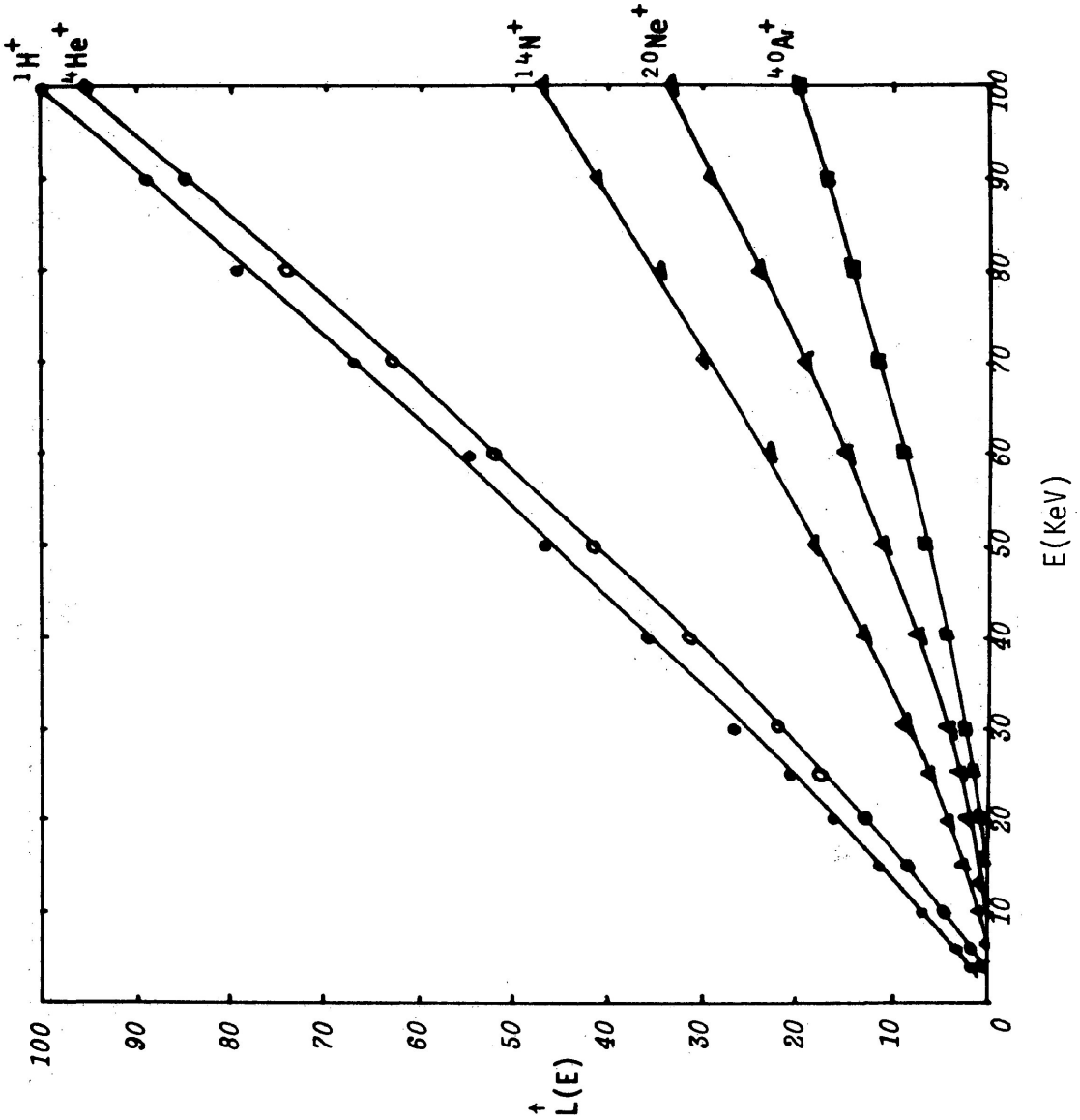

Fig. 40. A linear plot of L *versus* E for $^{1}H^{+}$, $^{4}He^{+}$, $^{14}N^{+}$, $^{20}Ne^{+}$ and $^{40}Ar^{+}$ ions impinging on ZnS:Ag (P-11, 4μ size).

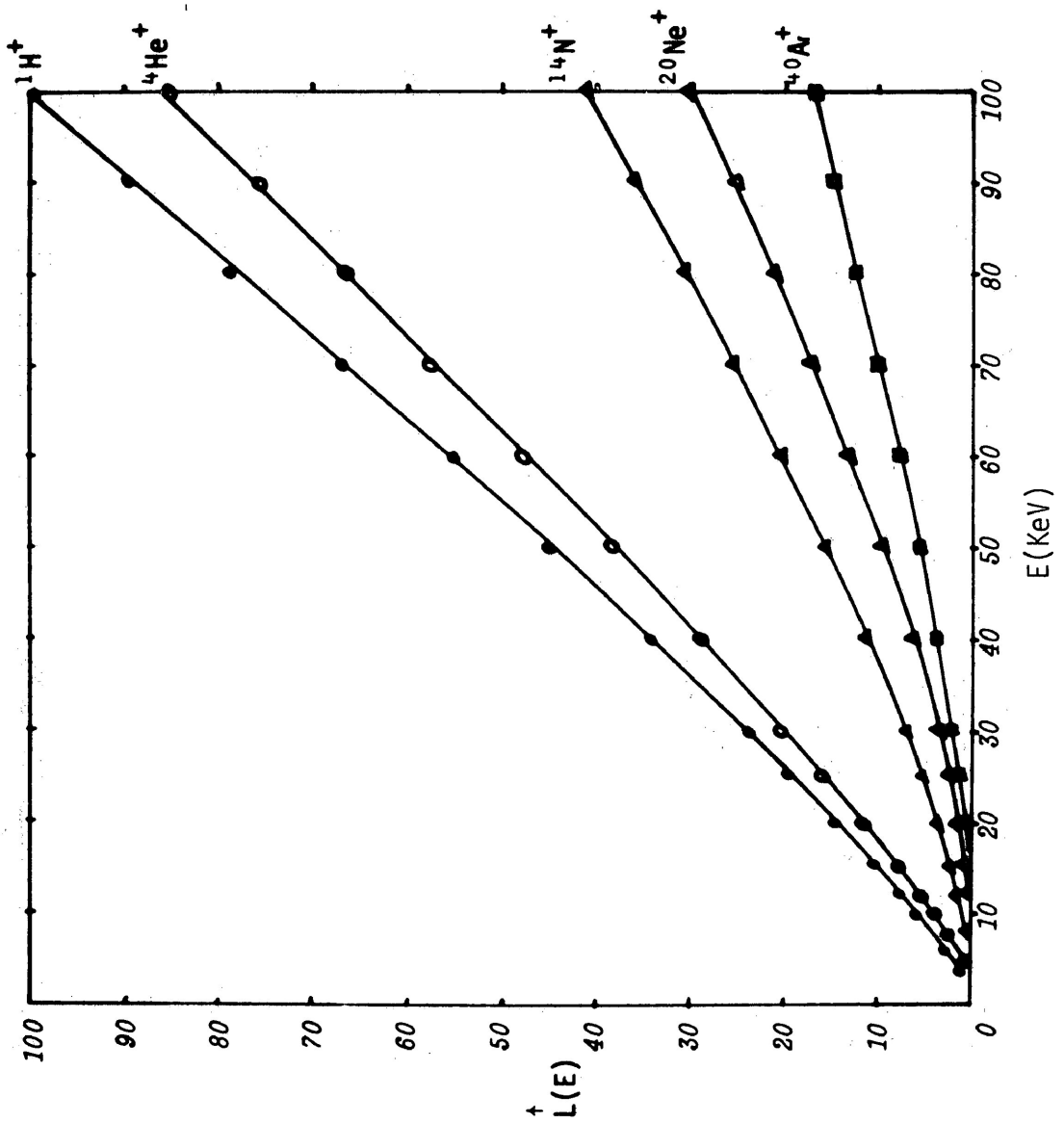

Fig. 41. A linear plot of L *versus* E for $^{1}H^{+}$, $^{4}He^{+}$, $^{14}N^{+}$, $^{20}Ne^{+}$ and $^{40}Ar^{+}$ ions impinging on ZnS:Ag;Cu (P-2, 21μ size).

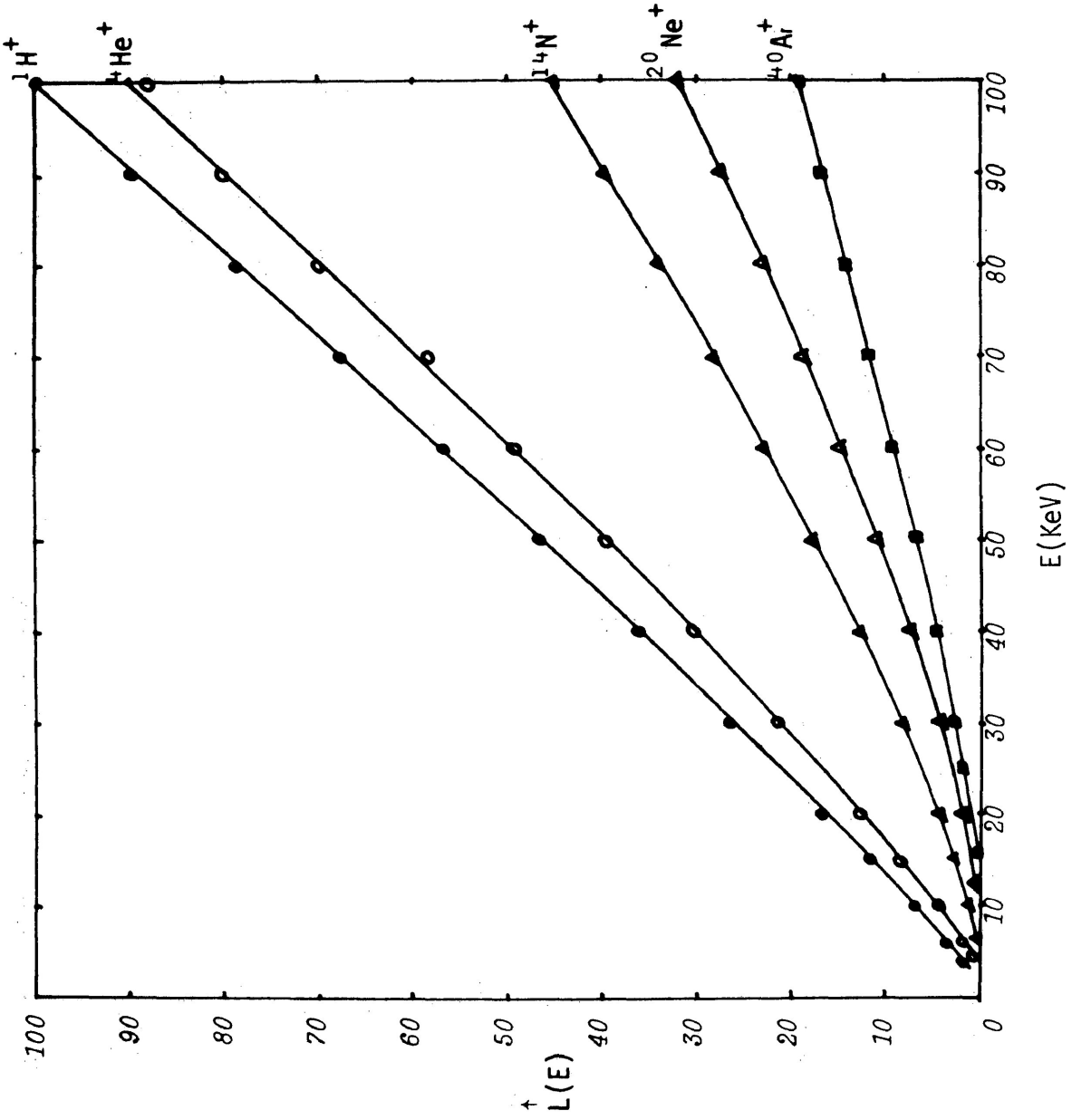

Fig. 42. A linear plot of L *versus* E for $^{1}H^{+}$, $^{4}He^{+}$, $^{14}N^{+}$, $^{20}Ne^{+}$ and $^{40}Ar^{+}$ ions impinging on ZnS:Cu (P-31, 11.5μ size).

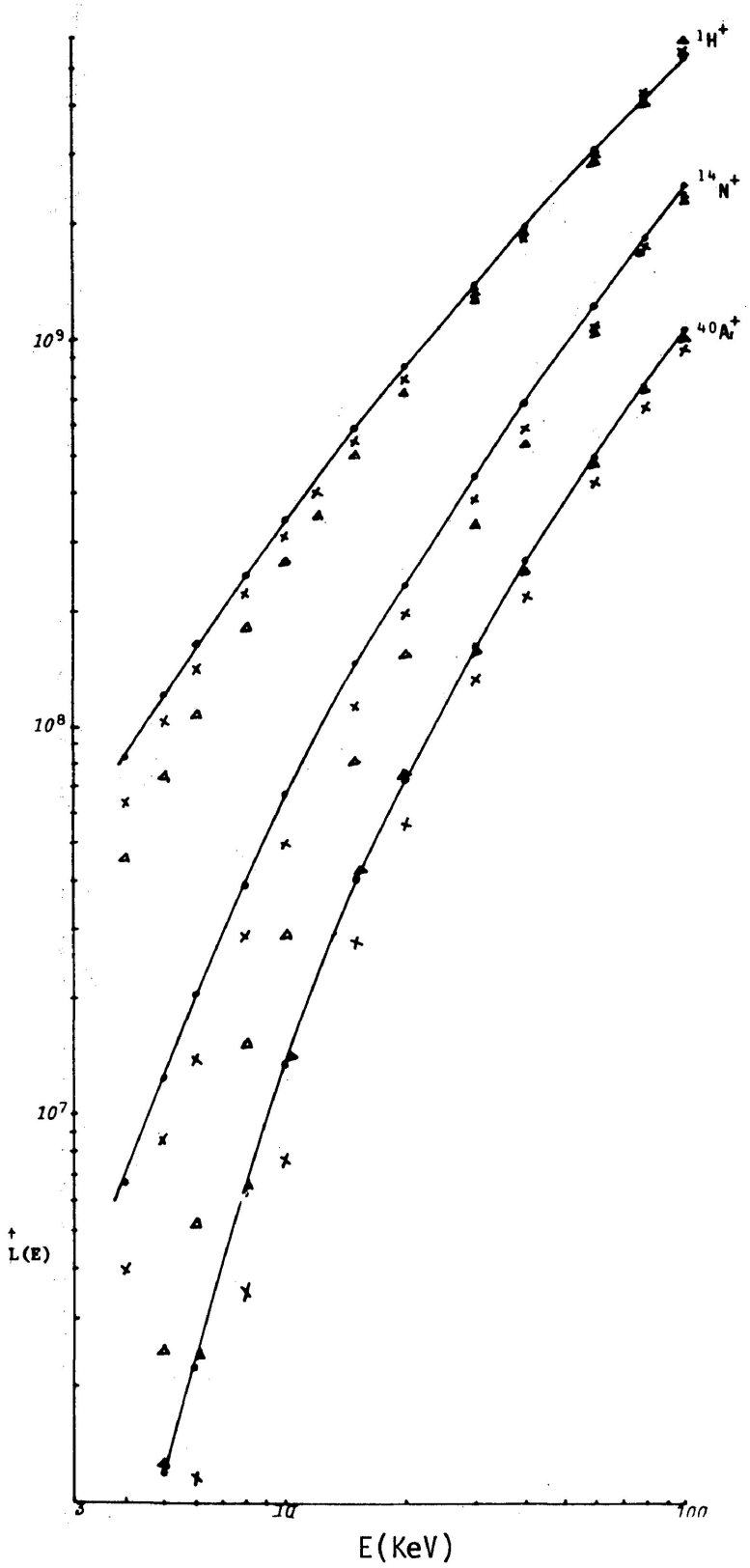

Fig. 43. A composite plot of L *versus* E for $^1H^+$, $^{14}N^+$ and $^{40}Ar^+$ ions impinging on ZnS:Ag of different particle size: 4μ(·); 10.5μ (x); and 7μ(Δ). The solid curves are drawn through the points of 4μ size sample.

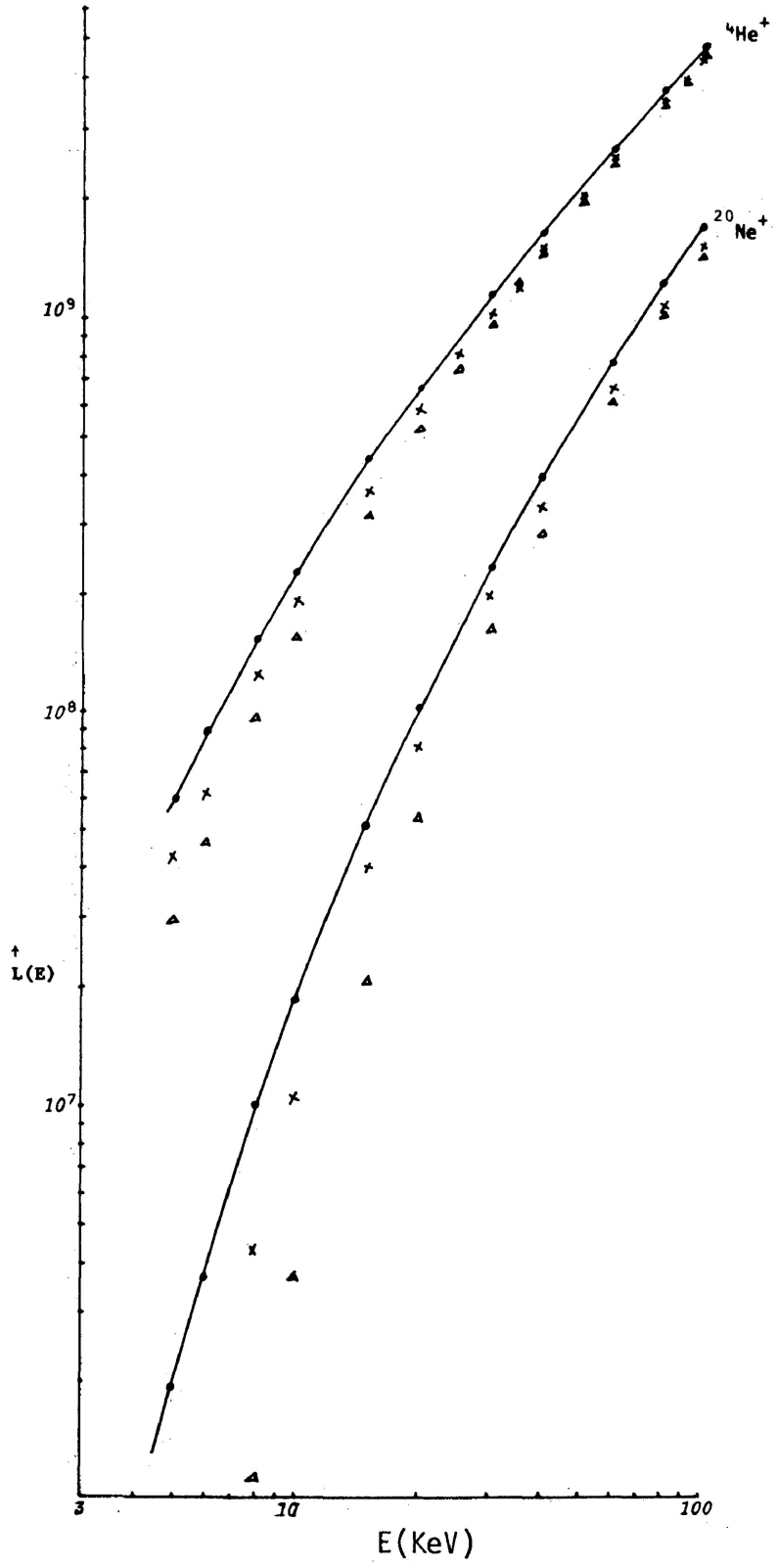

Fig. 44. A composite plot of L *versus* E for $^4He^+$ and $^{20}Ne^+$ ions impinging on ZnS:Ag of different particle size: 4μ(·); 10.5μ(x); and 7μ(Δ). The solid curves are drawn through the points of 4μ sample.

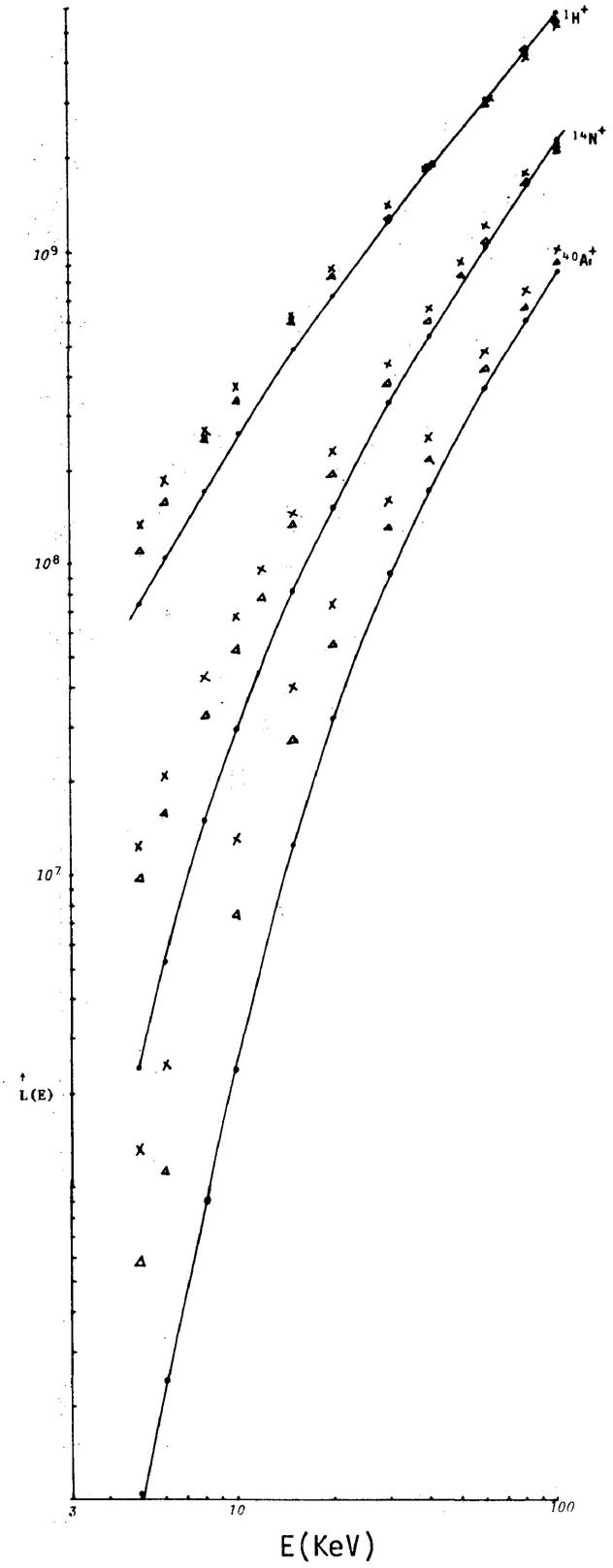

Fig. 45. A composite plot of L *versus* $^1H^+$, $^{14}N^+$ and $^{40}Ar^+$ ions impinging on ZnS:Ag (•), ZnS:Ag;Cu (Δ) and ZnS:Cu (x). The solid curves are drawn through the points of ZnS:Ag.

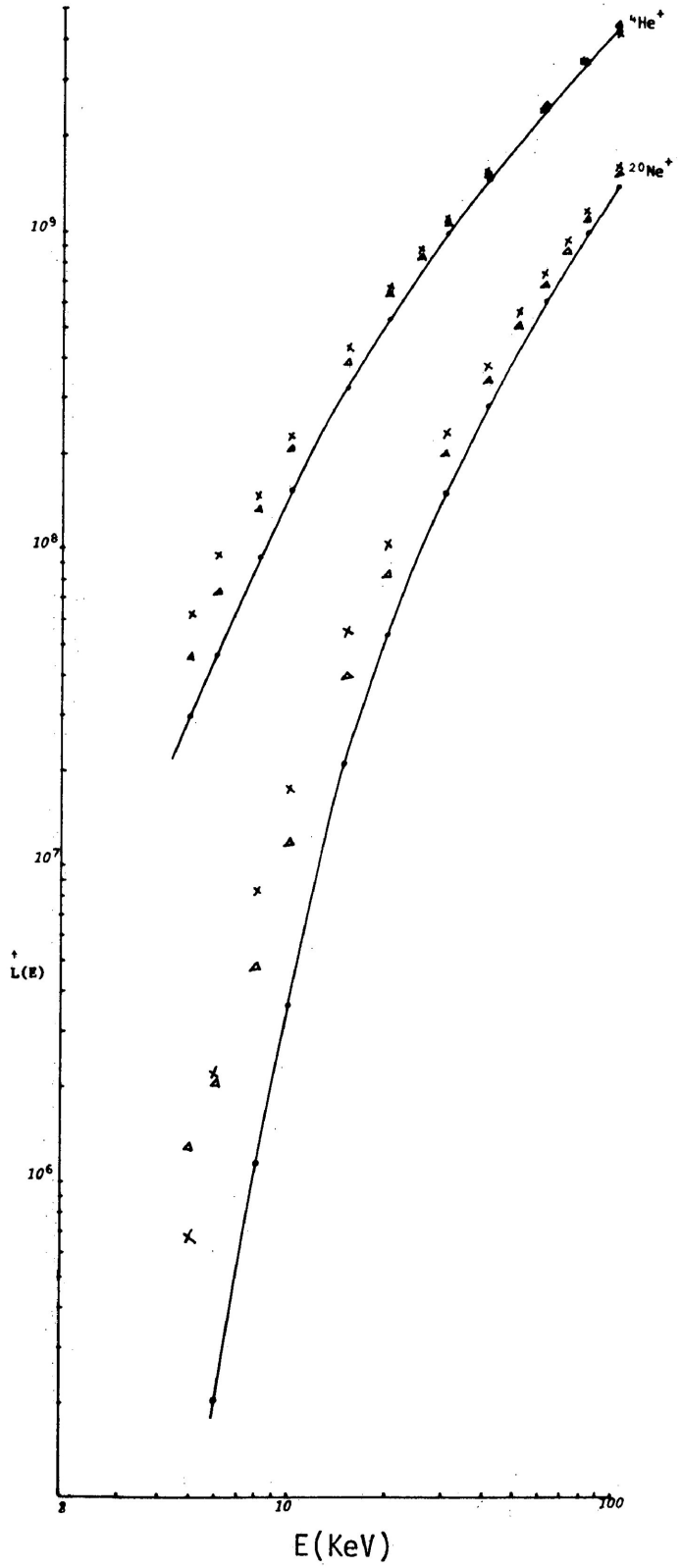

Fig. 46. A composite plot of L *versus* E for $^4He^+$ and $^{20}Ne^+$ ions impinging on ZnS:Ag (·), ZnS:Ag;Cu (Δ) and ZnS:Cu (x). The solid curves are drawn through the points of ZnS:Ag.

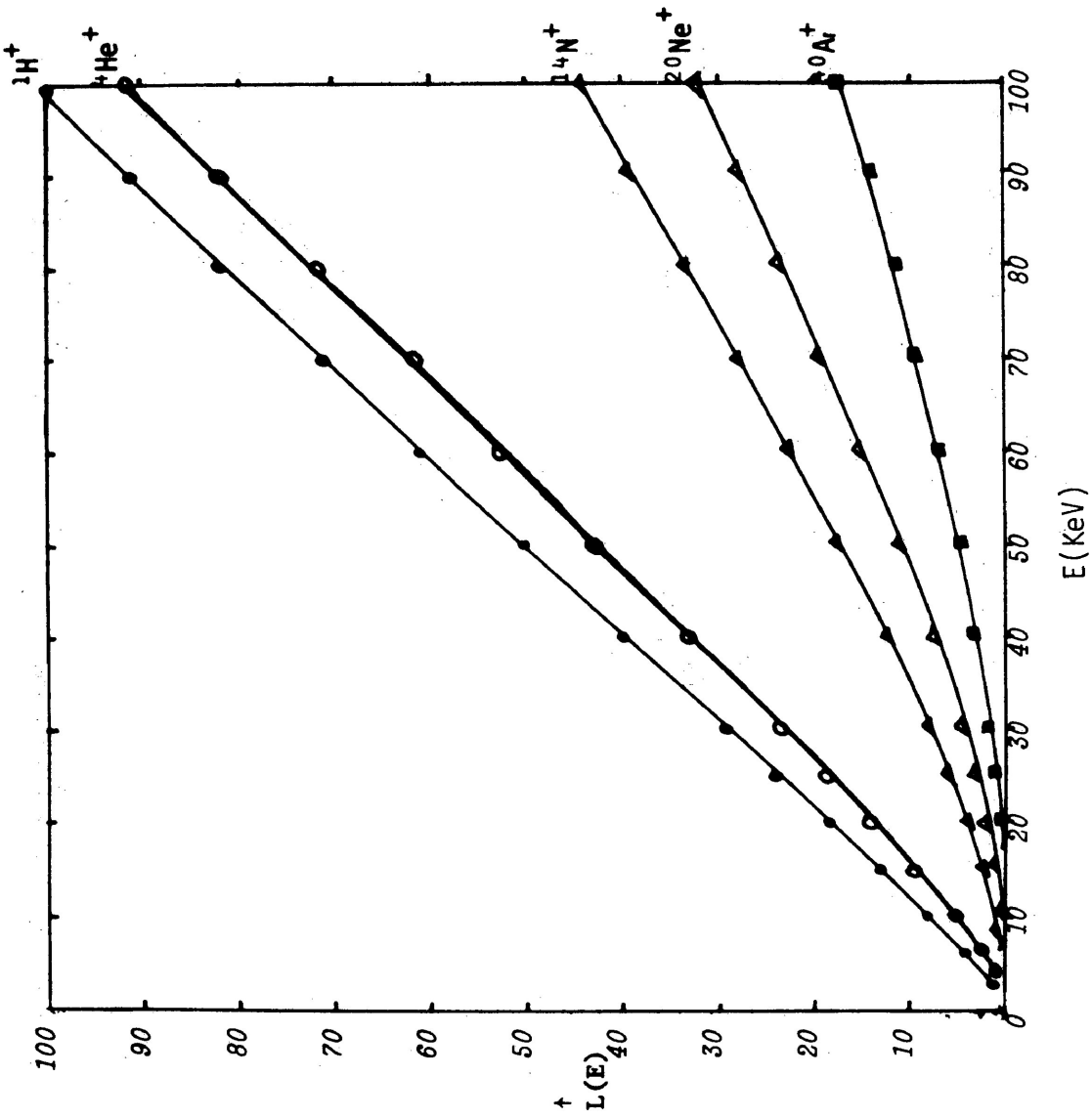

Fig. 47. A linear plot of L *versus* E for $^{1}H^{+}$, $^{4}He^{+}$, $^{14}N^{+}$, $^{20}Ne^{+}$ and $^{40}Ar^{+}$ ions impinging on ZnCdS:Ag (fine).

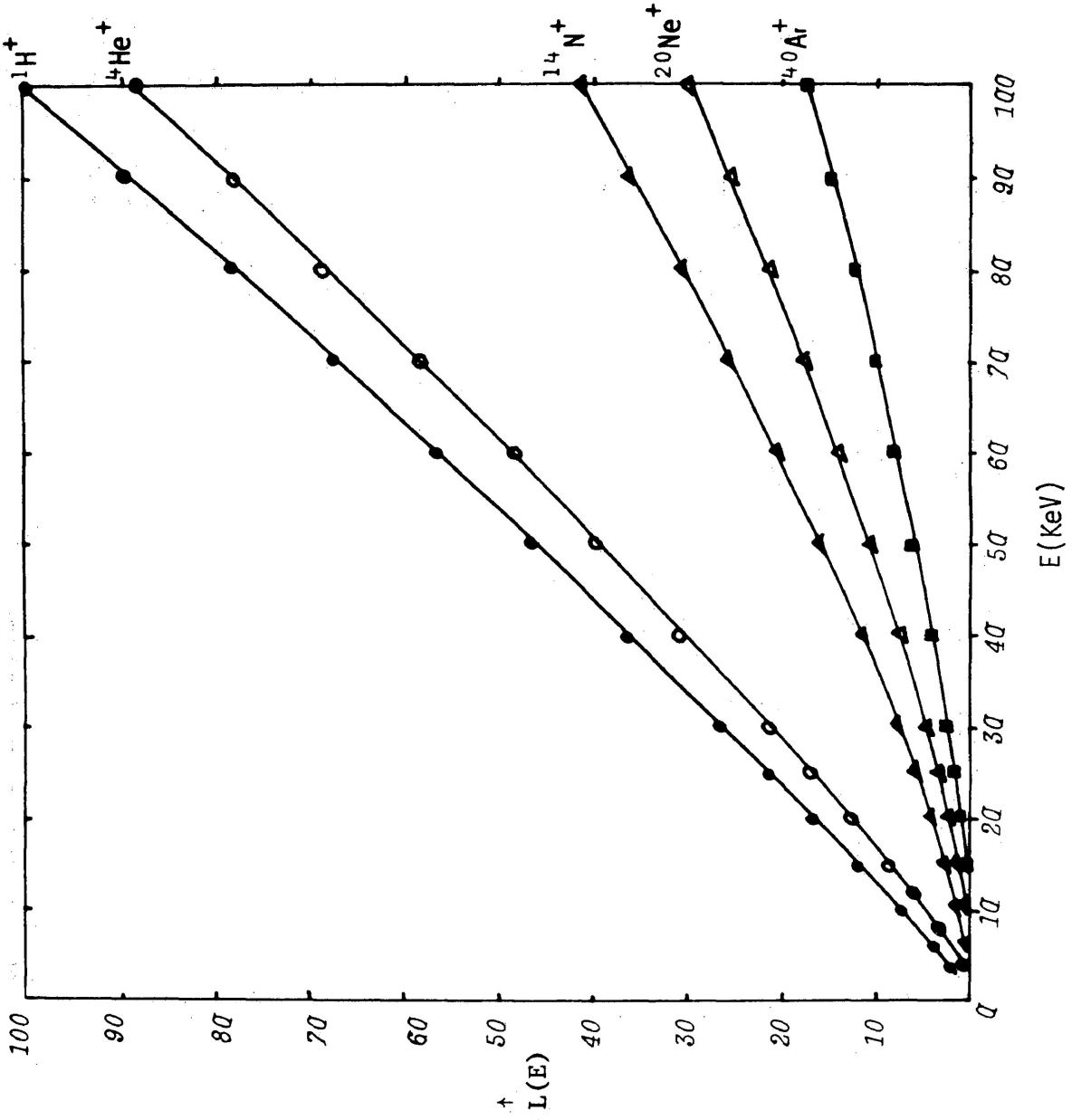

Fig. 48. A linear plot of L *versus* E for $^{1}H^{+}$, $^{4}He^{+}$, $^{14}N^{+}$, $^{20}Ne^{+}$ and $^{40}Ar^{+}$ ions impinging on ZnCdS:Ag.

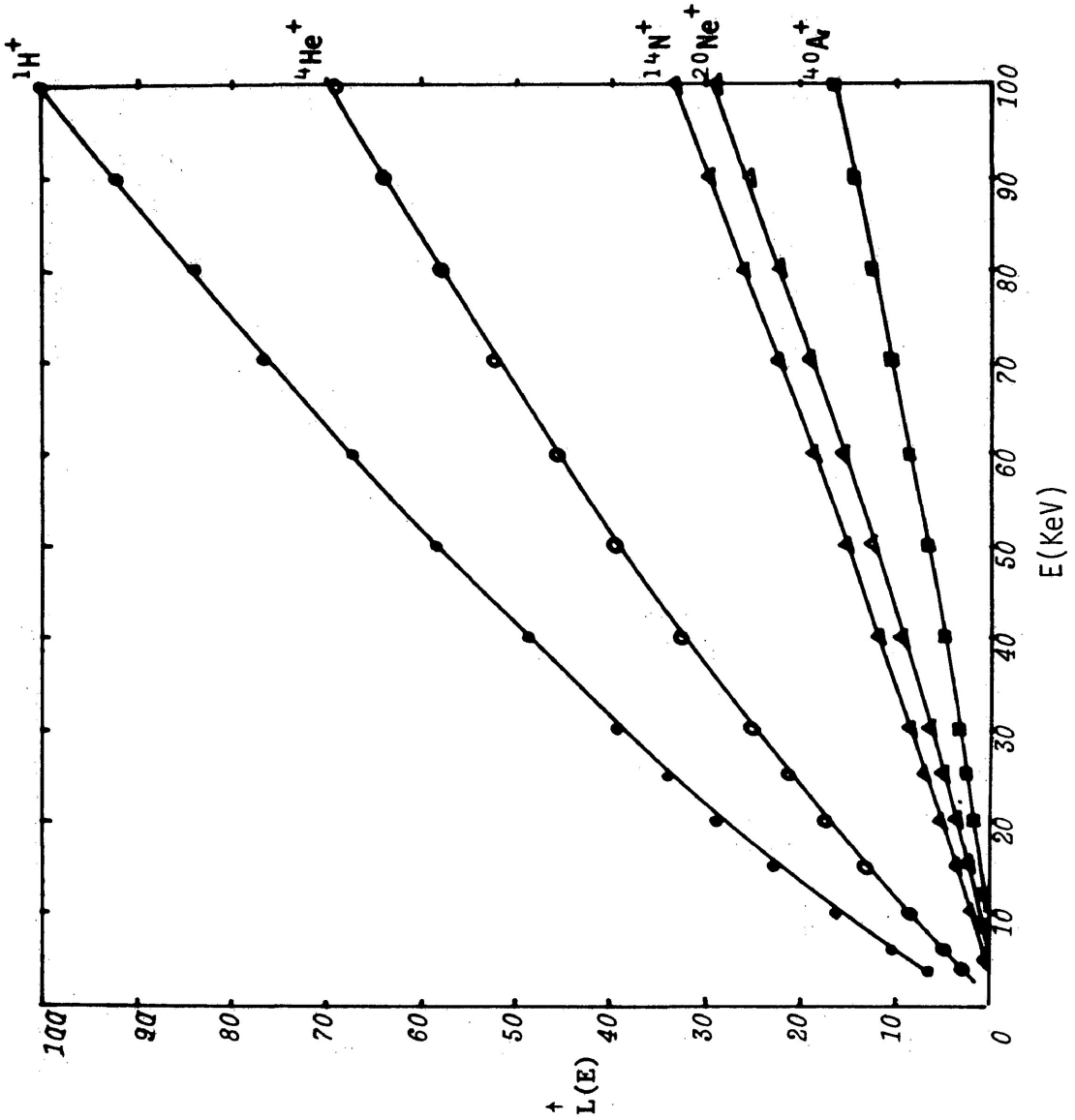

Fig. 49. A linear plot of L *versus* E for $^{1}H^{+}$, $^{4}He^{+}$, $^{14}N^{+}$, $^{20}Ne^{+}$ and $^{40}Ar^{+}$ ions impinging on $CaWO_4$.

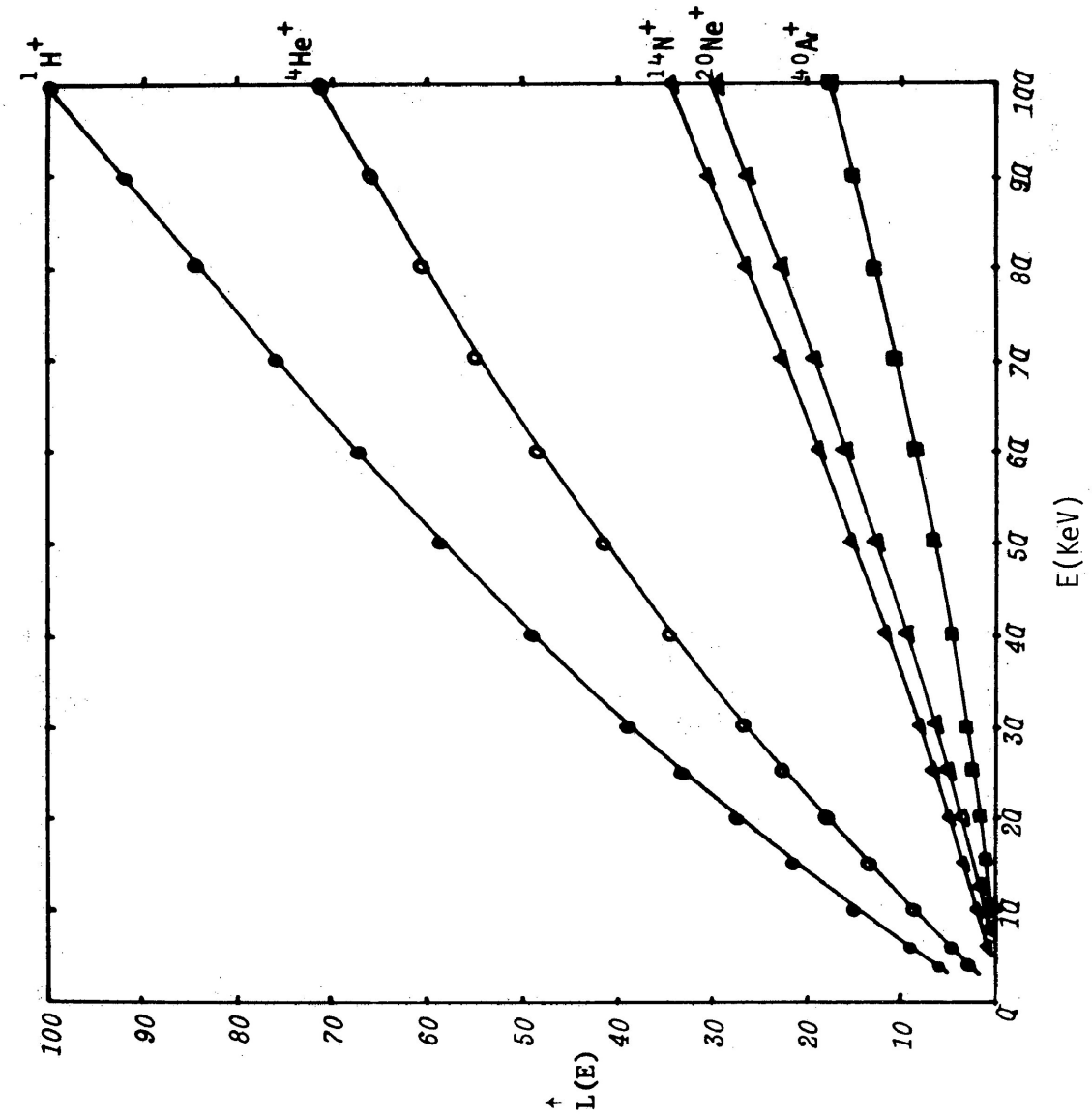

Fig. 50. A linear plot of L *versus* E for $^{1}H^{+}$, $^{4}He^{+}$, $^{14}N^{+}$, $^{20}Ne^{+}$ and $^{40}Ar^{+}$ ions impinging on $CaWO_4$ (fine).

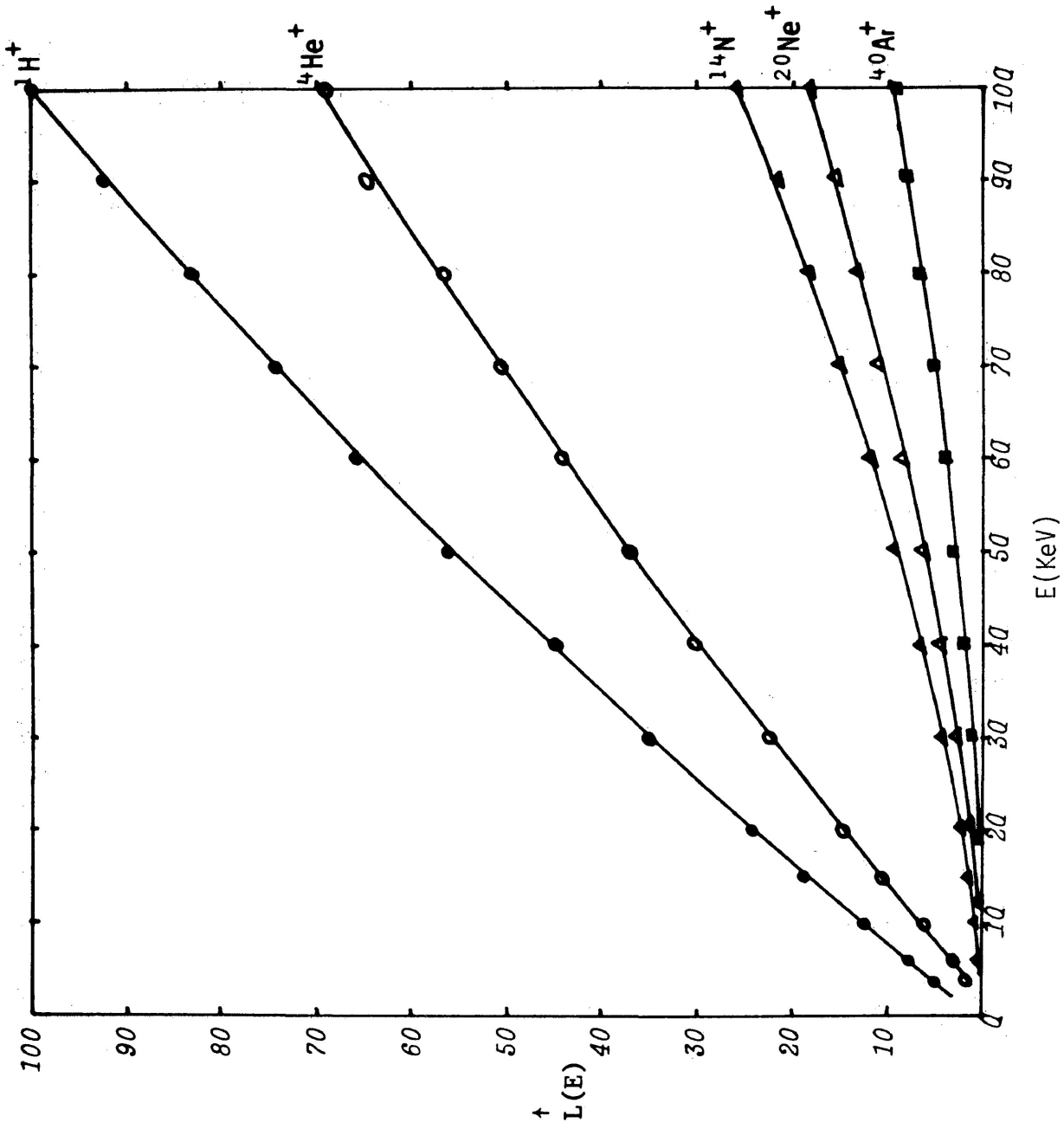

Fig. 51. A linear plot of L *versus* E for $^{1}H^{+}$, $^{4}He^{+}$, $^{14}N^{+}$, $^{20}Ne^{+}$ and $^{40}Ar^{+}$ ions impinging on YVO_4:Eu.

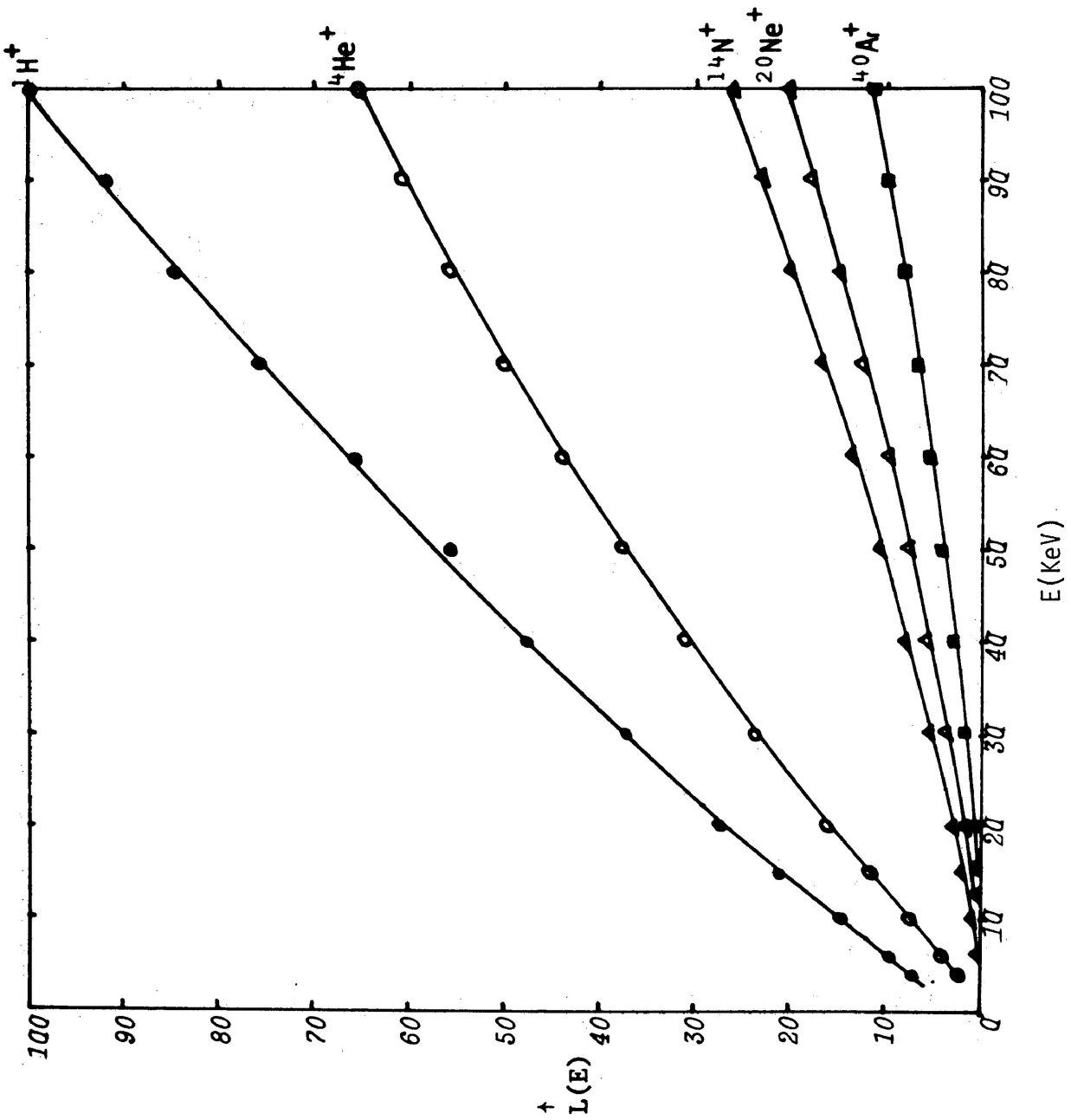

Fig. 52. A linear plot of L *versus* E for $^{1}H^{+}$, $^{4}He^{+}$, $^{14}N^{+}$, $^{20}Ne^{+}$ and $^{40}Ar^{+}$ ions impinging on YVO_4:Eu,Bi.

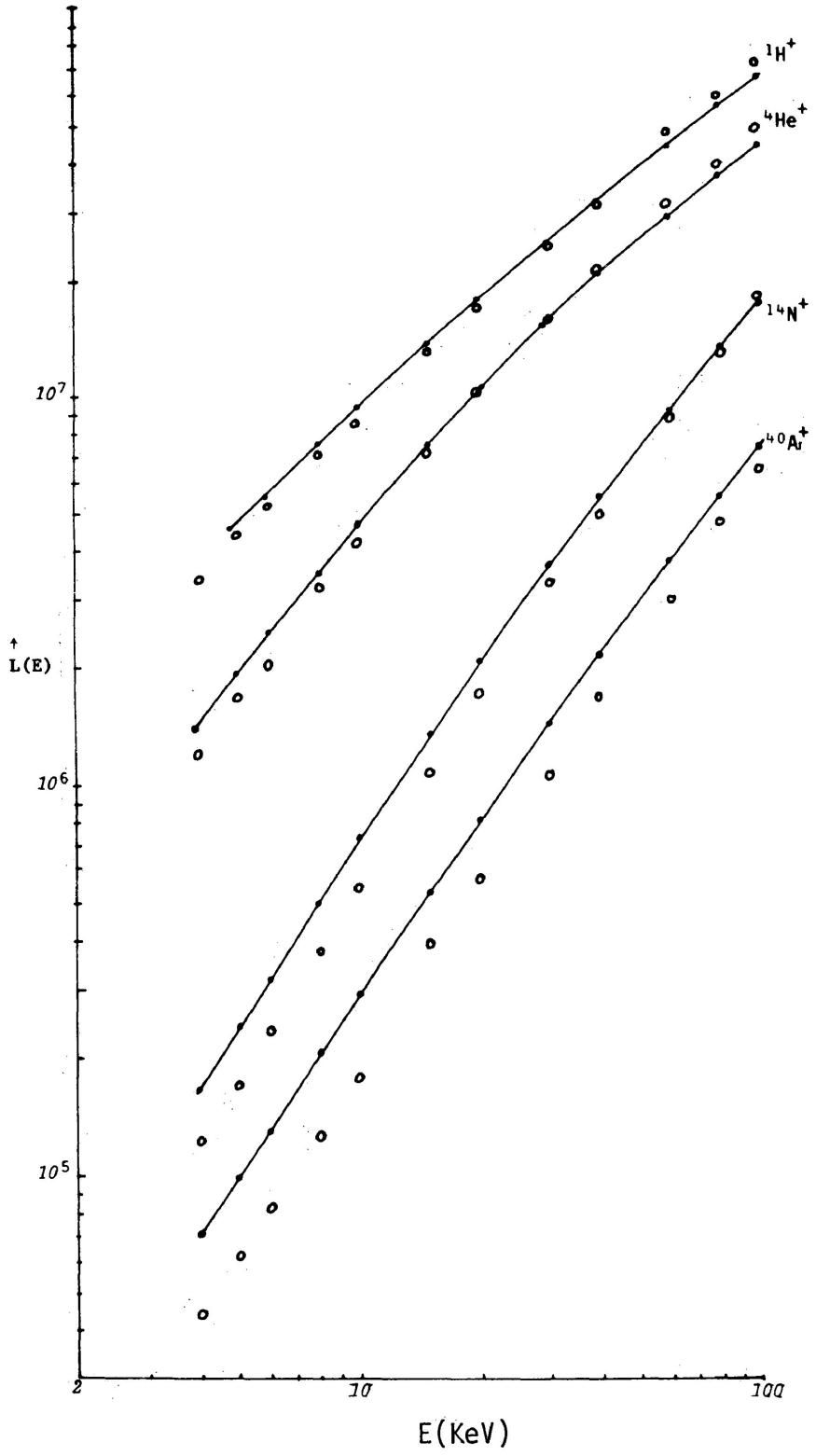

Fig. 53. A composite plot of L *versus* E for $^1H^+$, $^4He^+$, $^{14}N^+$ and $^{40}Ar^+$ ions impinging on YVO_4:Eu;Bi (·) and YVO_4:Eu (o). The solid curves are drawn through the points of YVO_4:Eu;Bi.

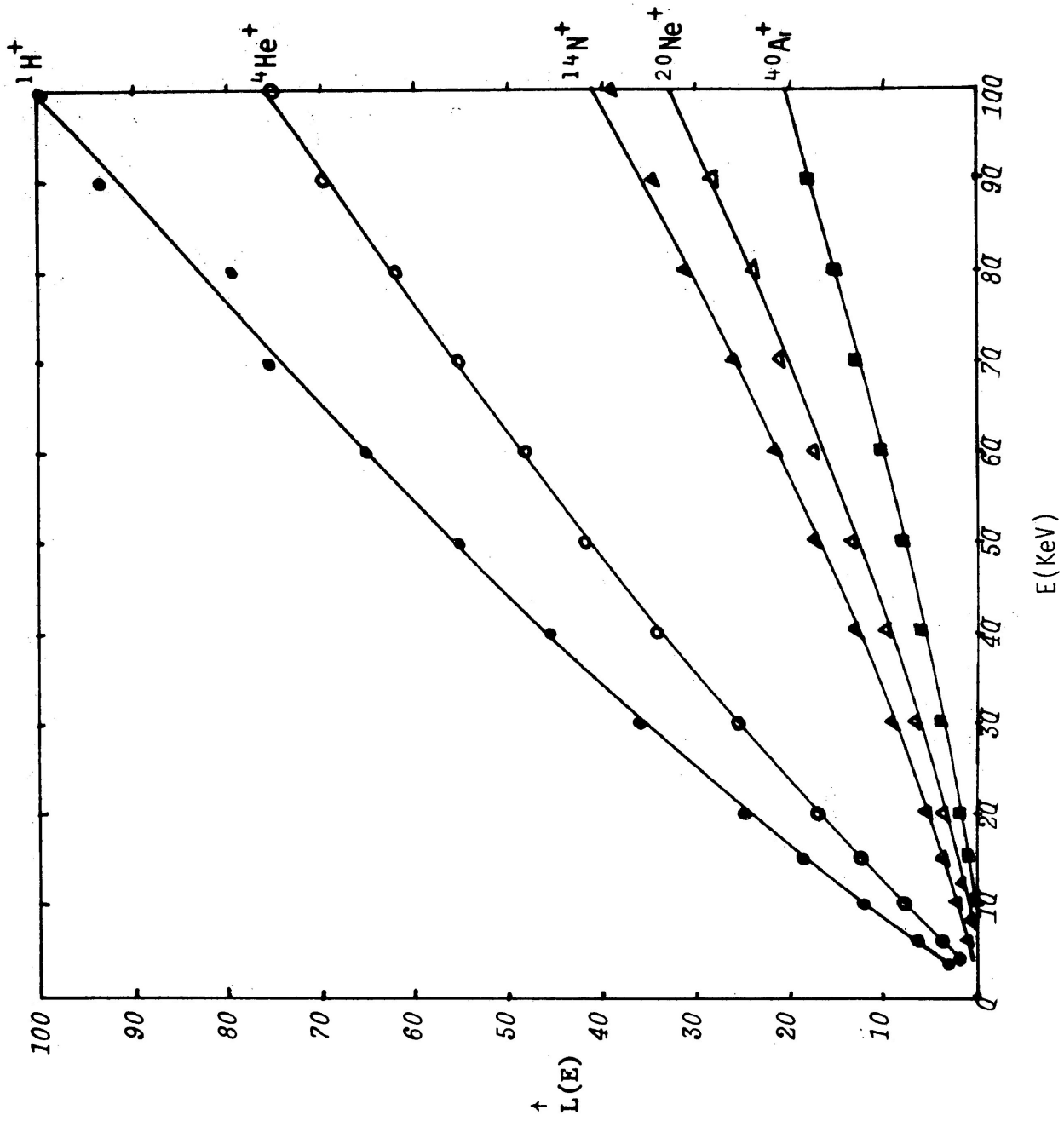

Fig. 54. A linear plot of L *versus* E for $^{1}H^{+}$, $^{4}He^{+}$, $^{14}N^{+}$, $^{20}Ne^{+}$ and $^{40}Ar^{+}$ ions impinging on $KMgF_3$:Mn.

(2) The light output *versus* energy curves are linear only within a certain energy range. For heavy ions, the curves are distinctly non-linear with curvature concave toward the energy axis. For light ions, the curves were either concave away from or toward the energy axis, depending on the phosphor.

(3) Surface effects appear to play an important role in some of the phosphors, especially in ZnS and ZnCdS phosphors.

(4) The shape of the L *versus* E curves, as well as the relative spacing between the curves for ions of different masses, is different from phosphor to phosphor.

The shape of the observed curves can be classified into three kinds according to the shape of $^{1}H^{+}$ and $^{4}He^{+}$ curves:

(i) Zn_2SiO_4:Mn, ZnO:Zn and Y_2O_2S:Eu phosphors in which the L *versus* E plots for $^{1}H^{+}$ and $^{4}He^{+}$ are approximately straight lines.

(ii) ZnS and ZnCdS phosphors in which the experimental curves are concave toward the energy axis. Surface effects are very pronounced in these phosphors.

(iii) $CaWO_4$, YVO_4 and $KMgF_3$:Mn phosphors in which the $^{1}H^{+}$ and $^{4}He^{+}$ curves are concave away from the energy axis.

It is possible that saturation occurs due to the high specific electronic energy loss of the low energy ions. Surface effects do not seem to appear in these phosphors, perhaps because of low mobility charge transfer mechanisms.

A composite plot of L *versus* E curves for Zn_2SiO_4:Mn phosphors, as displayed in Fig. 37, illustrates the luminescent response from 2μ, 5μ and 10μ particle size Zn_2SiO_4:Mn phosphors when bombarded by ions. The $^{1}H^{+}$ curves of 2μ and 5μ size samples were first normalized to yield

the $^{1}H^{+}$ curve of 10μ size sample, the normalization constant was then used to normalize the rest of the curves. (In order to avoid confusion the $^{20}Ne^{+}$ curves are not shown in Fig. 37.) It is seen that the slopes, as well as the relative magnitudes of L, are slightly different.

In Figs. 43 and 44 are compared the luminescent responses of three ZnS:Ag phosphors of different particle size (7μ, 10.5μ and 4μ), and in Figs. 45 and 46 are displayed the differences in luminescent response of ZnS:Ag, ZnS:Ag:Cu and ZnS:Cu phosphors with different activators, as well as crystal structure. It is clearly illustrated that the shape of the L *versus* E curves and the relative spacing of the curves for ions of different masses are essentially different, especially at lower energies. The relatively large observed differences at lower energies suggest that surface effects play an important role in ZnS phosphors.

Results of experiments using ZnCdS:Ag (P-20) and ZnCdS:Ag (P-22) phosphors are shown in Figs. 43 to 46. Overall, the shapes of the curves are similar to those from ZnS phosphors. It is seen that the L values, as well as the relative spacing, are slightly different especially for heavy ions at lower energies.

Europium-activated and europium-bismuth-activated yttrium vanadate phosphors have different luminescent responses, as shown in Fig. 53. The difference in light output between $^{1}H^{+}$ and $^{40}Ar^{+}$ for YVO_4:Eu is about 20 percent larger than for the YVO_4:Eu,Bi phosphor. Both phosphors exhibit line spectra. The reason for the differences in luminescent response of these phosphors is not clear; a possible explanation is that the presence of the additional bismuth activator has altered the luminescence mechanism and thus influenced either surface recombination or saturation effects.

The curvature of the L *versus* E curves for $^{1}H^{+}$ and $^{4}He^{+}$ is likely due to saturation of the luminescence mechanism. The broken lines passing through the experimental points in Figs. 55 to 66 show the observed light output as a function of ion energy for $^{1}H^{+}$, $^{14}N^{+}$, $^{40}Ar^{+}$, $^{4}He^{+}$ and $^{20}Ne^{++}$ ion bombarding ZnO:Zn, Zn_2SiO_4:Mn, $CaWO_4$ and ZnS samples. The solid curves represent the predicted relationships between L and E given by Eqn. (1). The constant C in this equation was adjusted so as to normalize the theoretical curve for $^{40}Ar^{+}$ to the correspondingly observed light output at 50 KeV in all samples studied. The value of C was then used to compute the values of L as a function of ion energy for hydrogen, helium, nitrogen and neon.

From Figs. 55 and 56, which show the results obtained from the ZnO:Zn sample, it may be noted that the experimental values of L lie close to the theoretical curves. The light output at higher energies is less than predicted. However, the discrepancy between corresponding functional relationships is not large; the slopes of the predicted curves for heavy ions are approximately 10 percent larger than the corresponding experimental curves, and for lighter ions the difference is roughly 6 percent.

The results of the Zn_2SiO_4:Mn sample, as shown in Figs. 57 and 58, are identical to those observed by van Wijngaarden *et al.*,[6] the experimental L values for nitrogen, neon and argon lie close to the theoretical curves within experimental uncertainty. However, the observed differences between the light output for helium and neon are both about a factor of two higher than the correspondingly predicted differences. Figs. 59 and 60 display the results obtained from the $CaWO_4$ sample. The differences between the experimental and theoretical results are similar to those

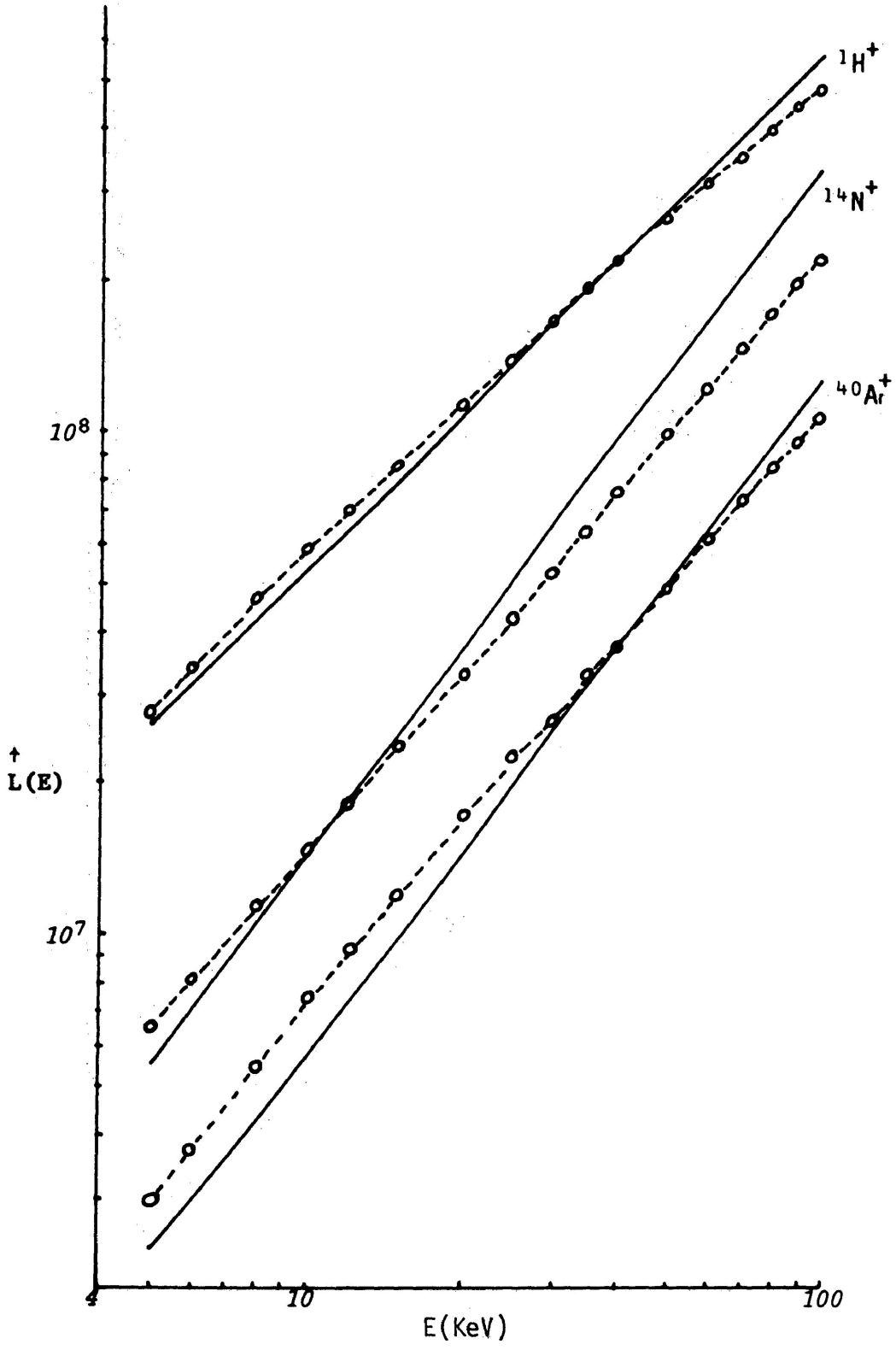

Fig. 55. A logarithmic plot of L *versus* E for $^1H^+$, $^{14}N^+$ and $^{40}Ar^+$ ions impinging on ZnO:Zn. The solid curves represent the appropriate theoretical function [Eqn. (1)]. The broken lines are drawn through the experimental points.

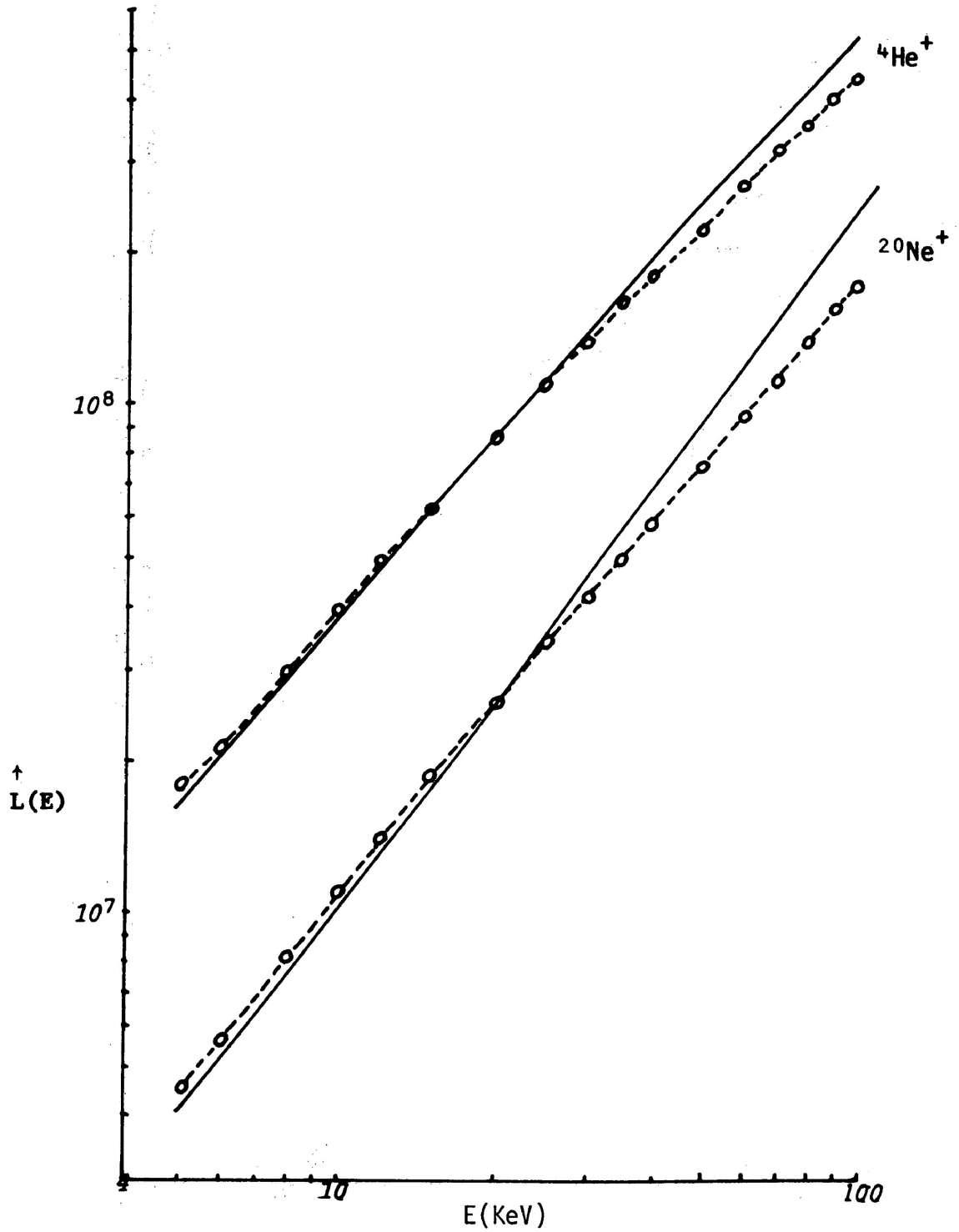

Fig. 56. A logarithmic plot of L *versus* E for $^4He^+$ and $^{20}Ne^+$ ions impinging on ZnO:Zn. The solid curves represent the theoretical function [Eqn. (1)]. The broken lines are drawn through the experimental points.

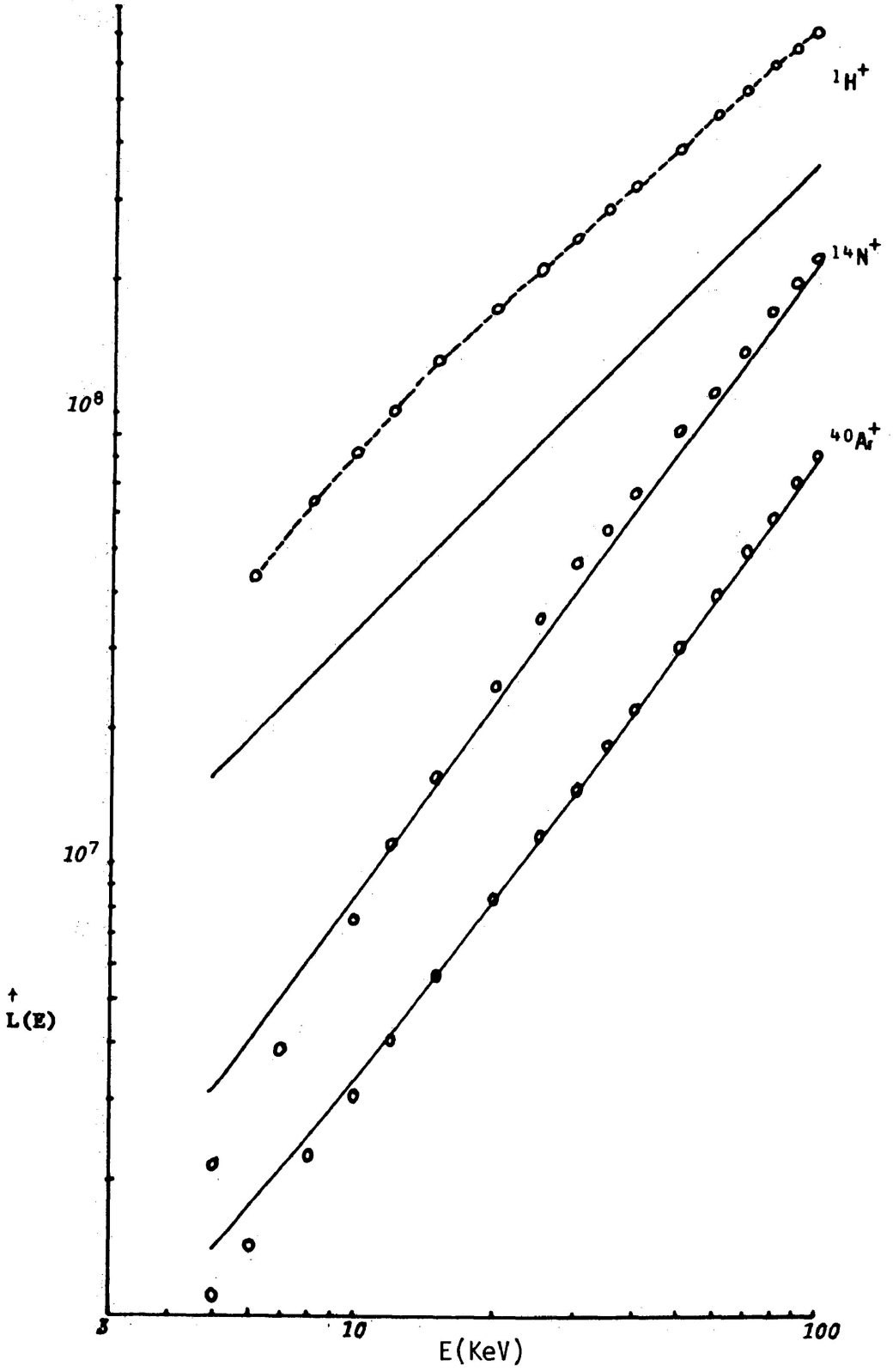

Fig. 57. A logarithmic plot of L *versus* E for $^1H^+$, $^{14}N^+$ and $^{40}Ar^+$ ions impinging on Zn_2SiO_4:Mn (2μ size). The solid curves represent the appropriate theoretical function [Eqn. (1)]. The broken line is drawn through the experimental points of $^1H^+$.

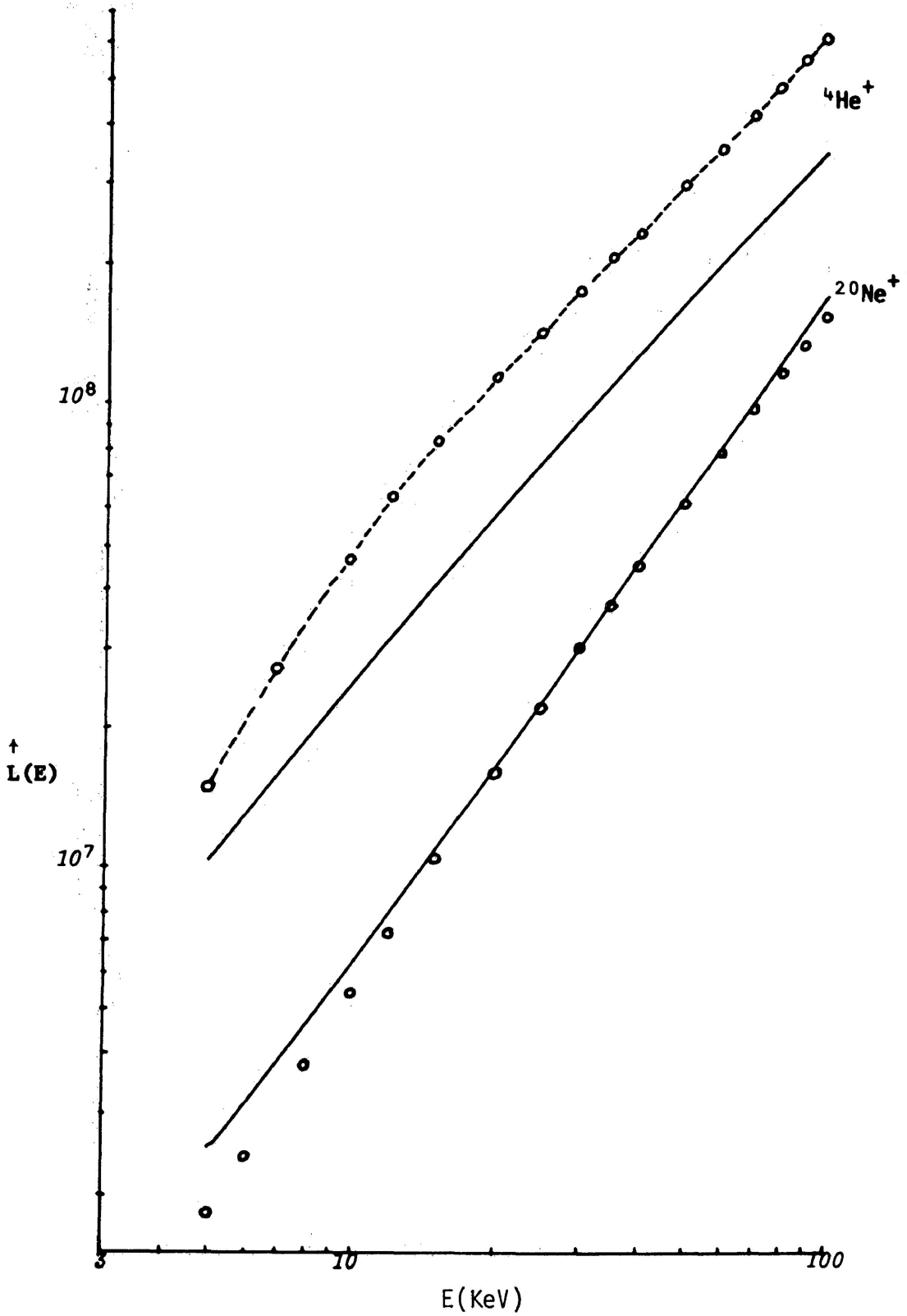

Fig. 58. A logarithmic plot of L *versus* E for $^4He^+$ and $^{20}Ne^+$ ions impinging on Zn_2SiO_4:Mn (2μ size). The solid curves represent the appropriate theoretical function [Eqn. (1)]. The broken line is drawn through the experimental points of $^4He^+$.

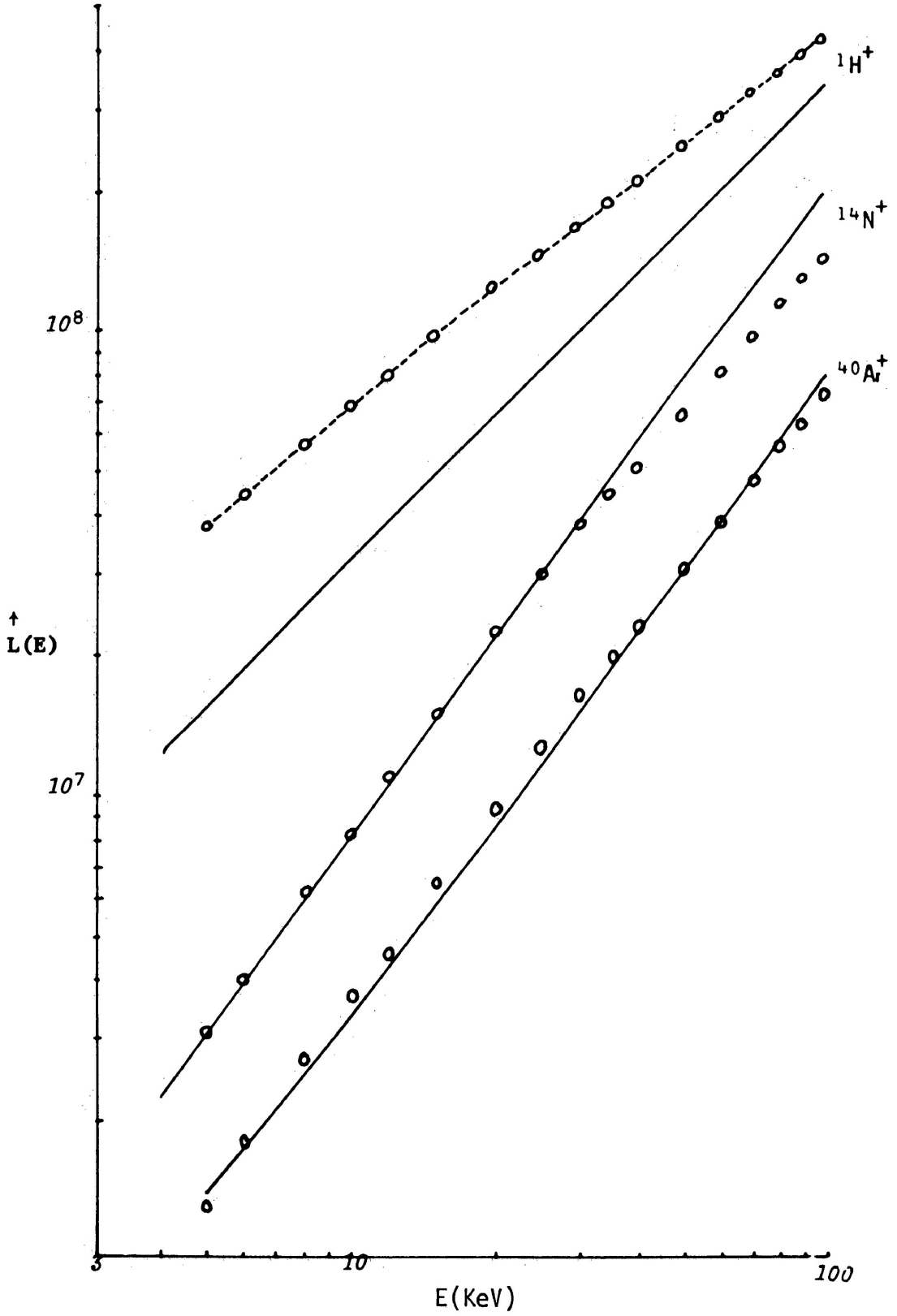

Fig. 59. A logarithmic plot of L *versus* E for $^1H^+$, $^{14}N^+$ and $^{40}Ar^+$ ions impinging on $CaWO_4$. The solid curves represent the appropriate theoretical function [Eqn. (1)]. The broken line is drawn through the experimental points of $^1H^+$.

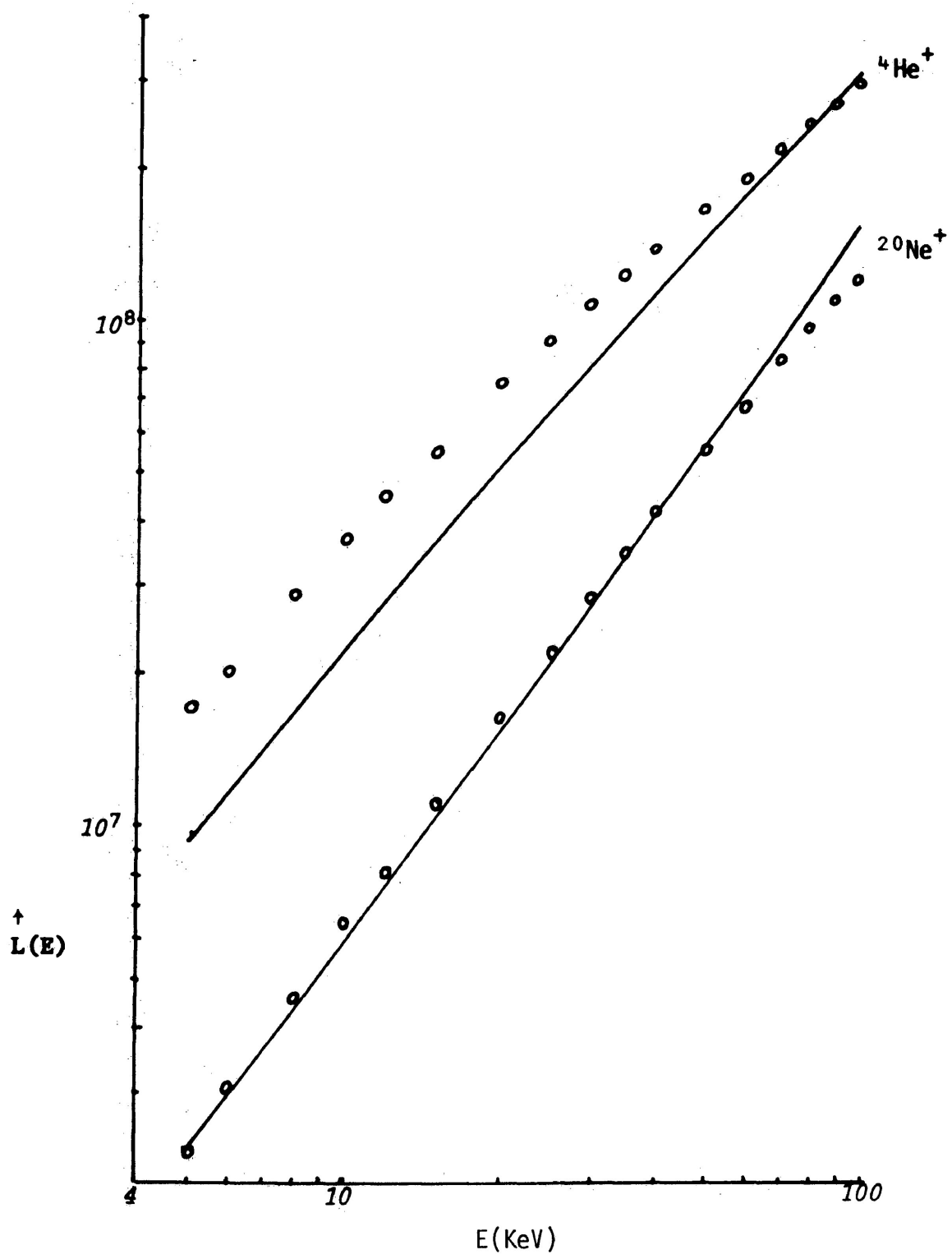

Fig. 60. A logarithmic plot of L *versus* E for $^4He^+$ and $^{20}Ne^+$ ions impinging on $CaWO_4$. The solid curves represent the appropriate theoretical function [Eqn. (1)].

obtained with Zn_2SiO_4:Mn. Comparing the solid curves with the experimental points, it can be seen that the relative magnitude of the predicted L values for $^{14}N^+$, $^{20}Ne^+$ and $^{40}Ar^+$ agree roughly with the experiments. There is a small discrepancy between the predicted and the observed functional relationships, especially at higher energies. The overall agreement between theory and experiment in Zn_2SiO_4:Mn and $CaWO_4$ samples for ions heavier than helium, however, seems reasonably good.

The large discrepancy at lower energies between the predicted and the observed functional relationships, as well as the differences in relative magnitude of L values in ZnS:Ag, ZnS:Cu and ZnS:Ag:Cu phosphors, are clearly illustrated in Figs. 61 and 62, Figs. 63 and 64, and Figs. 65 and 66, respectively. Since all the ZnS curves are concave toward the energy axis, a surface recombination is evident.

From the above results, it appears that the variation of the ionoluminescence intensity with ion energy and ion mass can only be interpreted approximately on the basis of the theoretical expression, Eqn. (1). This equation reduces to $L(E) = CE$ for light projectiles in the KeV energy range, where $S_e >> S_n$. For larger masses, S_n becomes an appreciable fraction of the total stopping cross section. The relative importance of S_n increases rapidly with decreasing energy and thus there is only a small amount of energy available for electron excitation. Thus L(E) increases with increasing projectile energy and decreases with increasing mass of the projectile. The discrepancy between the theory and experiments indicates that C is not a constant. Several plausible reasons may be considered:

(1) C might be a function of the projectile velocity[6] because the ratio

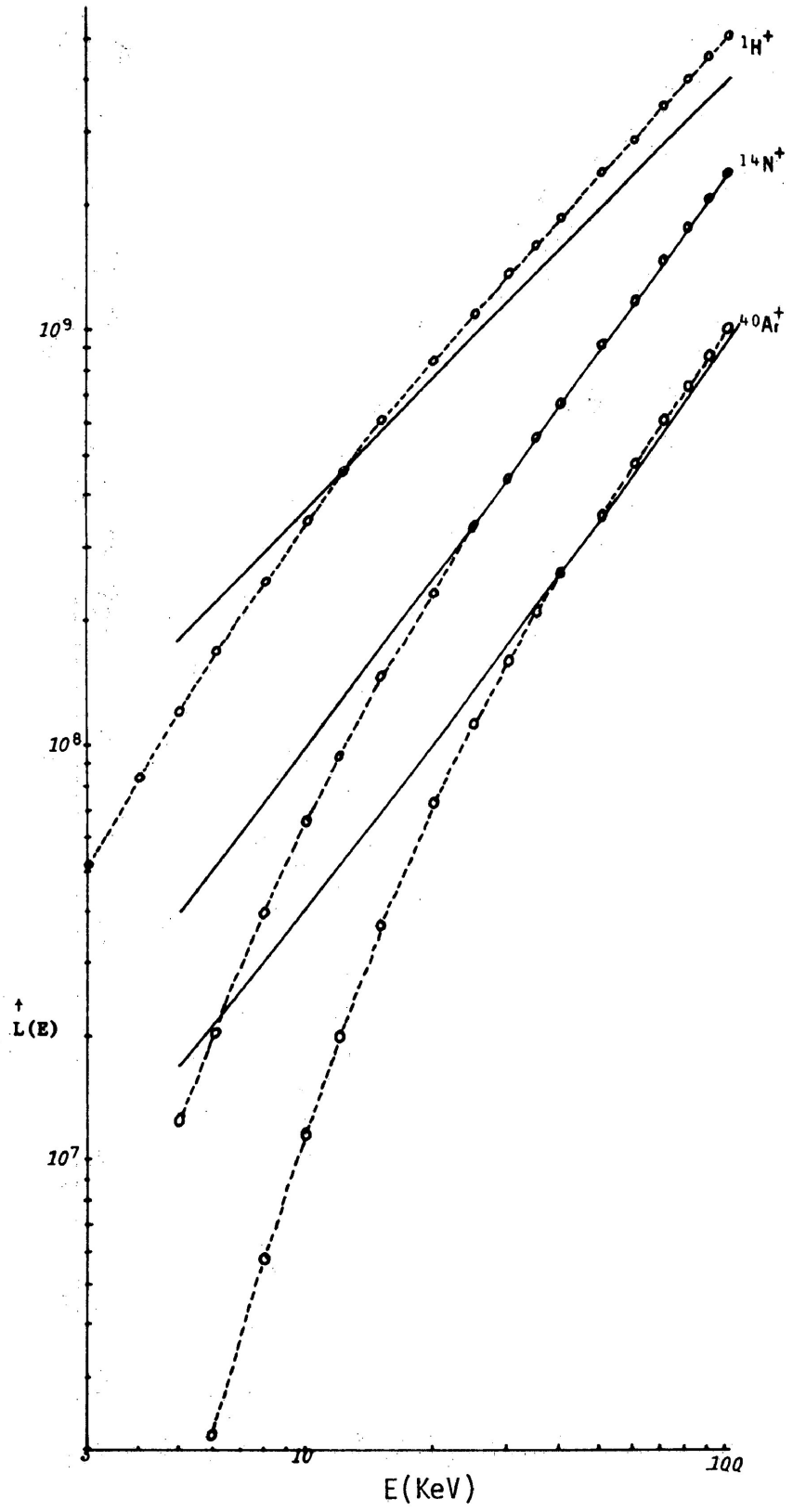

Fig. 61. A logarithmic plot of L *versus* E for $^1H^+$, $^{14}N^+$ and $^{40}Ar^+$ ions impinging on ZnS:Ag. The solid curves represent the appropriate theoretical function [Eqn. (1)]. The broken lines are drawn through the experimental points.

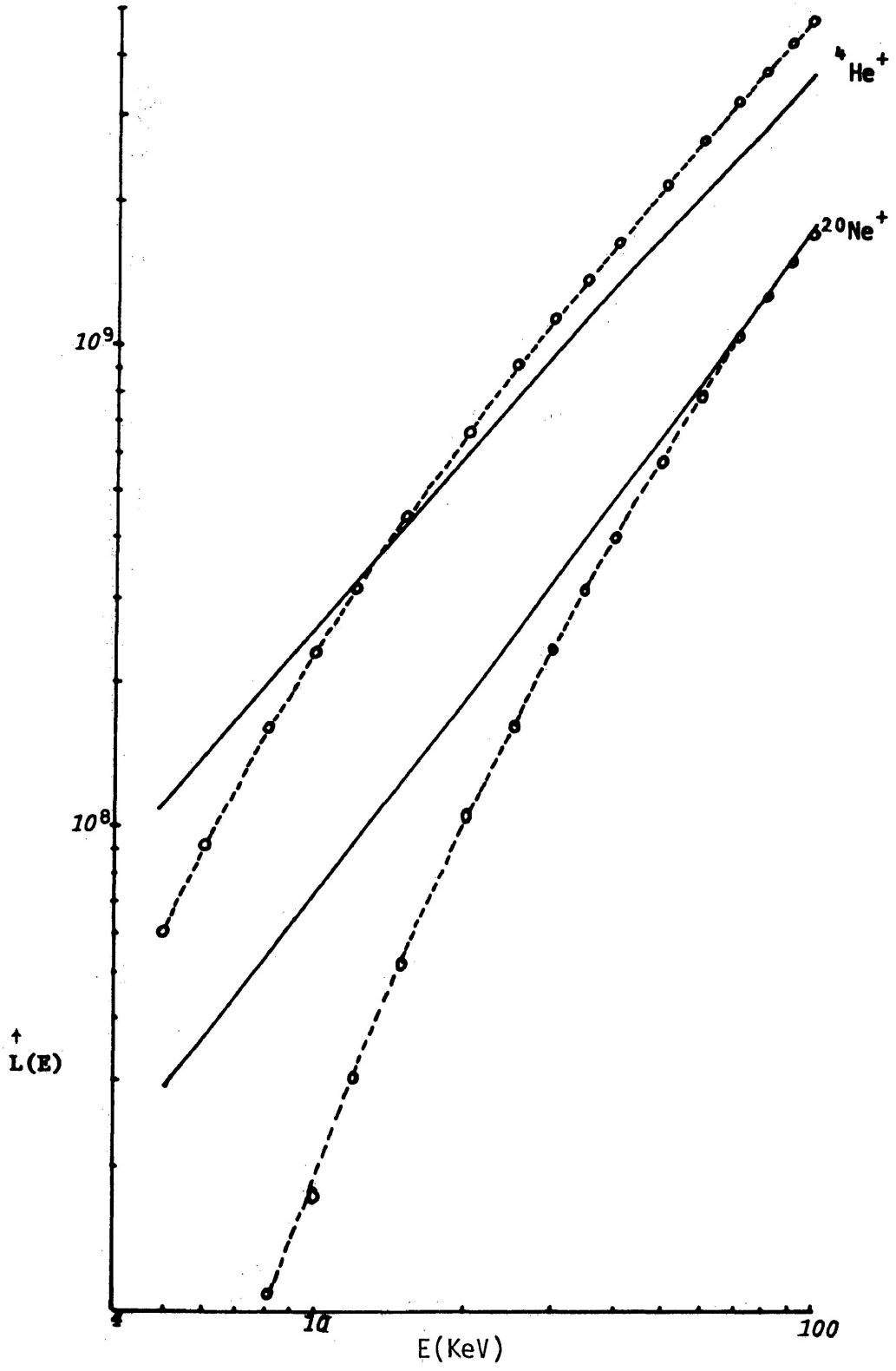

Fig. 62. A logarithmic plot of L *versus* E for $^4He^+$ and $^{20}Ne^+$ ions impinging on ZnS:Ag. The solid curves represent the appropriate theoretical function [Eqn. (1)]. The broken lines are drawn through the experimental points.

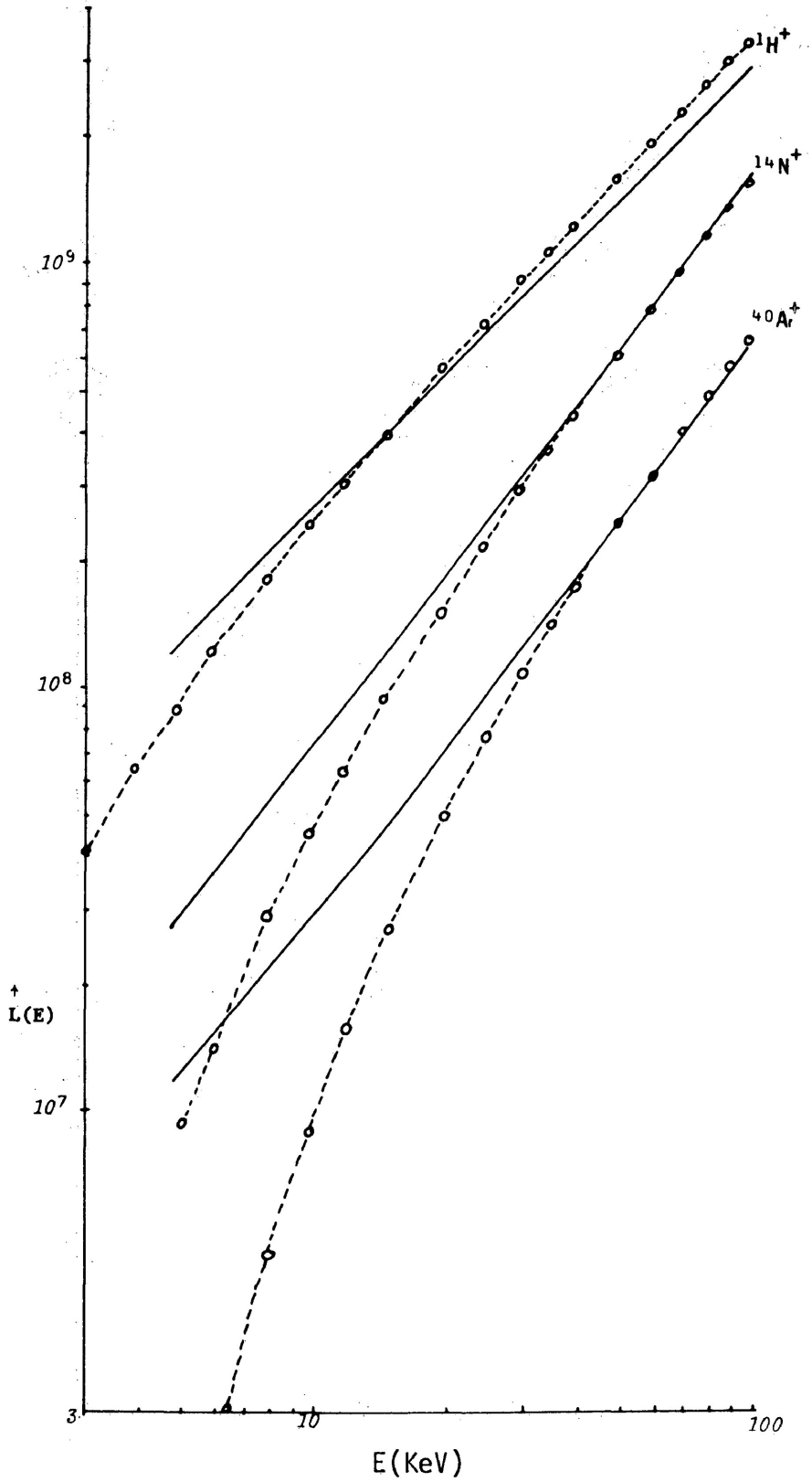

Fig. 63. A logarithmic plot of L *versus* E for $^1H^+$, $^{14}N^+$ and $^{40}Ar^+$ ions impinging on ZnS:Cu. The solid curves represent the appropriate theoretical function [Eqn. (1)]. The broken lines are drawn through the experimental points.

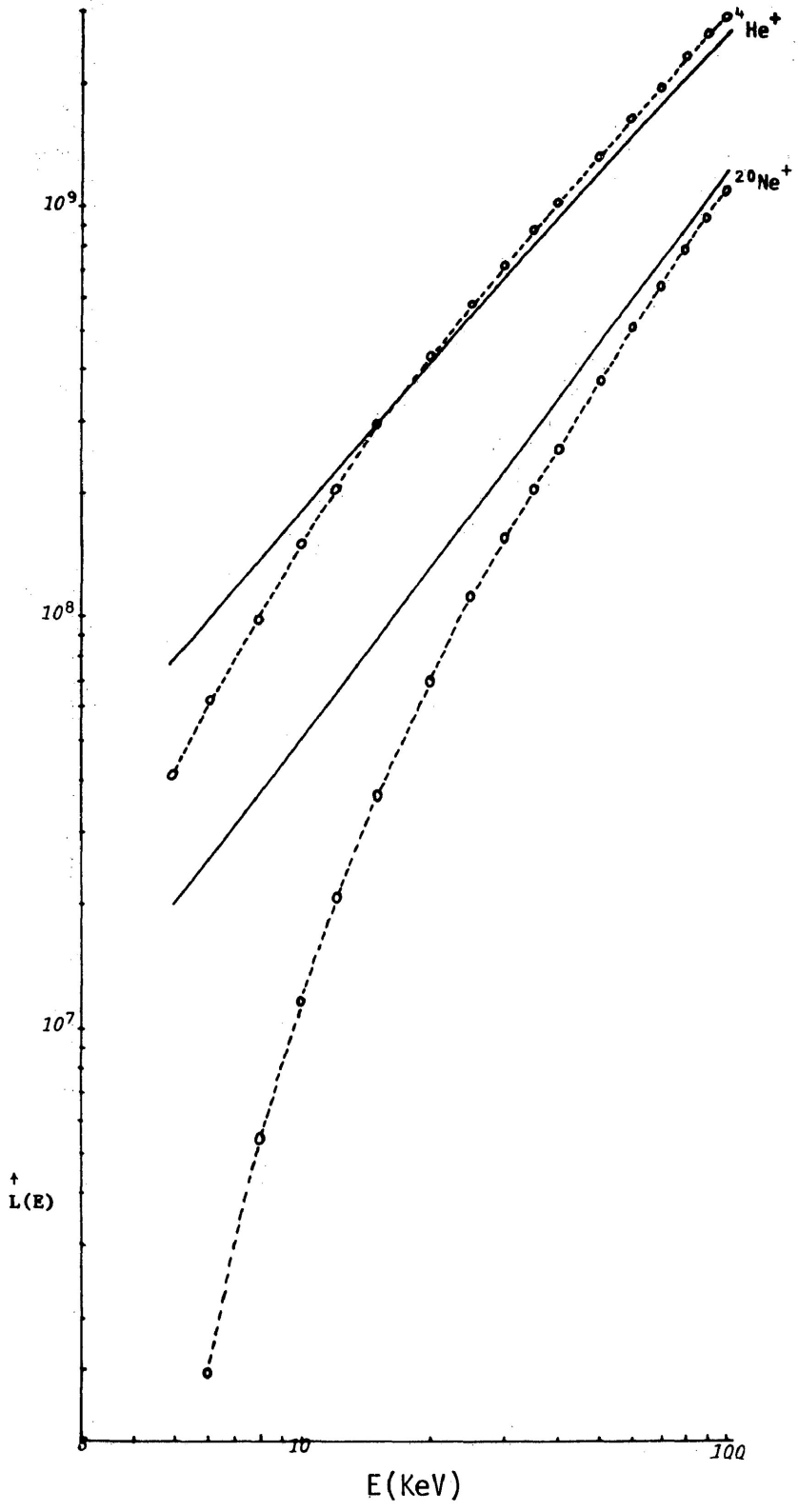

Fig. 64. A logarithmic plot of L *versus* E for $^4He^+$ and $^{20}Ne^+$ ions impinging on ZnS:Cu. The solid curves represent the appropriate theoretical function [Eqn. (1)]. The broken lines are drawn through the experimental points.

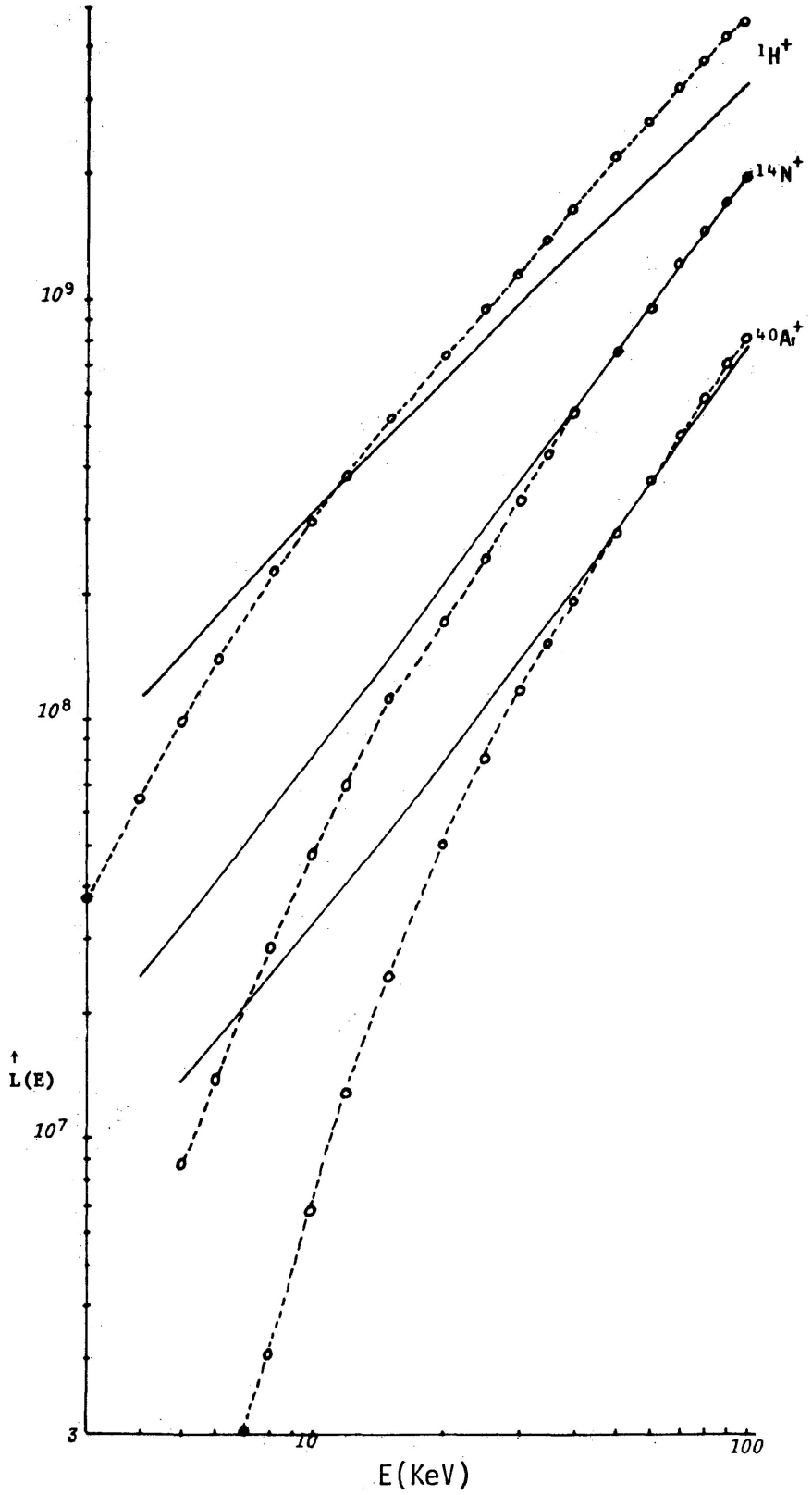

Fig. 65. A logarithmic plot of L *versus* E for $^1H^+$, $^{14}N^+$ and $^{40}Ar^+$ ions impinging on ZnS:Ag;Cu. The solid curves represent the appropriate theoretical function [Eqn. (1)]. The broken lines are drawn through the experimental points.

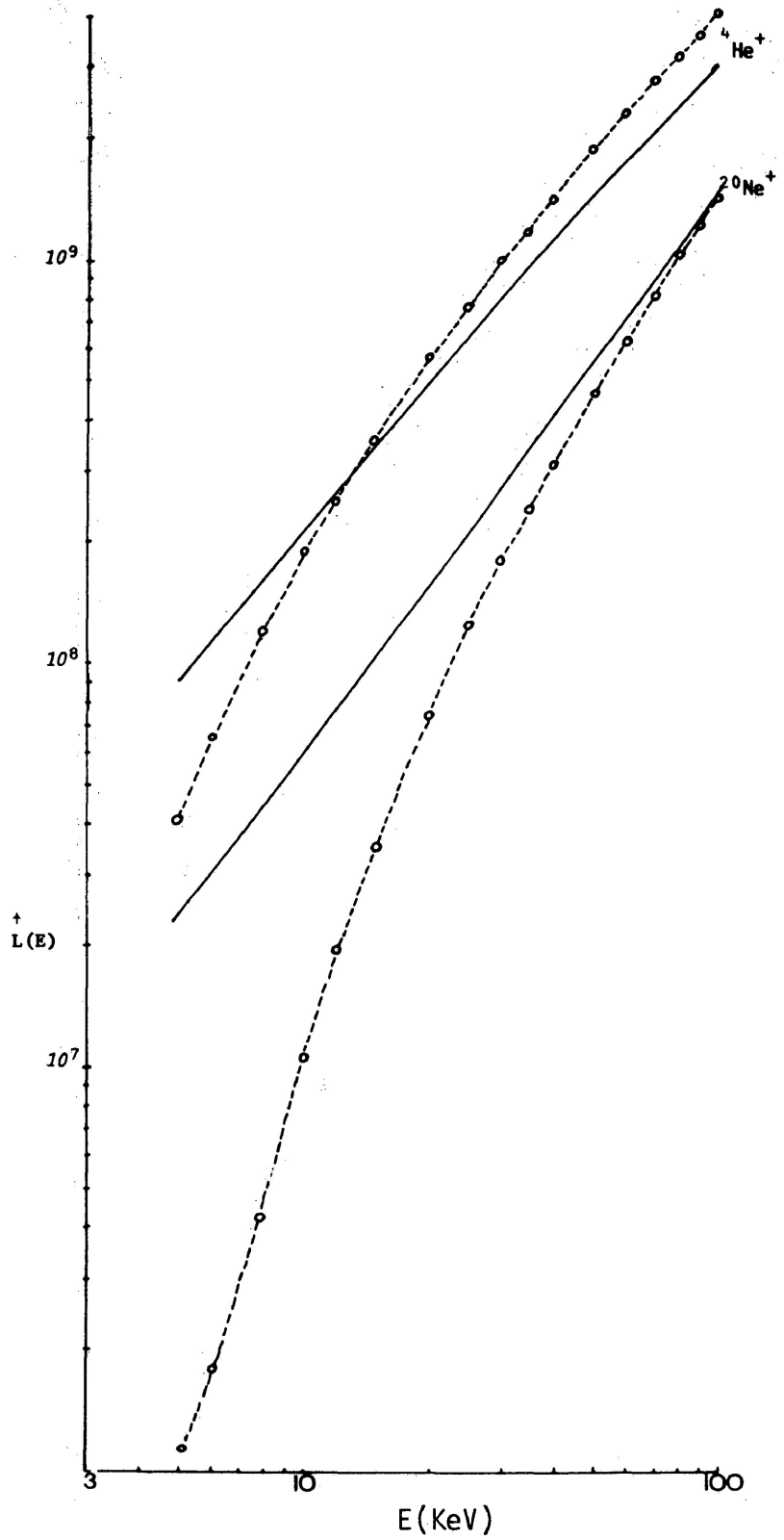

Fig. 66. A logarithmic plot of L *versus* E for $^4He^+$ and $^{20}Ne^+$ ions impinging on ZnS:Ag;Cu. The solid curves represent the appropriate theoretical function [Eqn. (1)]. The broken lines are drawn through the experimental points.

of the radiative to non-radiative transitions is expected to be velocity dependent.

(2) Experimental results for $CaWO_4$ and YVO_4 phosphors indicated that the luminescence mechanism and saturation effects may have to be taken into consideration.

(3) The oscillatory structure of S_e with Z_1, the atomic number of the projectile, at a constant velocity may cause considerable changes in the relative spacing of the theoretical curves.

(4) Radiation damage produced along the path under low energy ion bombardment[8] may alter the ratio of radiative to non-radiative transitions.

(5) It may be necessary to take into account the properties of the crystal and the state of the surface of the sample, as well.[15]

A comparison of the experimental results from the ZnS phosphors (Figs. 61 to 66) with the L values obtained from Eqn. (1) indicates a large discrepancy in functional relationships at lower energies. Thus a major influence on the light output under ion bombardment is non-radiative surface recombination.

Figs. 67 (a, b and c) display the results of ZnS:Ag, ZnS:Cu:Ag and ZnS:Cu phosphors when bombarded with $^1H^+$ and $^{40}Ar^+$ ions. The points are experimental and the solid curves were calculated from Eqns. (9) and (14), respectively, with the suitable choice of diffusion length L_D and the surface loss parameter Q (see Table III), the constant k' in Eqn. (9) was adjusted so as to normalize the curve to hydrogen at 10 KeV; the remaining points then followed. The normalized value of k' was then used in calculating the theoretical L values as a function of ion energy for the argon curve in Eqn. (14).

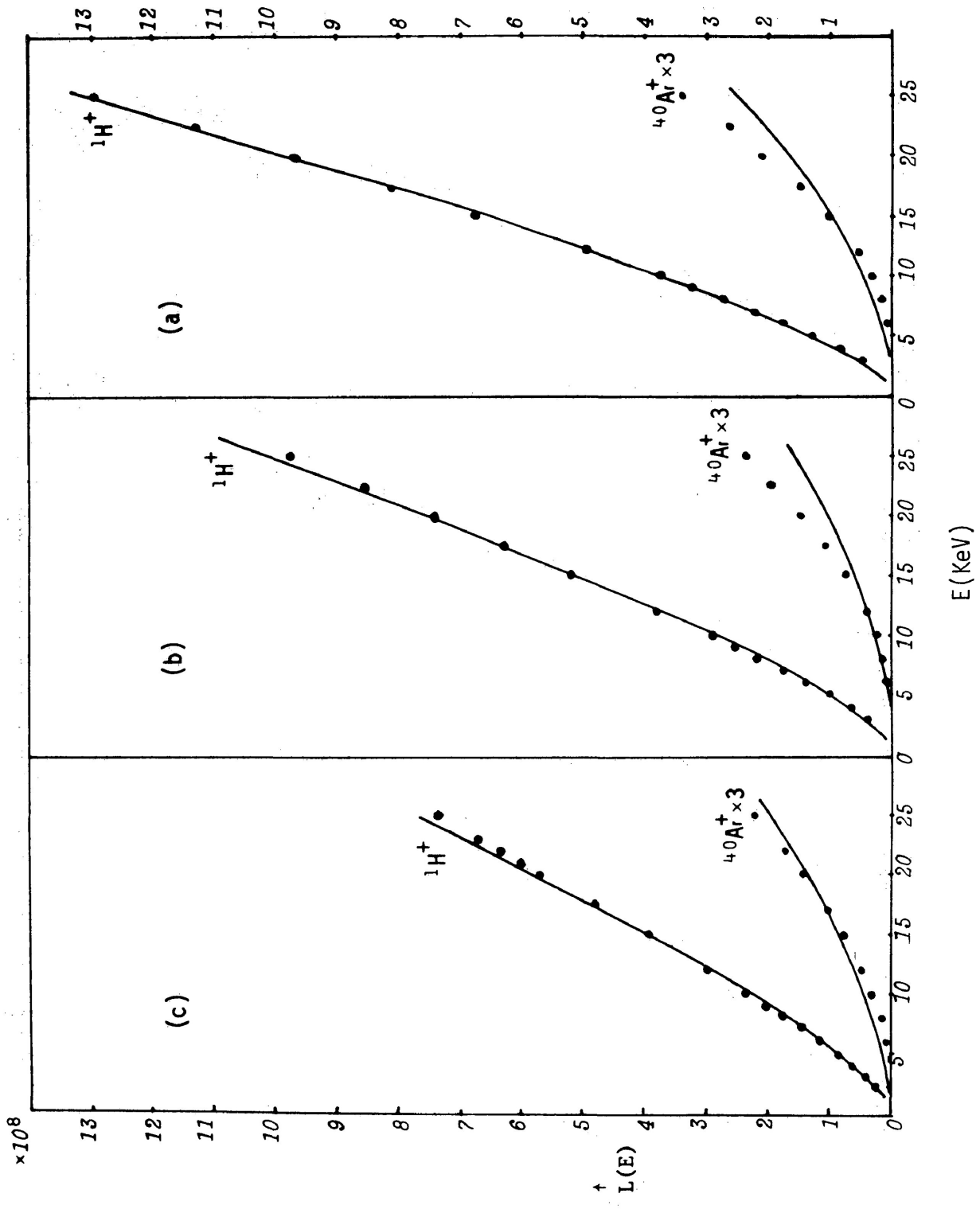

Fig. 67. A linear plot of L *versus* E for $^1H^+$ and $^{40}Ar^+$ ions impinging on (a) ZnS:Ag (b) ZnS:Ag;Cu and (c) ZnS:Cu at lower energies. The solid curves represent the appropriate theoretical function with suitable choice of L_D and Q.

TABLE III

SAMPLE	L_D (Å)	Q	CRYSTAL STRUCTURE
ZnS:Cu	1000	0.80	Cubic
ZnS:Cu:Ag	1000	0.95	Hexagonal
ZnS:Ag	1000	0.90	Cubic

From Fig. 67 it can be seen that the theory for $^{1}H^{+}$ agrees very well with experiment, and for $^{40}Ar^{+}$ the observed difference between the experimental light output and the theoretical one was within 20 percent. This discrepancy is expected considering the number of approximations involved in Eqn. (14). The result indicated that the range correction factor α_R for $^{40}Ar^{+}$ in ZnS which we approximated by $1 + 1/3\mu = 4/3$ where we put $\mu \simeq M_2/M_1 = 1$ is overestimated since α_R must be a function of energy.

The differences in surface loss parameter Q as given in Table III for these ZnS phosphors may be due to the presence of different activators in the crystal and the crystal structure itself.

Comparing the results with Gergely's values,[53] $L_D = 1130$ Å and $Q = 0.7$ for a ZnS:Ag,Cl sample, the agreement is remarkable. The latter were determined by cathodoluminescence.

VI.

CONCLUSIONS

Twenty-six types of phosphor-activator-surface treatment combinations have been subjected to bombardment by five species of ions with masses ranging from one to forty and with energies ranging from three to one-hundred KeV. For each ion-phosphor pair an ionoluminescent efficiency has been determined under the same experimental conditions so that it is now possible to make comparative statements about the efficiences of any of the phosphors subject to bombardment by any of the ions in this energy range.

Luminescence is a result of the direct excitation of the lattice electrons. The intensity of the light output, L, is a function of ion energy and is approximately proportional to the total amount of energy lost to electrons by the ion in the stopping medium. The transfer of ion energy to the lattice is more important than the transfer to the impurities themselves. Light production in the phosphor depends strongly on the types of radiative and non-radiative transitions which may occur in the bulk and on the surface of the phosphor. For scintillators such as NaI and ZnS, the major influence on the light output under heavy ion bombardment is surface recombination. For the majority of low efficiency phosphors, $CaWO_4$, YVO_4, etc., it appears that saturation of the luminescence mechanism may occur due to the high specific electronic energy loss $(dE/dR)_e$ of the low energy ions. That such might be the case is reasonable since the non-radiative recombination processes already completely dominate the radiative ones. If the lifetime of the

non-radiative process is shorter than that of the radiative one, then it follows that ionoluminescence will be quenched for high excitation densities. These phosphors should be characterized by low ambipolar diffusion coefficients which help to keep the density of excited electrons high enough for saturation phenomena to occur. In other phosphors, such as ZnS, with high efficiencies and relatively large ambipolar diffusion coefficients, the recombination of the electron-hole pairs at short-lived, non-radiative centers at the surface has the dominant influence on the detailed behaviour of ionoluminescence. This type of model has been shown to apply to ZnS and NaI, and may also apply in Plastifluor in combination with the bulk saturation effect. In any of the phosphors studied, either or both of these effects may influence the light output. For a phosphor in which neither is present, L *versus* E for $^1H^+$ should be linear since $S_e >> S_n$. If the curve is concave toward the energy axis, surface recombination must be the dominating recombination effect. If it is concave away from the axis, saturation is the most likely candidate.

In general, it is hard to determine the validity of the simple expression, Eqn. (1), for the number of electrons excited by a fast ion, since both saturation and surface recombination will lower the light output for heavy ions.

For those phosphors in which the transfer of excitation energy involves the motion of electrons, the major influence on the light output under ion bombardment is surface recombination, the variation of the ionoluminescent intensity with ion energy may be described approxiby

$$L(E) = Cf(R_p / L_D) \int_0^{E_0} \frac{S}{S_e + S_n} dE$$

in which C is a constant, $f(R_p/L_D)$ is a function that takes into account surface recombination effects, such as Eqn. (15).

REFERENCES

[1]C. F. Eve and H. E. Duckworth, Can. J. Phys. 36, 104 (1958).

[2]A. van Wijngaarden and H. E. Duckworth, Can. J. Phys. 40, 1749 (1962).

[3]A. van Wijngaarden, L. Hastings and E. S. Kotteles, Can. J. Phys. 44, 789 (1966).

[4]L. Hastings, P. R. Ryall and A. van Wijngaarden, Can. J. Phys. 45, 2333 (1967).

[5]L. Hastings and A. van Wijngaarden, Can. J. Phys. 45, 4039 (1967).

[6]A. van Wijngaarden, D. J. Bradley and N. M. A. Finney, Can. J. Phys. 43, 2180 (1965).

[7]Q. H. Lao, L. Hastings, N. Finney and A. van Wijngaarden, Radiation Effects 1, 89 (1969).

[8]N. Bohr, Kgl. Danske Videnskab. Selskab. Mat. Fys. Medd. 18, No. 8, 1 (1948).

[9]K. O. Nielsen, *Electromagnetically Enriched Isotopes and Mass Spectrometry* (Academic Press, Inc.: New York, 1956).

[10]F. Seitz and J. S. Koshler, *Solid State Physics, Vol. 2* (Academic Press, Inc.: New York, 1956), pp. 340-345.

[11]J. Lindhard and M. Scharff, Phys. Rev. 124, 128 (1961).

[12]J. Lindhard, M. Scharff and H. E. Schiott, Mat. Fys. Medd. Dan. Vid. Selsk. 33, No. 14 (1963).

[13]D. W. Palmer, M. W. Thomson and P. D. Townsend, *Atomic Collision Phenomena in Solids* (North-Holland: Amsterdam, London, 1970), pp. 523-529.

[14]O. Doll, Z. Physik 162, 215 (1961).

[15]V. V. Makarov and N. N. Petrov, Soviet Physics Solid State 10, No. 1, 154 (1968).

[16] Ref. 13, pp. 565-570.

[17] C. J. Taylor, W. K. Jentschke, M. E. Remley, F. S. Eby and P. G. Kruger, Phys. Rev. 84, 1034 (1951).

[18] K. Allison and H. Casson, Phys. Rev. 90, 380 (1953).

[19] R. B. Murray and A. Meyer, Phys. Rev. 122, 815 (1960).

[20] R. Gwin and R. B. Murray, Phys. Rev. 131, 501 (1963).

[21] R. Gwin and R. B. Murray, Phys. Rev. 131, 508 (1963).

[22] S. Bashkin, R. R. Carlson, R. A. Douglas and J. A. Jacobs, Phys. Rev. 109, 434 (1957).

[23] J. B. Birks, Phys. Rev. 87, 903 (1952).

[24] E. Newman, A. M. Smith and F. E. Steigert, Phys. Rev. 122, 1520 (1961).

[25] R. W. Hill, Rev. Sci. Instr. 33, 1477 (1962).

[26] A. C. Riviere and D. R. Sweetman, Rev. Sci. Instr. 34, 1286 (1963).

[27] G. J. Lockwood and G. L. Cano, IEEE Trans. on Nucl. Sci., 716 (1966).

[28] G. J. Lockwood and G. L. Cano, Phys. Rev. 157, 677 (1967).

[29] J. B. Birks, *The Theory and Practice of Scintillation Counting* (Pergamon Press: Oxford, 1964).

[30] C. J. Taylor, W. K. Jentschke, M. E. Remley, F. S. Eby and P. G. Kruger, Phys. Rev. 84, 1034 (1951).

[31] J. B. Birks and F. D. Brooks, Phys. Rev. 94, 1800 (1954).

[32] J. W. King and J. B. Birks, Phys. Rev. 86, 568 (1952).

[33] J. M. Fowler and C. E. Roos, Phys. Rev. 98, 996 (1955).

[34] T. J. Gooding and H. G. Pugh, Nucl. Instr. Methods 7, 189 (1960).

[35] J. R. Prescott and A. S. Rupaal, Can. J. Phys. 39, 221 (1961).

[36] J. B. Birks and F. A. Black, Proc. Phys. Soc. A64, 511 (1951).

[37] J. B. Birks, Phys. Rev. 86, 569 (1952).

[38] E. Brannen and G. L. Olde, Radn. Research 16, 1 (1962).

[39] J. Lindhard, Proc. Roy. Soc. A311, 11 (1969).

[40] J. Lindhard and A. Winther, Mat. Fys. Medd. Dan. Vid. Selsk. 34, No. 4 (1964).

[41] M. Walske, Phys. Rev. 88, 1283 (1952).

[42] E. Bonderup, Mat. Fys. Medd. Dan. Vid. Selsk. 35, No. 17 (1967).

[43] J. Cheshire, G. Dearnaley and J. M. Poate, Phys. Letters 27A, 304 (1968).

[44] J. H. Ormrod, J. R. MacDonald and H. E. Duckworth, Can. J. Phys. 43, 275 (1965).

[45] B. Fastrup, P. Hvelplund and C. H. Sauttor, Mat. Fys. Medd. Dan. Vid. Selsk. 35, No. 10 (1966).

[46] P. Hvelplund and B. Fastrup, Phys. Rev. 165, 408 (1958).

[47] C. P. Bhalla and J. N. Braford, Phys. Letters 27A, 378 (1968).

[48] W. van Roosbroeck, Phys. Rev. 91, 282 (1953).

[49] R. A. Smith, *Proceedings of the International School of Physics* (Academic Press, Inc.: New York, London, 1963), pp. 171-173.

[50] J. P. McKelvey, *Solid State and Semiconductor Physics* (Harper and Row: New York, 1966), pp. 320-330.

[51] W. Shockley and W. T. Read, Phys. Rev. 87, 835 (1952).

[52] H. B. DeVore, Phys. Rev. 102, 86 (1956).

[53] G. Gergely, J. Phys. Chem. Solids 17, 112 (1960).

[54] E. B. Fehr, A. I. Friedman, F. J. Studer and G. R. Fonda, J. Opt. Soc. Am. 42, 917 (1952).

[55] J. H. Ormrod and H. E. Duckworth, Can. J. Phys. 41, 1424 (1963).

[56] H. E. Schiott, Mat. Fys. Medd. Dan. Vid. Selsk. 35, No. 9 (1966).

[57] J. B. Birks and F. D. Brooks, Proc. Phys. Soc. B69, 721 (1956).

[58] M. Walske, Phys. Rev. 101, 940 (1956).

[59] A. van Wijngaarden and L. Hastings, Can. J. Phys. 45, 2239 (1967).

[60]O. B. Firsov, Sov. Phys. JETP 36(9), 1076 (1959).

[61]E. H. Goh. Private Communication.

APPENDIX I.

DIFFERENTIAL NUCLEAR CROSS SECTION

In analyzing the differential cross section, a simple scattering parameter, which could describe all processes, is defined as $t = E \cdot \sin(\theta/2)$ where θ is the deflection angle and E the energy in the center of mass system, which can be obtained from the interaction potential, V(r):

$$\theta = - \frac{1}{M_0 v^2} \frac{\partial}{\partial p} \int_{-\infty}^{\infty} V \left(\left[p^2 + z^2 \right]^{\frac{1}{2}} \right) dz$$

where p is the impact parameter and z is the axis direction. The energy transfer T is related to the maximum energy transfer T_m by $T = T_m \cdot \sin\theta^2/2$. In this way is obtained a so-called universal differential cross section

$$d\sigma = \pi a^2 \cdot (dt/2t^{\frac{3}{2}}) \cdot f(t^{\frac{1}{2}})$$

where a is the screening parameter defined in Section III. The scaling function $f(t^{\frac{1}{2}})$ is reproduced in Fig. A-1.

At high values of t, $f(t^{\frac{1}{2}})$ approaches Rutherford scattering where $f(t^{\frac{1}{2}}) = 1/2t^{\frac{1}{2}}$. At very low values of t, $f(t^{\frac{1}{2}})$ behaves asympototically as $1.43\ (t^{\frac{1}{2}})^{0.35}$.

Having obtained the scattering cross section $d\sigma$, S_n can be calculated by $S_n = \int T d\sigma$ or $S_n = (T_m / \varepsilon^2) \int t\sigma$. By using ρ and ε and Eqn. (2), Lindhard introduced a reduced stopping cross section, $S(\varepsilon) = d\varepsilon/d\rho = (dE/dR) \cdot (\varepsilon/E) \cdot (R/\rho)$. Considering only nuclear collisions

$$\begin{aligned} (d\varepsilon/d\rho)_n &= NS_n \cdot (\varepsilon/E) \cdot (R/\rho) \\ &= (1/\varepsilon) \cdot \int f(t^{\frac{1}{2}})/2t^{\frac{1}{2}} dt. \end{aligned}$$

Therefore the final expression for $(d\varepsilon/d\rho)_n$ is

$$(d\varepsilon/d\rho)_n = (1/\varepsilon)\int_0^{\varepsilon} f(X)\,dX$$

where we have let $X = t^{\frac{1}{2}}$.

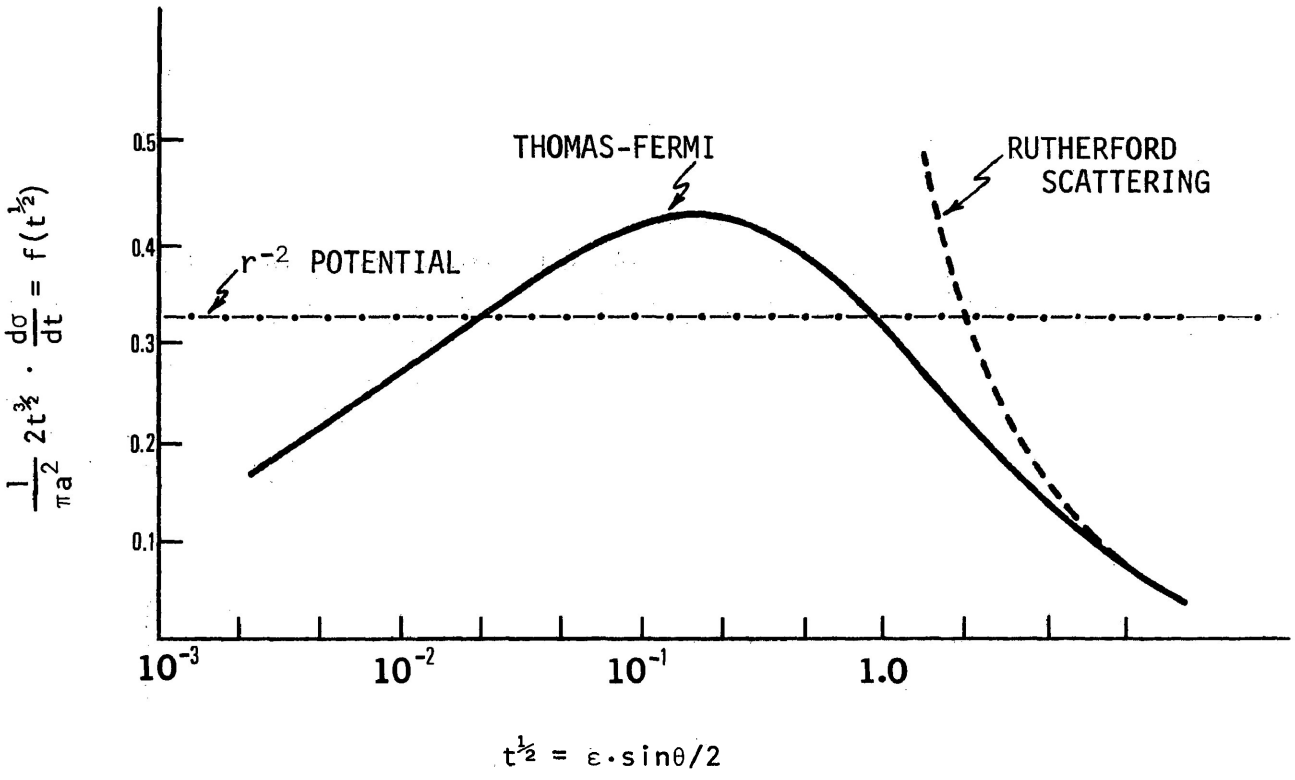

Fig. A-1. Plot of $f(t^{\frac{1}{2}})$ as a function of t for elastic nuclear collisions. Estimated from Thomas-Fermi type interaction.

APPENDIX II.

CONTINUITY EQUATION

Consider a small volume element of the crystal of unit cross section and thickness, dX, as shown in Fig. A-2.

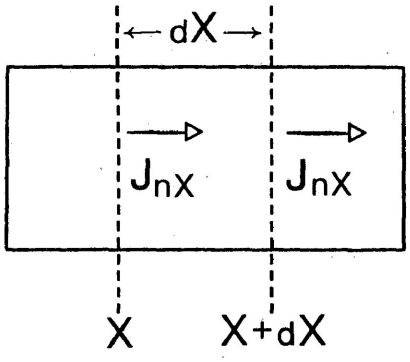

Fig. A — 2.

The particle flux densities, J_n and J_p, of electrons and holes, respectively, are flowing perpendicular to the unit cross section into the region at point X, and leaving the region at point X+dX. The flux density of electrons entering the volume element at the point X is denoted by $J_{nX}(X+dX)$. $J_{nX}(X+dX)$ can be obtained by making a Taylor expansion and taking the first two terms

$$J_{nX}(X+dX) = J_{nX}(X) + (dJ_{nX}/dX)\cdot dX.$$

Therefore the net increase in the number of electrons (or holes) within the volume element per unit time arising from a difference of J_{nX} entering and leaving the region is

$$\{J_{nX}(X) - J_{nX}(X+dX)\} = -(dJ_{nX}/dX)dX.$$

If the number of electrons generated per unit time within the volume element is $g_n dX$ and the number of electrons lost per unit time

by recombination is $(n/\tau_n)dX$, then the total net increase of the number of electrons in the volume element per unit time, which is $(dn/dt)dX$, is the algebraic sum of the contributions arising from the three different processes (drifting and diffusion, generation and recombination). Thus we may write

$$(dn/dt)dX = - (dJ_{nX}/dX) + g_n dX - (n/\tau_n)dX$$

or

$$dn/dt = - (dJ_{nX}/dX) + g_n - (n/\tau_n).$$

Similarly a calculation for holes within the same volume element will yield

$$dp/dt = - (dJ_{pX}/dX) + g_p - (p/\tau_p).$$

In general for the three-dimensional case we write

$$dn/dt = - \nabla\cdot\underset{\sim}{J}_n + g_n - n/\tau_n \qquad \text{(A-1)}$$

and

$$dp/dt = - \nabla\cdot\underset{\sim}{J}_p + g_p - p/\tau_p. \qquad \text{(A-2)}$$

The flux densities themselves may be written in the form

$$\underset{\sim}{J}_n = - D_n\nabla n - n\mu_n\underset{\sim}{E} \qquad \text{(A-3)}$$

$$\underset{\sim}{J}_p = - D_p\nabla p + p\mu_p\underset{\sim}{E} \qquad \text{(A-4)}$$

where D_n and μ_n are the diffusion coefficient and mobility of electrons and D_p and μ_p are the diffusion coefficient and mobility of holes. $\underset{\sim}{E}$ is any electric field which might be present.

The second term on the right-hand side of the last equation is the drift current density arising from an electric field (external or internal) which might be present. The first term on the right-hand side represents the diffusion flux density. That is, whenever there is a gradient of density, the particles will diffuse from a high concentration region to a low concentration region, and the particle flux density is therefore proportional to the gradient of concentration.

Substituting the current equations (A-3) and (A-4) into Eqns. (A-1) and (A-2) we obtain

$$dn/dt = D_n\nabla^2 n + \mu_n\nabla\cdot(n\underset{\sim}{E}) + g_n - n/\tau_n$$

and $$dp/dt = D_p\nabla^2 p + \mu_p\cdot(p\underset{\sim}{E}) + g_p - p/\tau_p.$$

Expanding $$\nabla\cdot(n\underset{\sim}{E}) = n\nabla\cdot\underset{\sim}{E} + \underset{\sim}{E}\cdot\nabla n$$

$$dn/dt - D_n\nabla^2 n + \mu_n\{n\nabla\cdot\underset{\sim}{E} + \underset{\sim}{E}\cdot\nabla n\} + g_n - n/\tau_n \qquad (A\text{-}5)$$

$$dp/dt = D_p\nabla^2 p - \mu_p\{p\nabla\cdot\underset{\sim}{E} + \underset{\sim}{E}\cdot\nabla p\} + g_p - p/\tau_p. \qquad (A\text{-}6)$$

We may use the 'quasi-neutral approximation' or 'charge balance' assumption[48-50] with the conditions

$$n-n_0 = \Delta n = \Delta p = p-p_0.$$

Consider a homogeneous sample where n_0 and p_0 are constants and the gradients and time derivatives of n and p are simply equal to the gradient and time derivatives of Δn and Δp, respectively:

$$dn/dt - d(\Delta n)/dt = d(\Delta p)/dt = dt/dt$$

and $$\nabla n = \nabla(\Delta n) = \nabla(\Delta p) = \nabla p.$$

Since we already know that $g_n = g_p$ and $n/\tau_n = p/\tau_p$ we may therefore write $g = g_n = g_p$ and $r = n/\tau_n = p/\tau_p$ and Eqns. (A-5) and (A-6) have the following form

$$d(\Delta n)/dt = D_n\nabla^2(\Delta n) + \mu_n\{n\nabla\cdot\underset{\sim}{E} + \underset{\sim}{E}\cdot\nabla(\Delta n)\} + g - r$$

and

$$d(\Delta p)/dt = D_p\nabla^2(\Delta n) - \mu_p\{p\nabla\cdot\underset{\sim}{E} + \underset{\sim}{E}\cdot\nabla(\Delta n)\} + g - r.$$

We now multiply the first of these equations by $\mu_p p$ and the second by $\mu_n n$, add them together to eliminate the term involving $\nabla\cdot\underset{\sim}{E}$

$$\frac{d(\Delta n)}{dt} = \frac{\mu_n D_p + p\mu_p D_n}{n\mu_n + p\mu_p}\nabla^2(\Delta n) + \frac{\mu_n\mu_p(p-n)}{n\mu_n + p\mu_p}\underset{\sim}{E}\cdot\nabla(\Delta n) + g - r\ .$$

Noting that $D_p\mu_n = D_n\mu_p$ (Einstein relation) we obtain

$$\frac{d(\Delta n)}{dt} = \frac{n+p}{n/D_p + p/D_n} \nabla^2(\Delta n) + \frac{p-n}{n/\mu_p + p/\mu_n} \underset{\sim}{E}\nabla(\Delta n) + g_0 - r \ .$$

By defining $$D^* = \frac{n+p}{n/D_p + p/D_n}$$

and $$\mu^* = \frac{p-n}{n/\mu_p + p/\mu_n}$$

where D^* and μ^* are called the ambipolar diffusion coefficient and mobility, we obtain the so-called ambipolar continuity equation

$$\frac{d(\Delta n)}{dt} = D^*\nabla^2(\Delta n) + \mu^*\underset{\sim}{E}\nabla(\Delta n) + g - r \ .$$

APPENDIX III.

TABLE II

Optical and physical properties of the phosphors and scintillation crystals obtained from the manufacturers' specifications.

	SAMPLE		PARTICLE SIZE	EMISSION WAVELENGTH	DECAY CONSTANT
1	ZnS:Ag	(P-22)	6.7 – 11.3μ	4500 Å	0.075 msec
2	ZnS:Ag	(P-11)	10.5μ	4500 Å	0.09 msec
3	ZnS:Ag	(P-11)	4.0μ	4500 Å	0.09 msec
4	ZnS:Ag:Cu	(P-2)	21.0μ	4500 and 5200 Å	0.09 msec
5	ZnCdS:Ag	(P-22)	6.3 – 11.5μ	5490 Å	0.052 msec
6	ZnS:Cu	(P-31)	11.5μ	5350 Å	80 msec
7	ZnCdS:Ag	(P-20)	4.0μ	5350 and 5700 Å	0.052 msec
8	CsI(Tℓ)			4200 and 5700 Å	1.1 msec
9	Zn_2SiO_4:Mn	(P-1)	10.5μ	5250 Å	10.0 msec
10	Zn_2SiO_4:Mn	(P-1)	5.0μ	5250 Å	
11	Zn_2SiO_4:Mn	(P-1)	10.0μ	5250 Å	
12	Zn_2SiO_4:Mn	(P-1)	10.5μ	5250 Å	10.0 msec
13	Zn_2SiO_4:Mn	(P-1)	2.0μ	5250 Å	
14	Zn_2SiO_4:Mn	(P-1)	5.2μ	5250 Å	
15	ZnO:Zn	(P-15)	4.0μ	4800 and 5200 Å	
16	$CaWO_4$	(P-5)	11.0μ	4200 Å	7.0 μsec
17	NaI(Tℓ)			4100 Å	0.25 μsec
18	$CaWO_4$	(P-5)	5.5μ	4200 Å	7.0 μsec
19	CsI(Na)			4100 Å	0.008 μsec
20	Stilbene				
21	Y_2O_2S:Eu	(P-22)	8.3μ	6270 and 6175 Å	
22	YVO_4:Eu:Bi	(P-22)	7.2 – 11 μ	7030, 6140, 6190 and 7000 Å	
23	$KMgF_3$:Mn		10.0μ	5950 Å	75 msec
24	YVO_4:Eu		7.2 – 11 μ		
25 and 26	Plastifluor			4250 Å	0.004 μsec